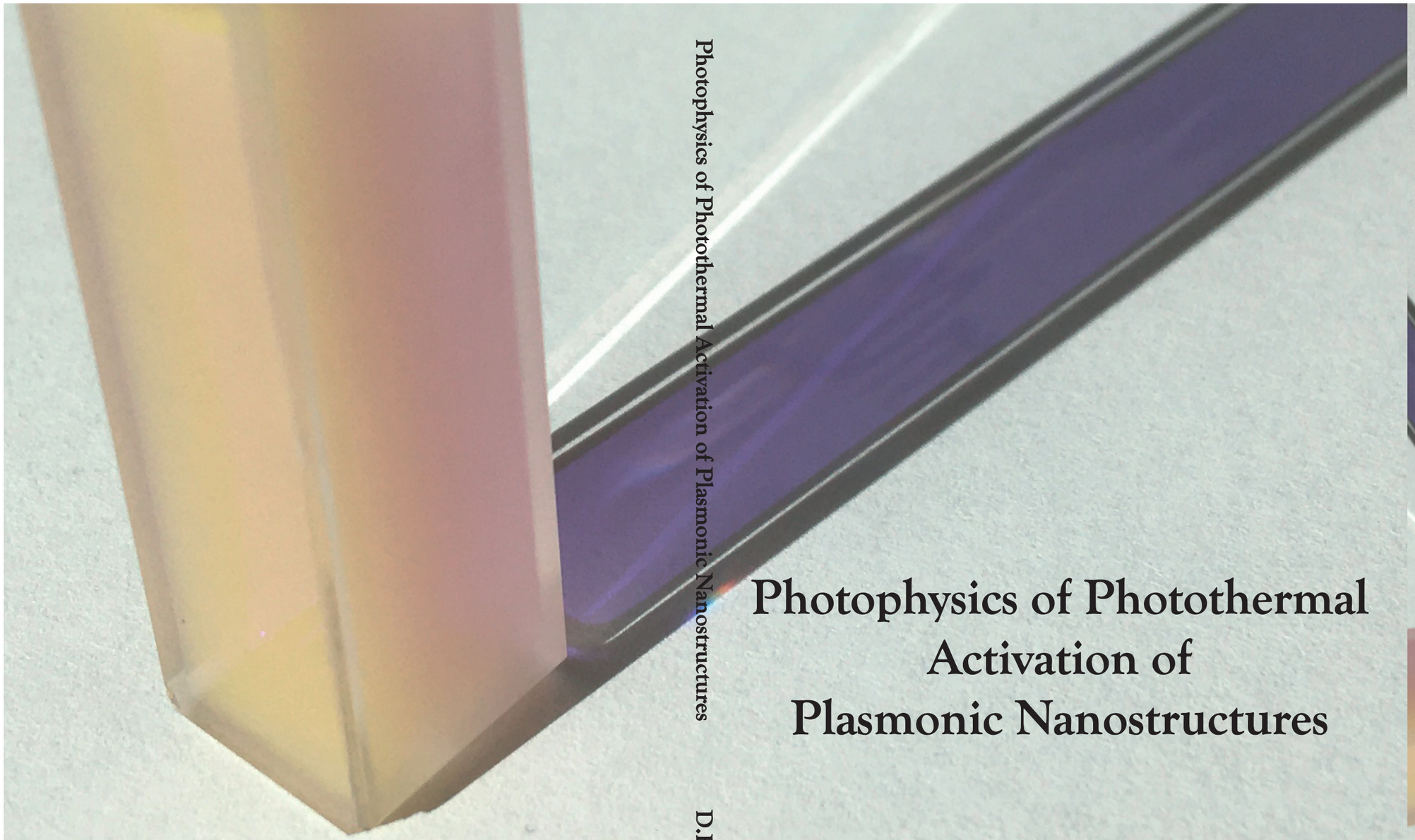

PCS PhotoCatalytic Synthesis

UNIVERSITY OF TWENTE.

ISBN
978-90-365-5179-3

Photophysics of Photothermal Activation of Plasmonic Nanostructures

D.B. O'Neill

You are cordially invited to attend the defence of my PhD dissertation:

Photophysics of Photothermal Activation of Plasmonic Nanostructures

By
Devin B. O'Neill

on
9th of July 2021
at
12:45 PM

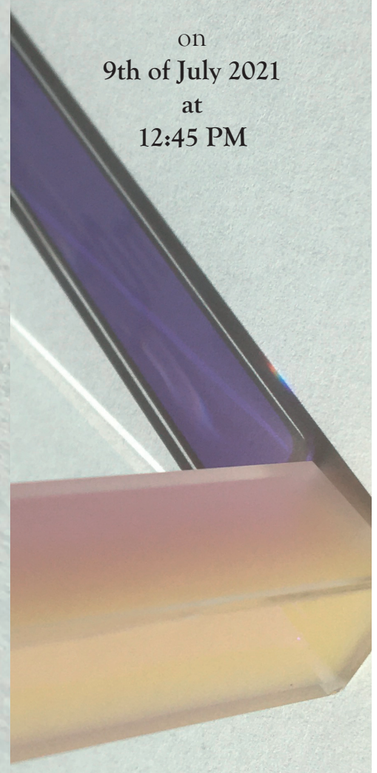

Photophysics of Photothermal Activation of Plasmonic Nanostructures

Devin B. O'Neill

Paranymphs
Ronald Jong
Piotr Krzywda

BK

561892-L-os-ONeill

Photophysics of Photothermal Activation of Plasmonic Nanostructures

Devin Brent O'Neill

PHOTOPHYSICS OF PHOTOTHERMAL ACTIVATION OF PLASMONIC NANOSTRUCTURES

DISSERTATION

to obtain

the degree of doctor at the University of Twente,

on the authority of the rector magnificus,

prof. dr. ir. A. Veldkamp,

on account of the decision of the Doctorate Board

to be publicly defended

on Friday 9 July 2021 at 12.45 hours

by

Devin Brent O'Neill

born on the 19th of June, 1987

in Ottawa, Canada

This dissertation has been approved by:

Supervisor

prof. dr. ir. G. Mul

Co-supervisor

dr. J.M. Huijser

Cover design: Photo of silver nanocubes coated in ceria suspended in ethanol in a sunebeam by Devin O'Neill

Printed by: Ipskamp, Enschene

Lay-out: by Devin O'Neill, Using Adobe products.

ISBN: 978-90-365-5179-3

DOI: 10.3990/1.9789036551793

Graduation Committee:

Chair / secretary:	prof.dr. J.L. Herek
Supervisor:	prof.dr.ir. G. Mul
Co-supervisor:	dr. J.M. Huijser
Committee Members:	prof. dr. M. Orrit prof. dr. B.M. Weckhuysen dr. E. Groeneveld prof.dr.ir. L. Lefferts prof.dr.ir. H.L. Offerhaus

Table of Contents

Introduction

This chapter will give a brief overview of the subjects which will be covered in this thesis. There are six sections to this chapter, which guide the reader from the general to the specific aspects of the thesis. First there is a short justification of the motivation into the field of research. Second there is a brief discussion of photocatalysis which guides the focus towards semiconductors. Third, there is a description of the process of light absorption. Fourth is a description of plasmonic materials and the role they can play as sensitizers for photochemical processes. Fifth is a description of the spectroscopic techniques used to characterize the charge and energy transfer. Finally, this chapter concludes with a description of the work which follows in the thesis.

1 Why focus on light driven processes

In the modern day there is a drive towards sustainability and renewability because of the undeniable impact humanity has had on the planet: not only that we are in the Anthropocene, but the limitations of the global carrying capacity and ever increasing energy demands (and the byproducts thereof).[1–4] It is then worth noting what sustainable energy there is on the planet: energy showered upon the planet (solar), or capturing energy from naturally occurring processes (wind, rain, tidal, geothermal, etc.).[5] Solar light can be used directly for catalysis, which allows for potentially less waste of energy (since some energy is lost with every conversion), which makes photocatalysis interesting.

There is another reason to use photocatalysis (reactions occurring on the surface of a light-activated catalyst) or photochemistry (direct light activation of a chemical bond): energy reduction in establishing chemical processes. When a molecule is photo-dissociated in a photochemical reaction, then the light energy is used to break the chemical bond. Since the energy of a bond can be quite high, breaking it can be quite energetically costly. Further, use of specific energies of light can stimulate specific product formation: it is possible to photo-dissociate Br_2 into two ground state radicals, one ground state and one excited sate radical, or two excited state radicals based on which electronic transition is excited.[6]

But photocatalysis or photochemistry are not the only possibly means to use solar light: generation of electricity is also possible. Solar cells convert light into electricity, and given the ever increasing electrification of modern life,[7–9] this can be of great benefit. As such, looking at means of improving energy generation from light is of great interest.

In photocatalysis, photochemistry, or solar cell technology, before a new process or product can be developed, there needs to be a more fundamental study of the materials. Asking what the fate of the energy of the absorbed light is: does it generate charge carriers in a material, does it directly drive a reaction, or does it generate heat? Further, often a system is sensitized, where one material absorbs the light, and then transfers the energy of the charge to another. In this case, the fate of the light can be even more varied: does the photosensitizer transfer energy or charge, is heat generated? How can these be controlled, how manipulating the materials to sensitize a system in the way we envision, is paramount to being able to make the high quality processes or products which harvest light for use?

2 What is photocatalysis?

Before we delve into the body of work presented in this thesis, it is good to ensure that we are all on a level enough field; so, we briefly begin with the simplest of topics: what is catalysis, and from that what is photocatalysis. From there it is a clear path to subjects of what influences and effects photocatalysis. Finally, a short description of how photocatalysts can be characterized concludes this chapter before the thesis moves into the experimental work. It is hopeful that this chapter will aid those not as well versed in the field in their understanding of this work; and so, we begin at the very beginning – a very good place to start.

Catalysis is a means of achieving more, with less. When a chemical reaction occurs, there are energetic barriers, and product selectivity; a catalyst can reduce the former and control the latter. By using a catalyst, the reaction pathway changes rather than proceeding from X to Z directly, it passes through several step(s). This is shown in Figure 1; where the activation energy (E_a) is different with and without a catalyst, but since both pathways have the same products and reagents, the total change in Gibbs free energy (ΔG) is the same. The catalyst can also be used to change the product selectivity, in Figure 1 it may be possible to only proceed to point A, and thereby get a different product. It is through changing the reaction pathway that a catalyst provides a reduction in activation energy, product selectivity, or both – and that is why they are of great interest, and value.

With catalysis superficially understood, now there is another question - what is a catalyst? There are three main types of catalysts, and increasing in size they are: homogeneous, biological, and heterogeneous. Homogeneous catalysts are molecules, often consisting of a metal atom and coordinating ligands, which exist in the same phase as the chemicals they react with. Biological catalysts are enzymes and proteins, orders of magnitude larger than homogeneous catalysts, which are suspended in the same phase as the chemicals. Heterogeneous catalysts are surfaces, they are in a different phase as the chemicals they react with – solid catalysts with

gaseous or liquid chemical reagents to react. Since the body of this work is on heterogeneous catalysts, so too will the focus of this introduction be.

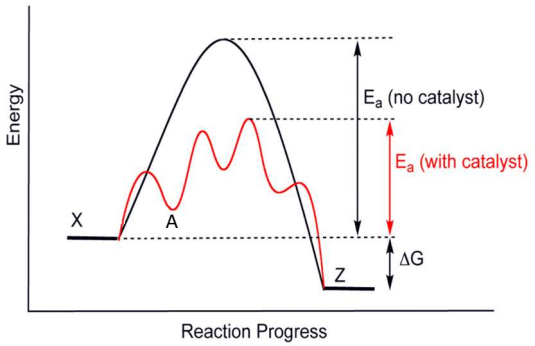

Figure 1: A reaction can progress with a relatively high activation energy, or with a catalyst, through a different series of reactions, needing less activation energy. Regardless of the path taken, for the same start and end products the total change in energy is the same. Public domain image.

Heterogeneous catalysts are materials with an active surface. This activity can stem from the chemical or physical structure of the material. The first has two components which can be separated: materials made up of one type of atom (metals), or materials made up of several (oxides, nitrides). The second relates more to metals than to oxides and nitrides but is still quite relevant.

Properties stemming from chemical ones in metals is well exemplified with the dissociative adsorption of hydrogen on platinum[10]: when the hydrogen gas adsorbs onto the platinum the bond between hydrogen atoms breaks, forming two hydrogen atoms, separately bound to the surface. In oxides and nitrides the interaction comes from the difference in the atoms making up the structure and is well exemplified with gallium nitride's interaction with methane: the hydrogen can become bound by the nitrogen, while the carbon by the gallium which leads to the cleavage of the C-H bond[11]. These interactions stems from the properties of the materials, specifically how strongly the chemical binds to the surface (this ultimately leads to the Sabatier principle).[12]

Physical structure plays a key role as well; although quite differently in metals, and in oxides and nitrides. In metals having steps or defects can create sites of relative excess or depletion of electrons – as they behave as a delocalized gas which is continuous throughout the material. This results in regions of slightly positive (δ+) or negative (δ -) charges on the surface and is called Smoluchowski smoothing

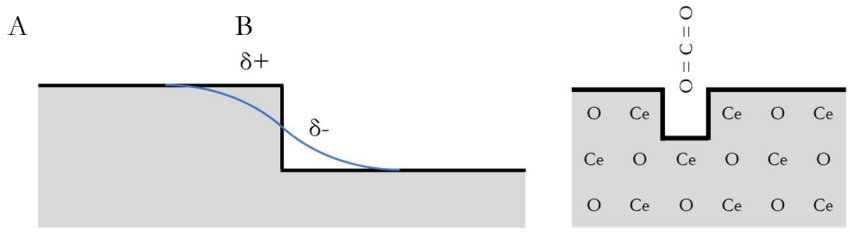

Figure 2: Surface structures which influence catalysis: A) Smoluchowski smoothing of electron density along a defect in a surface, resulting in localized charge differences. B) An oxygen vacancy in CeO_x which can participate in Mars-van Krevelen type mechanism of the reduction of CO_2 by incorporating one of the oxygens from CO_2 into the CeO_x lattice. The oxygen vacancy is restored by reaction with H_2 to form water.

(Figure 2A).[13,14] Another surface structure related property is the Mars-van Krevelen mechanism: which is the Theseus's ship approach to catalysis. First a lattice atom reacts with an adsorbs species, for example H_2, and the product (water) leaves the surface, producing a vacancy. In a second reaction a different molecule can bind and react, which regenerates the surface – but with a new atom (Figure 2B, the example for reaction of CO_2, producing CO, is shown).[15] This is commonly seen in reactions over ceria, on the account of ceria, which easily reduces from Ce(IV) to Ce(III) and can subsequently be re-oxidized.[16–18]

While morphology and composition will influence and dictate much of the catalytic properties, all reactions require energy to occur. Driving a catalytic reaction is the same as any other chemical reaction: heat, light, or electric potential can all stimulate reactions. Regardless of the stimulation source, one or more electrons are moved, either from or to the catalyst: filling or depleting molecular orbitals which cause bonds to break or form.

In photocatalysis light energy is used to overcome kinetic barriers of exothermic reactions, for example in the oxidation of water contaminants. In the case of endothermic reactions, light energy not only initiates the reaction (kinetically), but also is converted into chemical potential energy (thermodynamically): photons become chemical bonds, such as in the conversion of water to hydrogen and oxygen. For such a transformation to occur, the light must be absorbed, typically by a semiconductor (the photocatalyst); but not all light is equal, with different wavelengths having different energies, which result in different interactions. The nature of light-matter interactions will be briefly discussed, as well as the effect different energies can have. Following that, a short summary of how this relates to semiconductor photoexcitation will be presented. Concluding the

discussion of light absorption is one on the use of plasmonic materials to enhance light absorption in semiconductors. This introduction concludes with a final section about the methods for spectrally characterizing the materials.

3 Light absorption

Light is made up of photons, with each having an energy specific to its wavelength, and upon absorption a photon's energy can be transferred to the light absorber through an electronic transition. In atoms an electron can be excited from a low energy atomic orbital to a higher energy atomic orbital, likewise in a molecule between molecular orbitals and in a semiconductor from the valence band to the conduction band.

Atoms have the simplest interactions with light: electronic absorption, and scattering resulting from its polarizability (how easily the electron density of the atom in space is perturbed by an electric field). The former is the promotion of an electron to a higher energy orbital, leaving the lower energy orbital electron deficient. Upon internal relaxation, the light could be reemitted; the basis of photon emission spectroscopies. The second option involves scattering, which does not involve a stable electronic transition, but instead an unstable, transient, excitation. For atoms this is simply Rayleigh scattering, where a photon excites an electron to a "virtual state" (a transient perturbation of the electron density in space) which promptly relaxes through reemitting the light.[19,20]

Molecules add a level of complexity: molecular orbitals and motion. When atoms form chemical bonds, molecular orbitals are formed; an incident photon can excite an electron from a low energy molecular orbital to a higher energy molecular orbital. Depending on the nature of the electronic transition, light absorption can strengthen or weaken a chemical bond by promoting an electron from or to an antibonding orbital, the latter causing the molecule to become less stable and potentially initiating a photochemical reaction. Internal relaxation after electronic excitation may lead to emission of a photon through fluorescence, or after intersystem crossing through phosphorescence.[21]

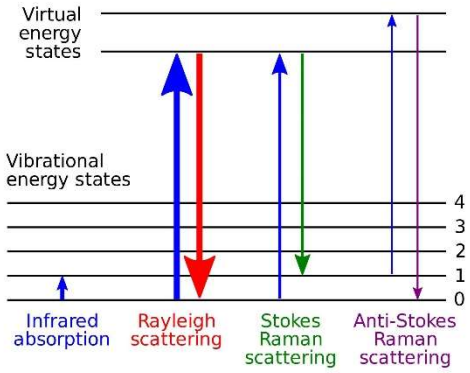

Figure 3. Depiction of different transitions possible, including infrared excitation of vibrational modes, Rayleigh scatter, and Raman scattering. Image reproduced under CC 3.0.

Motion of the atoms with respect to one another, molecular vibrations, add a new set of vibrational energy levels to the molecule. Each electronic energy level is accompanied by a series of vibrational levels; these allow for absorption of light in the infrared range of wavelengths. Additionally, it is possible that a phenomenon related to Rayleigh scattering can occur: Raman scattering. This occurs when the initial and final vibrational level are not the same, and the scattered photon has more or less energy (Anti-Stokes scattering and Stokes scattering in Fig. 3), with the difference coming from the change in vibrational energy of the molecule.[21]

Semiconductors are essentially incredibly large molecules; where the populated orbitals form a valence band, and the unpopulated orbitals form a conduction band. These electronic energy levels form bands, as the number of orbitals which interact with near-degenerate energy combine forming a near-continuum. Absorption of light causes an electron to be promoted from the valence band to the conduction band, leaving behind an electron vacancy in the valence band (a so-called 'hole'). Given no other means of relaxation, eventually the electron will relax back into the valence band, potentially via trap states within the bandgap. Vibrations could change as well, as rather than a molecule undergoing a relatively simple vibration, a perturbation of the crystal may propagate through the entire material or crystal. That is, disturbing one atom will cause those near it to be disturbed, and this will spread akin to a ripple in water – temporarily stretching or compressing bonds of the semiconductor. Once a photon is absorbed, a photochemical reaction can result. An adsorbed molecule can either accept an electron from the conduction band into an antibonding orbital (potentially leading to a photochemical reaction) or can donate an electron from an orbital into a hole in the semiconductor valence band. In this manner, semiconductor-assisted photocatalysis can occur. Also photoinduced redox

processes in the semiconductor, e.g. the promotion of oxygen vacancies (see Fig. 2), could play an important role in photocatalysis.

4 Local Surface Plasmon Resonances as a photosensitizer

Some materials can support a local surface plasmon resonance (LSPR); that is, a collective oscillation of electrons stimulated by specific frequencies of light.[21] LSPR can occur for frequencies where the magnitude of the real component (ε_r) of the dielectric function of the material is greater (but opposing sign) than that of the environment (ε_{env}).[22] LSPR results in intense near-field enhancement of the intensity of the electromagnetic field. The extinction of plasmonic particles can be calculated through Mie theory, and (for spheres) resonance occurs when then the imaginary component of the dielectric function (ε_i) is equal to $\varepsilon_r + \chi\varepsilon_{env}$, where χ accounts for the aspect ratio. Specifically:[22,23]

$$D(\lambda) = \frac{24\pi^2 N a^3 \varepsilon(\lambda)_{env}^{3/2}}{\lambda ln\,(10)}\left[\frac{\varepsilon_i(\lambda)}{(\varepsilon_r(\lambda) + \chi\varepsilon_{env}(\lambda))^2 + (\varepsilon_i(\lambda))^2}\right] \qquad [1][21]$$

Where the extinction of a system of particles (D) is determined by the dielectric function for the material and environment, the number of particles (N) and radius (a).

There are many parameters which effect LSPR: the local dielectric environment,[24,25] particle size and shape,[26,27] changes in symmetry,[28–31] changes in charge,[32,33] and processes of relaxation[34–37] to name a few. The first, the local dielectric stems from the above description of the LSPR, and the dependence of D(λ) on the local dielectric function. There have been applications brought forward employing plasmonic films for detecting changes to the refractive index of the environment which take advantage of this property.[38,39] The effect of size and shape is quite pronounced, and can change the LSPR from 350 nm to being well into the NIR for silver nanoparticles.[40,41] Changes to the particle symmetry are a special case of the changes in local dielectric function. That is, inhomogeneous dielectric environments can break LSPR symmetry and create explicit 'up' and 'down' modes (that is, modes which extend predominantly into, or out of a substrate).[29,31,42] This has been employed for many applications, including intense excitation of, and subsequent spectroscopy of analytes in the nanogaps.[43,44] The penultimate effector on the LSPR is charge: when the charge of a particle changes, so will the bulk plasma frequency – and subsequently the LSPR shifts (blueshift with increased electron density, and redshift with a decreased electron density).[45] Finally, the specific

processes of LSPR relaxation will cause a number of effects, both spectrally and temporally; which merit a more complete discussion.

The fate of the LSPR can be divided into radiative and non-radiative processes. The radiative relaxation of an LSPR is the reemission of light.[35] Non-radiative relaxation of an LSPR can occur through either internal relaxation (generation of heat) or charge/energy transfer.[34,36,46,47] In the case of heat generation, the LSPR could dephase through Landau damping, which creates a non-equilibrium energy distribution of charge carriers. Landau damping is the physical mechanism which contributes to the imaginary component of the dielectric constant, and is the transfer of the LSPR energy to an electron resulting in a hot electron-hole pair.[36] Through electron-electron (e-e) scattering, the carrier energy distribution equilibrates into a system of thermalized electrons which are not in equilibrium with the lattice, and so electron-phonon (e-ph) coupling occurs and the lattice heats. Finally, this photogenerated heat will dissipate to the environment.[36,47] To avoid this thermo-plasmonic heat generation, a competitive process must occur to interrupt this process. There are some phenomena which occur before Landau damping of the LSPR (plasmon-induced resonant energy transfer, PIRET, and chemical interface damping, CID, sometimes called plasmon-induced charge transfer transition),[34,37,48] and some after (hot or thermalized carrier transfer)[49,50]. The effect that these have on the LSPR spectra can vary. With PIRET and CID the width and intensity of the LSPR may change due to lifetime broadening.[34,37,51,52] It should be noted that charge transfer is considered to not be exclusively possible during or after LSPR decay; also a direct interfacial charge transfer transition has been reported.[37])CID results in a new spectral mode,[37] and charge transfer to an adsorbate or semiconductor will change the electron density in the plasmonic nanostructure, which results in a shift in the LSPR[45].

Since the LSPR creates regions of highly enhanced electromagnetic intensity, they can be employed for enhancing the rate of photochemical reactions and certain kinds of spectroscopy.[34,53–56] The photochemistry is owing to the charge or energy transfer which can either directly drive chemical reactions,[53] or photosensitize other materials.[34] Enhancement of fluorescence, IR and Raman spectroscopy have been widely employed.[54–57] In all cases, the near-field amplification of the electromagnetic intensity results in multiple-order of magnitude increases in signal.[58]

As the LSPR leads to heat generation, there is also plasmonic enhancement of thermal processes; and indeed, some propose that much of the observed enhancement is due to thermal stimulus.[59] There are many issues with this claim, as it argues that the absence of a massive increase in photocatalytic reaction rate constant due to high energy ballistic carriers is evidence against any non-thermal

contribution, while disregarding observations of changes in product selectivity.[60] While there is considerable thermal contribution, and this has led to ambiguity in the root of plasmonic enhancement, there are several experimental methods to identify the different contributions.[61]

5 Characterization of potential plasmonic-semiconductor photocatalysts

In addition to experimentally disambiguating the role of heat or other plasmonic enhancement through the observation of reaction rates,[61] it is also possible to do so more directly through spectroscopic means.[55,62] Charge transfer can be observed through Raman spectroscopy, and so plasmon-induced charge transfer can be observed through surface-enhanced Raman spectroscopy (SERS).[55] Additionally, transient absorption allows for time-resolved spectroscopic observations of light-induced perturbations of systems in time.

The enhancement of Raman scattering in SERS can be described as stemming from the plasmon resonance (if the incident light is near the plasmon resonance), molecular resonance (if the incident light is near a stable electronic transition), and charge transfer.[55] The selection rules for SERS allows for further determination of effects, and when operating outside of molecular resonance (that is, SERS, and not surface-enhanced resonant Raman scattering), then the relative enhancement of the totally symmetric and non-totally symmetric modes allows for a determination of a quantitative measure: the degree of charge transfer (ρ_{CT}).[55]

$$\rho_{CT} = \frac{I^k(CT) - I^k(LSPR)}{I^k(CT) - I^0(LSPR)} \quad [2]$$

Where the superscript k denotes a chosen Raman line, and the superscript 0 denotes a chosen totally symmetric Raman line of the same molecule. The intensities (I) of the lines are compared when under CT conditions versus when under LSPR conditions. Since the totally symmetric modes are unaffected by CT, and the non-totally symmetric modes are unaffected by the LSPR this allows for simplifications.[55] Experimentally by allowing for a single spectra to give ρ_{CT}, and mathematically:

$$\rho_{CT}(k) = \frac{\frac{I^k(CT)}{I^0(LSPR)}}{1 + \frac{I^k(CT)}{I^0(LSPR)}} \quad [3]$$

The limitation of this method is the need for a Raman probe through which CT would occur. A molecule must be the conduit for the CT to observe it through

this method. In contrast, through the direct, time-resolved observation of the electronic absorption spectra, detection of perturbations of the system, and the dynamics of resonance energy and charge transfer processes is possible.

Transient absorption (TA) spectroscopy is a technique in which a short light pulse is split (Fig. 4A), with part being tuned to a desired wavelength, and the other being delayed in time before (optionally) being converted to a broad spectrum; both then impinge on the same spot on a sample allowing the direct observation of the electronic absorption spectrum in time after the photoexcitation pulse.

It is through TA that the photodynamics of materials can be observed: tracking the light-induced LSPR excitation and processes following, such as the LSPR decay processes discussed above and potential resonance energy transfer or charge transfer to a semiconductor.[35,62,64–66] With this technique it is possible to observe the photo-excitation of ceria,[64] additionally the observation of plasmonic stimulation resulting in the same signal has been observed, indicative of LSPR-induced charge transfer.[62] Resonant energy transfer has also been observed through TA; by controlling the competition of charge and energy transfer.[35] The response of plasmonic nanoparticles has been well studied, from transient processes in ensemble measurements, to the formation of breathing modes due to heating in single nanocubes.[67,68]

Disambiguation of charge and resonance energy transfer by TA is possible, as both processes have a distinct spectral fingerprint. Further, the mechanism of charge

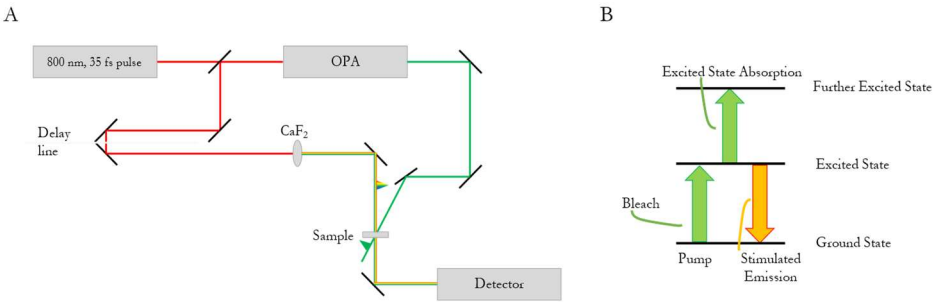

Figure 4: A) Scheme of the TA setup, the wavelength of the pump is controlled by the optical parametric amplifier (OPA) and a probe pulse is delayed and then used to generate white light to determine the spectra of the sample in time relative to the pump. B) A cartoon of the energy levels of a molecule, the pump excites electrons from the ground state to an excited state, the probe then observes the ground state bleach, and the new excited state absorption. The excited state can relax back to the ground state through stimulated emission during the probe or through a chemical reaction.

or energy transfer can be achieved through the examination of the wavelength dependent quantum yield:[37] hot electron processes have a wavelength dependance, while CID is excitation wavelength invariant.[37,69] Since TA shows both photoexcited absorption and photoinduced bleach, it can be possible to determine from where an electron is promoted to and from[62]. Using this knowledge, it is possible to d_etermine not only the light-induced mechanism(s), but also the efficiency of charge or energy transfer.

6 Scope of this Thesis

Chapter 2 examines the possibility of using silver bromide as a photocatalyst in the coupling of methane. In the intended process, the AgBr would act as a bromine source, and undergo photodissociation to form bromine radicals, which would react with methane to produce methyl bromide. This methyl bromide would be coupled over a solid acid to form higher order hydrocarbons and would be extracted from the stream. The byproduct of both methyl bromide formation and coupling is hydrogen bromide, which would be used to regenerate the silver bromide from the photogenerated silver releasing hydrogen. Unfortunately, this process was found to not be feasible at ambient pressures, and although hydrogen could be formed from hydrogen bromide over silver, the constraints applied on the process due to the highly caustic nature and the need for illuminated surface led to the conclusion of the project without successfully forming the process.

Chapter 3 is a study of the charge transfer between silver and ceria through a 4-mercaptobenzoic acid linker using Raman spectroscopy. It showed that for wavelengths with energy greater than half the HOMO/LUMO gap of the linker charge transfer would occur (As the HOMO/LUMO of the linker are of equal energy from the silver E_f), in accordance with Fowler's equation. Further, the greater the thickness of the shell the greater the degree of charge transfer. Finally, the silver nanocube core size had little to no effect on the degree of charge transfer, although it does affect the attenuation of light.

Chapter 4 is an observation of charge and energy transfer in a gold/cerium-praseodymium oxide system through TA. The concentration of praseodymium is varied to influence the spectral properties, while having a minimal effect on the electronic properties. In this way, the mechanism of excitation transfer is controlled: from ballistic electron injection, to chemical interface dampening and resonant energy transfer, depending on praseodymium concentration. This work sheds light

on the effects of spectral overlap, while usually associated with resonant energy transfer, here a clear connection to chemical interface dampening is shown.

Chapter 5 characterizes the ultrafast photodynamics of hafnium nitride nanoparticles, a non-noble metal plasmonic material. Previously literature has had conflicts between experimental and theoretical work, with the former claiming to observe excited carriers, while the latter predicted rapid generation of heat. This work unifies experimental and theoretical observations, by measuring and modelling HfN photodynamics, and conclusively shows that the effect of illumination is the ultrafast generation of heat. No evidence of excited carriers was observed. Further, a coherent Raman signal was observed, indicating the permanent degradation of the sample into $HfN_XO_YH_Z$.

Chapter 6 contains a perspective on the future direction of the work laid out in this thesis, and pitfalls to be avoided.

7 References

1. Bardi, U. Peak oil: The four stages of a new idea. *Energy* **34**, 323–326 (2009).
2. Barrett, G. W. & Odum, E. P. The twenty-first century: The world at carrying capacity. *Bioscience* **50**, 363–368 (2000).
3. Elhacham, E., Ben-Uri, L., Grozovski, J., Bar-On, Y. M. & Milo, R. Global human-made mass exceeds all living biomass. *Nature* **588**, 442–444 (2020).
4. Waters, C. N. *et al.* The Anthropocene is functionally and stratigraphically distinct from the Holocene. *Science* . **351**, 137 (2016).
5. Herzog, A. V, Lipman, T. E. & Kammen, D. M. Renewable energy sources: A variable choice. *Environ. Sci. Policy Sustain. Dev.* 8–20 (2001).
6. Asano, Y. & Yabushita, S. Theoretical study of nonadiabatic transitions in the photodissociation of Cl 2 and Br 2. *Chem. Phys. Lett.* **372**, 348–354 (2003).
7. Alhajeri, N. S., McDonald-Buller, E. C. & Allen, D. T. Comparisons of air quality impacts of fleet electrification and increased use of biofuels. *Environ. Res. Lett.* **6**, 024011 (2011).
8. Olówósejéjé, S., Leahy, P. & Morrison, A. P. A practical approach for increased electrification, lower emissions and lower energy costs in Africa. *Sustain. Futur.* **2**, 100022 (2020).
9. Mai, T. T. *et al. Electrification Futures Study: Scenarios of Electric Technology Adoption and Power Consumption for the United States. National Renewable Energy Laboratory* https://www.nrel.gov/docs/fy18osti/71500.pdf (2018).
10. Poelsema, B., Lenz, K. & Comsa, G. The dissociative adsorption of hydrogen on defect- ' free ' Pt (111). *J. Phys. Condens. Matter* **22**, 304006 (2010).
11. Li, L., Fan, S., Mu, X., Mi, Z. & Li, C. J. Photoinduced conversion of methane into benzene over GaN nanowires. *J. Am. Chem. Soc.* **136**, 7793–7796 (2014).

12. Rothenburg, G. *Catalysis: Concepts and Green Applications*. (Wiley-VCH, 2008). doi:10.1002/9783527621866.

13. Smoluchowski, R. Anisotropy of the Electronic Work Function of Metals. *Phys. Rev. B* **60**, 661–674 (1941).

14. Kolasinski, K. W. *Surface Science: Fundamentals of Catalysis and Nanoscience*. (Wiley, 2012).

15. Doornkamp, C. & Ponec, V. The universal character of the Mars and Van Krevelen mechanism. *J. mol. Cat A,* **162**, 19–32 (2000).

16. Fiorenza, R., Crisafulli, C. & Scirè, S. H2purification through preferential oxidation of CO over ceria supported bimetallic Au-based catalysts. *Int. J. Hydrogen Energy* **41**, 19390–19398 (2016).

17. Liu, B., Li, W., Song, W. & Liu, J. Carbonate-mediated Mars–van Krevelen mechanism for CO oxidation on cobalt-doped ceria catalysts: facet-dependence and coordination-dependence. *Phys. Chem. Chem. Phys.* **20**, 16045–16059 (2018).

18. Wang, C. *et al.* Water-Mediated Mars − Van Krevelen Mechanism for CO Oxidation on Ceria-Supported Single-Atom Pt 1 Catalyst. *ACS Catal.* **7**, 887–891 (2017).

19. Das, R. S. & Agrawal, Y. K. Raman spectroscopy: Recent advancements, techniques and applications. *Vib. Spectrosc.* **57**, 163–176 (2011).

20. Jones, R. R., Hooper, D. C., Zhang, L., Wolverson, D. & Valev, V. K. Raman Techniques: Fundamentals and Frontiers. *Nanoscale Res. Lett.* **14**, (2019).

21. Atkin, P. & Paula, J. *Physical chemistry. W.H. Freeman* Co., New York (2006)

22. Willets, K. A.; Van Duyne, R. P. Localized Surface Plasmon Resonance Spectroscopy and Sensing. *Annu. Rev. Phys. Chem.* 2007, 58 (1), 267−297.

23. Mie, G. Beiträge zur Optik trüber Medien, speziell kolloidaler Metallösungen. *Ann. Phys.* **330**, 377–445 (1908).

24. Singh Sekhon, J. & Verma, S. S. Refractive Index Sensitivity Analysis of Ag, Au, and Cu Nanoparticles. *Plasmonics* **6**, 311–317 (2011).

25. Ahamad, N., Bottomley, A. & Ianoul, A. Optimizing refractive index sensitivity of supported silver nanocube monolayers. *J. Phys. Chem. C* **116**, 185–192 (2012).

26. Stefan Kooij, E. & Poelsema, B. Shape and size effects in the optical properties of metallic nanorods. *Phys. Chem. Chem. Phys.* **8**, 3349–3357 (2006).

27. Grillet, N. *et al.* Plasmon coupling in silver nanocube dimers: Resonance splitting induced by edge rounding. *ACS Nano* **5**, 9450–9462 (2011).

28. Bottomley, A., Prezgot, D., Coyle, J. P. & Ianoul, A. Dynamics of nanocubes embedding into polymer films investigated: Via spatially resolved plasmon modes. *Nanoscale* **8**, 11168–11176 (2016).

29. Gale-Mouldey, A., Jorgenson, E., Coyle, J. P., Prezgot, D. & Ianoul, A. Hybridized plasmon resonances in core/half-shell silver/cuprous oxide nanoparticles. *J. Mater. Chem. C* **8**, 1852–1863 (2020).

30. Prezgot, D., Bottomley, A., Coyle, J. P. & Ianoul, A. Unusually Sharp Localized Surface

Plasmon Resonance in Supported Silver Nanocrystals with a Thin Dielectric Coating. *J. Phys. Chem. Lett.* **8**, 5555–5558 (2017).

31. Nicoletti, O. *et al.* Three-dimensional imaging of localized surface plasmon resonances of metal nanoparticles. *Nature* **502**, 80–84 (2013).

32. Sheldon, M., van de Groep, J., Brown, A., Polman, A. & Atwater, H. Plasmoelectric potentials in metal. *Science (80-.).* **346**, 1–5 (2014).

33. Van De Groep, J., Sheldon, M. T., Atwater, H. A. & Polman, A. Thermodynamic theory of the plasmoelectric effect. *Sci. Rep.* **6**, 1–12 (2016).

34. Li, J. *et al.* Plasmon-induced resonance energy transfer for solar energy conversion. *Nat. Photonics* **9**, 601–607 (2015).

35. Cushing, S. K. *et al.* Controlling Plasmon-Induced Resonance Energy Transfer and Hot Electron Injection Processes in Metal@TiO 2 Core–Shell Nanoparticles. *J. Phys. Chem. C* **119**, 16239–16244 (2015).

36. Brongersma, M. L., Halas, N. J. & Nordlander, P. Plasmon-induced hot carrier science and technology. *Nat. Nanotechnol.* **10**, 25–34 (2015).

37. Wu, K., Chen, J., McBride, J. R. & Lian, T. Efficient hot-electron transfer by a plasmon-induced interfacial charge-transfer transition. *Science (80-.).* **349**, 632–635 (2015).

38. Bialiayeu, a, Bottomley, a, Prezgot, D., Ianoul, a & Albert, J. Plasmon-enhanced refractometry using silver nanowire coatings on tilted fibre Bragg gratings. *Nanotechnology* **23**, 444012 (2012).

39. Mayer, K. M. & Hafner, J. H. Localized Surface Plasmon Resonance Sensors. *Chem. Rev.* **111**, 3828–3857 (2011).

40. Parente, M. *et al.* Simple and Fast High-Yield Synthesis of Silver Nanowires. *Nano Lett.* (2020) doi:10.1021/acs.nanolett.0c01565.

41. Kelly, K. L., Coronado, E., Zhao, L. L. & Schatz, G. C. The optical properties of metal nanoparticles: The influence of size, shape, and dielectric environment. *J. Phys. Chem. B* **107**, 668–677 (2003).

42. Prezgot, D., Bottomley, A., Coyle, J. P. & Ianoul, A. Unusually Sharp Localized Surface Plasmon Resonance in Supported Silver Nanocrystals with a Thin Dielectric Coating. *J. Phys. Chem. Lett.* **8**, 5555–5558 (2017).

43. Akselrod, G. M. *et al.* Probing the mechanisms of large Purcell enhancement in plasmonic nanoantennas. *Nat. Photonics* **8**, 835–840 (2014).

44. Sherry, L. J. *et al.* Localized Surface Plasmon Resonance Spectroscopy of Single Silver Nanocubes. *Nano Lett.* **5**, 2034–2038 (2005).

45. Novo, C., Funston, A. M., Gooding, A. K. & Mulvaney, P. Electrochemical charging of single gold nanorods. *J. Am. Chem. Soc.* **131**, 14664–14666 (2009).

46. Sayed, M., Zhang, L. & Yu, J. Plasmon-induced interfacial charge-transfer transition prompts enhanced CO_2 photoreduction over Cu/Cu_2O octahedrons. *Chem. Eng. J.* **397**, 125390 (2020).

47. Baffou, G. Thermoplasmonics Heating Metal Nanoparticles Using Light, Cambridge:

Cambridge University Press (2017)

48. Kale, M. J. & Christopher, P. Plasmons at the interface. *Science.* **349**, 587–588 (2015).

49. Chen, L. *et al.* SERS study of surface plasmon resonance induced carrier movement in Au@Cu_2O core-shell nanoparticles. *Spectrochim. Acta - Part A Mol. Biomol. Spectrosc.* **189**, 608–612 (2018).

50. Mukherjee, S. *et al.* Hot electrons do the impossible: Plasmon-induced dissociation of H_2 on Au. *Nano Lett.* **13**, 240–247 (2013).

51. Lee, S. Y. *et al.* Tuning Chemical Interface Damping: Interfacial Electronic Effects of Adsorbate Molecules and Sharp Tips of Single Gold Bipyramids. *Nano Lett.* **19**, 2568–2574 (2019).

52. Foerster, B.; Joplin, A.; Kaefer, K.; Celiksoy, S.; Link, S.; Sönnichsen, C. Chemical Interface Damping Depends on Electrons Reaching the Surface. *ACS Nano* **2017**, *11* (3), 2886–2893..

53. Christopher, P., Xin, H. & Linic, S. Visible-light-enhanced catalytic oxidation reactions on plasmonic silver nanostructures. *Nat. Chem.* **3**, 467–472 (2011).

54. Fu, X., Jiang, T., Zhao, Q. & Yin, H. Charge-transfer contributions in surface-enhanced Raman scattering from Ag, Ag_2S and Ag_2Se substrates. *J. Raman Spectrosc.* 43(9), 1191-1195 (2012)

55. Lombardi, J. R. & Birke, R. L. A Unified Approach to Surface-Enhanced Raman Spectroscopy. *J. Phys. Chem. C* **112**, 5605–5617 (2008).

56. Corson, E. R. *et al.* In Situ ATR-SEIRAS of Carbon Dioxide Reduction at a Plasmonic Silver Cathode. *J. Am. Chem. Soc.* **142**, 11750–11762 (2020).

57. Mohamed, M. B., Volkov, V., Link, S. & El-Sayed, M. a. The `lightning' gold nanorods: fluorescence enhancement of over a million compared to the gold metal. *Chem. Phys. Lett.* **317**, 517–523 (2000).

58. Mun, J., Lee, D., So, S., Badloe, T. & Rho, J. Surface-enhanced spectroscopy: Toward practical analysis probe. *Appl. Spectrosc. Rev.* **54**, 142–175 (2019).

59. Dubi, Y., Un, I. W. & Sivan, Y. Thermal effects - an alternative mechanism for plasmon-assisted photocatalysis. *Chem. Sci.* **11**, 5017–5027 (2020).

60. Aizpurua, J. *et al.* Theory of hot electrons: general discussion. *Faraday Discuss.* **214**, 245–281 (2019).

61. Baffou, G., Bordacchini, I. & Baldi, A. Simple experimental procedures to distinguish photothermal from hot-carrier processes in plasmonics. *Light Sci. Appl.* **9**, 108 (2020).

62. Pelli Cresi, J. S. *et al.* Highly efficient plasmon-mediated electron injection into cerium oxide from embedded silver nanoparticles. *Nanoscale* **11**, 10282–10291 (2019).

63. Petrova, H. *et al.* Time-resolved spectroscopy of silver nanocubes: Observation and assignment of coherently excited vibrational modes. *J. Chem. Phys.* **126**, (2007).

64. Pelli Cresi, J. S. *et al.* Ultrafast Formation of Small Polarons and the Optical Gap in CeO_2. *J. Phys. Chem. Lett.* **11**, 5686–5691 (2020).

65. Link, S., Burda, C., Mohamed, M., Nikoobakht, B. & El-Sayed, M. Femtosecond transient-

absorption dynamics of colloidal gold nanorods: Shape independence of the electron-phonon relaxation time. *Phys. Rev. B - Condens. Matter Mater. Phys.* **61**, 6086–6090 (2000).

66. Du, L., Furube, A., Hara, K., Katoh, R. & Tachiya, M. Ultrafast plasmon induced electron injection mechanism in gold-TiO_2 nanoparticle system. *J. Photochem. Photobiol. C Photochem. Rev.* **15**, 21–30 (2013).

67. Link, S. & El-Sayed, M. A. Spectral Properties and Relaxation Dynamics of Surface Plasmon Electronic Oscillations in Gold and Silver Nanodots and Nanorods. *J. Phys. Chem. B* **103**, 8410–8426 (1999).

68. Staleva, H. & Hartland, G. V. Vibrational Dynamics of Silver Nanocubes and Nanowires Studied by Single-Particle Transient Absorption Spectroscopy. *Adv. Funct. Mater.* **18**, 3809–3817 (2008).

69. Fowler, R. H. H. The Analysis of Photoelectric Sensitivity Curves for Clean Metals at Various Temperatures. *Phys. Rev.* **38**, 45–56 (1931).

Utilizing silver bromide as a photogenerated halogen source for the activation of methane looks promising. Such a process would allow production of higher order hydrocarbons from methane with a side product of hydrogen, while allowing for securing the reactor by turning off the light source. The photolysis of silver bromide was used to produce bromine radicals which could react with methane to produce hydrogen bromide and methyl bromide. The goal was to then couple the methyl bromide over a solid acid to produce higher order hydrocarbons species, while reacting the hydrogen bromide with silver to regenerate the silver bromide and release hydrogen. Unfortunately, the investigations of the process showed that it was not feasible at 1 bar, as the needed illuminated surface area to volume ratio was 58 m^2/L. It was confirmed that hydrogen bromide would react with silver to release hydrogen; however, a highly acidic liquid was also deposited in the reactor. While it may be possible to produce a viable catalytic process, it was not with our present set-up.

Silver Bromide and Methane: the 100-year-old chemistry that will likely never be a modern process

1 Introduction

Long has it been known that silver salts are photosensitive; with 18th and 19th century scholars observing the precipitation of black particles after the illumination of silver chloride and silver nitrate – discoveries which would lead to the development of photography.[1] Substantially more recently, the kinetic parameters of the photodissociation of halogens and subsequent reaction with methane,[2] and the phototarnishing of silver by both methyl and acidic gaseous halides have been reported.[3,4] The conversion of functionalized methane (CH_3OH, CH_3Br, etc.) into higher order hydrocarbons over solid acids was realized in the 1970's.[5a] Finally, all the chemistry can form the basis for development of a process in which a solid silver halide is irradiated to produce halide radicals which react with methane, selectively to the mono-halogenated compound, such as methyl bromide. Methyl bromide then couples over a solid acid to produce ethylene and a halogen acid gas, such as hydrogen bromide. Hydrogen bromide tarnishes the silver releasing hydrogen gas, and starts the cycle anew. Despite all this chemistry being well researched, realization of this cycle (Figure 1) has not yet occurred.

Why might one desire such a process? Simple: while methane is found in great abundance in natural resources such as natural gas and oil reserves, it is not terribly useful as a chemical feedstock – owing to the high stability. Essentially all chemistry with methane as a feedstock relies on the so called methane-steam reforming process, in which synthesis gas (CO and H_2) is produced. This can be further processed to form methanol, or long chain hydrocarbons by the Fisher Tropsch process. Methane steam reforming is very energy intensive, and significant amounts of CO_2 are released. Halide chemistry can lead more efficiently to desired intermediates. Methyl bromide fills this role as an intermediate towards ethylene production, and thereby a myriad of plastic and oil products.

One might remark that not all processes of the previously indicated cycle need realization, and indeed, it has been achieved through a thermal process of halide gas and methane over a solid acid[6,7]; however, it is well known that accidents can occur, and when working with halide gases, this can be catastrophic. Using a silver halide under illumination instead of a gaseous halide at high temperature would allow for two major benefits. First, no gaseous halogens are present without light, that is, when the light is off, the reactor is (relatively) safe. Second, the immediate release of

[a] While this article is from 1986, it refers to an article from the1970's which first realized the discovery (Meisel, S.L, CHEMTECH, 1976), the original article is not readily available.

hydrogen from the hydrogen halide gas as it reacts with the silver. These benefits merited investigation into realizing a silver halide and solid acid catalytic process for the coupling of methane. A more detailed description of the chemistry and several preliminary data are reported in this chapter.

Contributions to this chapter have been made by Ilya Konter (former MSc student), and Jasper Stook (former BSc student), and are cited to their respective theses.

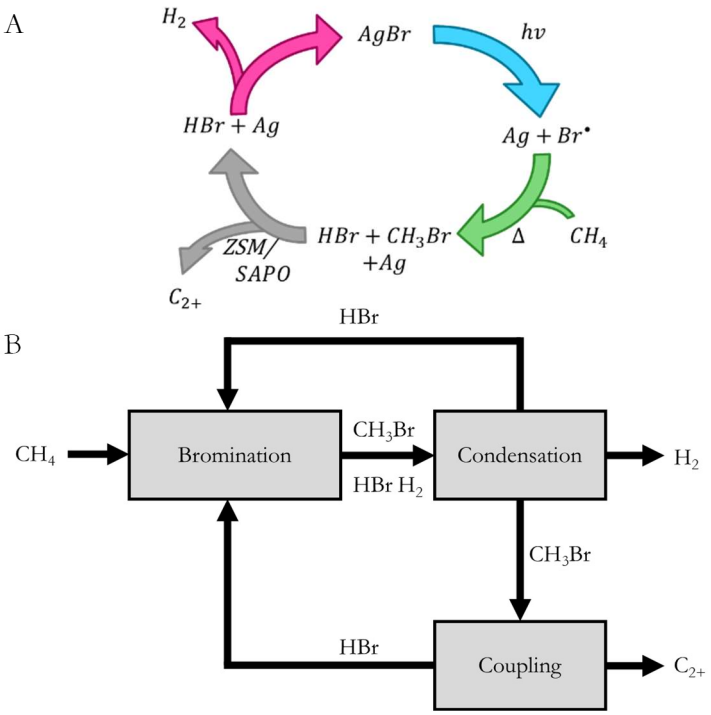

Figure 1: Catalytic process for the conversion of methane into higher order hydrocarbons through bromination. A) chemical reactions looped in the proposed process. B) scheme showing proposed steps for the process.

2 The established chemistry

The proposed catalytic process is to use silver bromide as a bromine source for the coupling of bromine by way of methyl bromide. The catalytic steps are described by:

A. $AgBr_{(s)} + h\nu \rightarrow \frac{1}{2}Br_{2(g)} + Ag_{(s)}$

B. $Br_{2(g)} + h\nu \rightarrow 2Br\bullet_{(g)}$

C. $Br\bullet_{(g)} + CH_{4(g)} \rightleftarrows HBr_{(g)} + \bullet CH_{3(g)}$

D. $\bullet CH_{3(g)} + \frac{1}{2}Br_{2(g)} \rightarrow CH_3Br_{(g)}$

E. $CH_3Br_{(g)} \rightarrow \frac{1}{2}C_2H_{4(g)} + HBr_{(g)}$

F. $Ag_{(s)} + HBr_{(g)} \rightarrow AgBr_{(s)} + \frac{1}{2}H_{2(g)}$

To understand this proposed system, we will begin with the processes involving the conversion (A) and formation (F) of AgBr (section 2.1), before discussing bromine photolysis (B, section 2.2), methane functionalization (C and D, section 2.3), and methyl bromide coupling (E, section 2.4). Reactions B-D are classic radical reactions: initialization (B), propagation (C, and D when reacting with Br_2 to produce Br•) and termination (D, when reacting with Br•).[2]

2.1 Silver halide photo reactivity

It is well established that silver salts react under illumination, creating a dark surface in solid salts, and dark precipitates in solutions. Indeed, in a 1777 correspondence this effect was noted for silver halide salts, and in 1802 for silver nitrate.[1] This phenomenon gave rise to the development of photography, as this photo-decomposition allowed for the selective removal of portions of silver salt – the so-called latent image effect. The name "latent image" was given because the image remained invisible until developed: the removal of unexposed silver halide, and the further reduction of the exposed silver halide revealed the image.[8] Since the invention of photography was revolutional, and silver halides featured prominently, the photo-dynamics of silver halides have been well studied.[1,9–12] While photography has benefited from the light-induced reduction of silver, in the context of this work it is the light-induced release of halide which is of interest. Fortunately, it was silver bromide that was used in photography, as will be discussed later, as bromide is highly desirable for the photocatalytic process conceived here.

The decomposition of AgBr after photoexcitation stems from the ionic nature of the silver bromide bond.[13,14] The indirect band gap of AgBr is 2.7 eV, but for particles smaller than 7 nm, this bandgap is size-dependent and increasing with decreasing size.[12,15] The absorption of light causes a Br p→ Ag d electronic transition.[13] Photoelectrons could migrate to grain boundaries, becoming trapped

in defect sites, and ultimately reducing a silver atom.[8] Photogenerated holes become trapped at silver vacancies before oxidizing bromine.[16]

The limiting factor in the utilization of silver bromide in the context of the proposed process is the available bromine per unit illuminated surface area. Initially the absorption cross section of silver bromide will determine the penetration depth of light, but during continuous illumination silver particles will form on the surface, creating a more complicated optical environment. Silver particles are known to be plasmonic, and exhibit an absorption cross section many times their physical cross section.[17] This will limit the absorption of light and subsequent release of bromine to a penetration depth less than the order of the wavelength of light (owing to the exponential decay of the evanescent waves, and trapping of the incident light in plasmonic hotspots).[17] Given the properties of AgBr, assuming a penetration depth on the order of 10 nm (not unrealistic given a film of coupled plasmonic particles)[18] and operating at $50\%_{mol}$ Br_2 at 600 K and 1 bar, a surface area to volume ratio of 58 m^2/L is required. This translates into a volume of Br_2 at STP[b] of 250 mL of bromine gas per square meter illuminated.

If AgBr is thought of as the starting point of the proposed catalytic process, then to close the catalytic cycle it must be regenerated: the light-induced silver must react with brominated species. Silver spontaneously reacts with both gaseous halide acids and organo-halides at reasonable temperatures – but slowly. This reaction can be accelerated through phototarnishing.[3,4]

Phototarnishing is separate from photolysis of the gaseous halogen species; with photolysis of HBr and CH_3Br occurring for light well into the UV regime (occurring with photon energies exceeding 4 eV). Instead, phototarnishing is a different route for the electronic relaxation of silver bromide: the photogenerated electron from the AgBr reduces a bromine atom in HBr or CH_3Br rather than a silver atom in AgBr. This process is understood to be linearly dependent on the number of absorbed photons, and independent of temperature (for a range between 25-200°C).[4] This means that the continued illumination of silver bromide, after the release of bromine and subsequent formation of silver metal, can readily oxidize gas phase bromine species to regenerate AgBr (reaction F in the above scheme). In the case of HBr, this will release the desirable product of H_2, and in the case of CH_3Br, this will release a methyl radical – which is an intermediate in the bromination of methane (this will be discussed more in section 2.3 of this chapter).[19] Accordingly, the phototarnishing effect will benefit the proposed process by accelerating the regeneration of AgBr and releasing H_2 which recovers available bromide.

[b] IUPAC standard ambient temperature and pressure: 0^oC, 100 KPa.[45]

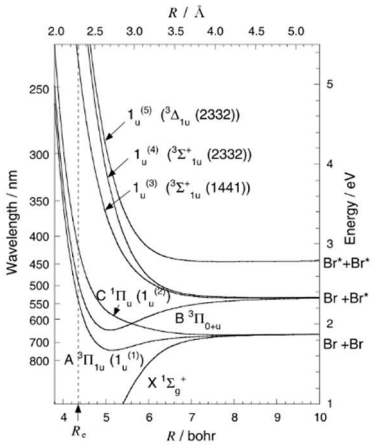

Figure 2: electronic transitions of bromine, reproduced from (Theoretical study of nonadiabatic transitions in the photodissociation of Cl 2 and Br 2)

2.2 Halogen photodissociation

After liberation from AgBr, the bromine must undergo dissociation for rapid reactions with methane; this dissociation can be achieved through a photothermal route. The different halogen gases absorb light with different photon energies: bromine redshifted respective to chorine.[20] It is well established that the electronic transition which accompanies light absorption can result in the photodissociation of the halogen gas.[21] Both of these are key to the proposed photothermal process for methane conversion.

The optical cross sections of chlorine and bromine have been well studied, and the absorption cross section of chlorine is known to be significant between 300 nm and 400 nm, while that of bromine is between 350 nm and 550 nm (with a smaller absorption cross section extending to 700 nm).[20,21] In bromine a photon with a wavelength below ca. 694 nm can excite the molecule from the ground state to the first excited state ($^1\sum^+_g \rightarrow {}^3\prod_u$) and at room temperature optical excitation at 680 nm is sufficient to cause dissociation into 2 ground state bromine radicals. Additional electronic transitions at similar energies exist which can result in the formation of excited bromine radicals as well (Figure 2).[21,22]

The absorption cross section for each electronic transition is also a variable in the photolysis of Br_2. The two spin forbidden transitions, $^1\prod_u$, and $^3\prod_{0u}$ have

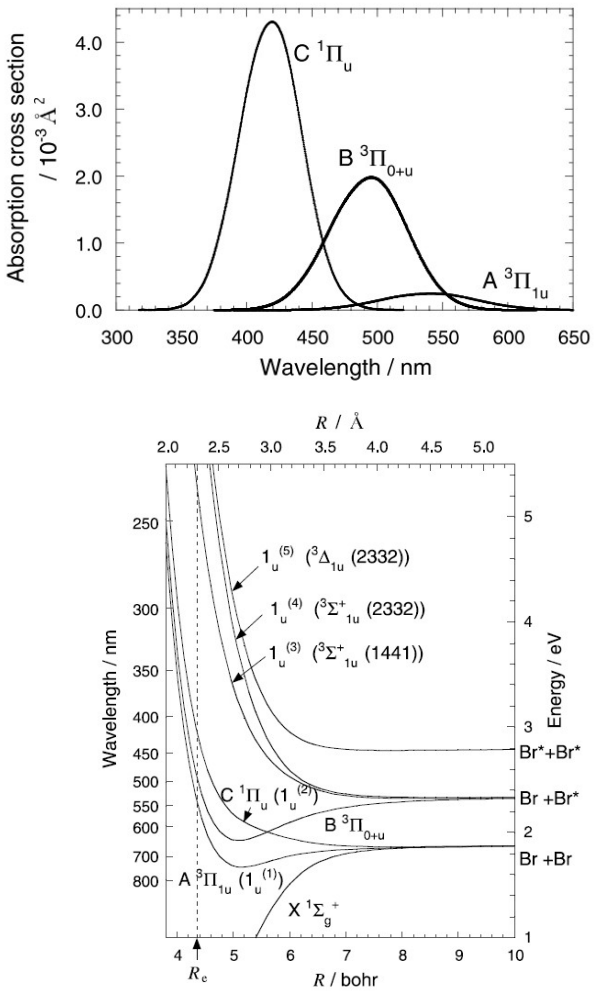

Figure 3: A)absorption cross section of electronic transitions of Br_2, with (B) the associated energy diagram. Reproduced from (Theoretical study of nonadiabatic transitions in the photodissociation of Cl_2 and Br_2)

significant absorption cross sections (Figure 3A); these electronic transitions are allowed due to intensity borrowing.[22] The dissociation caused by one these states, like the $^3\prod_u$, result in two ground state bromine radicals. Excitation to the $^3\prod_{0u}$ state (the B band in Figure 3A), and UV light excitations (200 nm – 280 nm) result in the formation of excited radicals (Br+Br•). Dissociation from both the A or B excitation requires thermal excitation (Figure 3B).[22] Given the deep UV nature of that electronic transition, and that such illumination would interfere with both the

CH_3Br (section 2.3) and silver (inter-band transition of silver metal), it is to be avoided in the proposed process.

2.3 Methane functionalization

The halogenation of methane has been well studied, both the thermal and photothermal routes. One of the major shortcomings of the process is over-halogenation: for economically valuable products such as ethylene a mono-halogenated methane is desired. Balancing over-halogenation is the need to maintain a high conversion to the mono-halogenated species. It is this balancing act which brings bromine to the forefront for the proposed process, as the reactivity of bromine is less than chlorine or fluorine (which form stable, highly substituted methyl halides), but forms sufficiently stable products (methyl iodide can easily decompose to methane in reaction conditions).[19,23]

For fluorine, chlorine, and bromine gases the reaction with methane is exothermic at room temperature.[19] Additionally, for chlorine, the product is a more favourable reagent for halogenation: that is, CH_3Cl is more reactive with Cl_2 than CH_4.[23] Fortunately bromination can be controlled in two ways: thermally, and chemically.[19,24,25] The bromination of methyl bromide is favourable for temperatures below 450°C; above this the reaction is no longer spontaneous.[19] This has been observed throughout literature as a means of controlling the degree of bromination.[24] In contract to thermally controlling the extent of the reaction, one can take advantage of the endothermic nature of iodine to influence the degree of bromination. The use of iodine at temperatures of 500°C increases the selectivity towards CH_3Br; the iodine catalyzes the reaction of CH_2Br_2 with CH_4 to form two monosubstituted methyl bromides.[25] This has been employed in academic studies for the functionalization of methane and other alkanes.[26]

In the bromination of CH_4 to CH_3Br with Br_2, the rate of CH_3Br formation is equal to the rate of loss of Br_2; owing to the formation of HBr. This has allowed, in literature, for the *in situ* monitoring of the degree of reaction through spectroscopic monitoring of $[Br_2]$, and has led to the rate equation of:

$$\frac{d[CH_3Br]}{dt} = -\frac{d[Br_2]}{dt} = \frac{k\prime[CH_4][Br_2]^{1/2}}{P^{1/2}}$$

Where k' is the rate constant multiplied by the spectral absorption and apparatus constant, and P is the total pressure of the system.[2] This rate equation is only true for initial conditions; unfortunatley, if the reaction is allowed to progress considerably then secondary reaction and inhibitions from reaction products will occur.[2] Specifically, considering the reactions (not accounting for multiple brominations):

(1) $Br_2+h\nu \rightarrow Br+Br$
(2) $Br+CH_4 \rightarrow CH_3+HBr$
(3) $CH_3+Br_2 \rightarrow CH_3Br$
(4) $CH_3+HBr \rightarrow CH_4+Br$
(5) $2Br+M \rightarrow Br_2+M$

Where M is any gas phase species with which bromine can relax through collision. Then the steady state rate of methyl bromide formation is given by[2]:

$$\frac{d[CH_3Br]}{dt} = \frac{k_2[CH_4]\left({}^{n}/_{k_5}[M]\right)^{1/2}}{1+\frac{k_4[HBr]}{k_3[Br_2]}}$$

Knowledge of the rate laws allows for a degree of control on the reaction and specifically the knowledge that a reduced pressure and removal of products increases the rate of reaction (as reactions (2) and (4) are an equilibrium of the bromine and methyl radicals).

Thermal control of this reaction can be further aided through the introduction of light. The photolysis of bromine results in radicals which can react with the methane.[2,27] This has been shown to be a photothermal reaction with significant enhancement from light stimulation.[2] As has been discussed for bromine, the effect of absorbing a photon can result in decomposition of the species. To ensure that desired products will not be decomposed, light in the spectral regime where methyl bromides absorb must be minimized with respect to the visible light intensity. The mono- and di-substituted methyl bromide species have considerable absorption for wavelengths below 300 nm, with a peak at 200 nm.[28] This allows for a simple method of using primarily visible light excitation to drive the photocatalytic portion of the process. Should the methyl bromide be illuminated with sufficiently energetic light (λ<185 nm, 6.7 eV) then the photolysis of CH_3Br will occur: forming HBr and CH_2. Unfortunately this photolysis of methyl halides alone produces predominantly methane, rendering this as a non-desirable route towards higher-order hydrocarbons.[29]

2.4 Solid acids for coupling

With methyl bromide produced from methane, coupling it into higher-order hydrocarbons is needed. Fortunately, in keeping with the theme of this chapter, this as well is established chemistry. Early work demonstrated the conversion of methyl bromide into higher order hydrocarbons though the use of a solid acid in the

presence of water and Br_2.[5,23] More recent work shows an anerobic conversion to higher order hydrocarbons over cobalt loaded SAPO-34[c].[6,24,30]

Early work by Olah and others showed that it was possible to both functionalize methane with halides over a solid acid, but also to couple the formed methyl halide into C_2 species in the presence of water.[5,23,31] Over many of the established catalysts, this process has losses of carbon atoms to the formation of CO_x due to the presence of oxygen species.[32] One approach to solve this limitation is to work in anerobic conditions for all carbon containing steps.[33] Much like other anaerobic methane coupling processes, these produce a non-trivial amount of aromatic hydrocarbons.[6,34,35]

More recent work has used an oxygen source which is less reactive with carbon species, but still active in bromine sequestering: CaO.[6] This allows for a separate step of oxidative recovery of the bromine. A drawback of this approach is that processing is needed to separate the bromine from the water formed from HBr decomposition; or, if the CaO is incorporated with the solid acid, then oxygen species (water) is still present in the reaction chamber. A solution to this is to use a bromine sink which is also the bromine source: silver bromide.

The mechanism which allows for the coupling of the methyl bromide is the same as that which allows for methanol to be coupled: acid/base sites on the solid acid. The CH_3X (where X is either Br or OH) binds to a surface OH group, releasing HX.[23] This methyl group is akin to a stabilized methyl radical, which reacts to form higher order hydrocarbons. Zeolites are well known to limit reactions based on size, however they can suffer from coke buildup in the pores. This can be resolved by cofeeding methane and methanol;[36] fortunately, reported bromination of methane is limited so co-feeding CH_4 and CH_3Br would inherently occur in such a process.[24,25,30]

The solid acid selected will influence the temperature regime that is ideal for higher hydrocarbon production. SAPO-34 has good selectivity for C_{2+} (>50%) up to 500°C,[30] while ZMS-5[d] has similar selectivity below 240°C.[34] The precise selectivity for higher order hydrocarbons does depend on the solid acid, and is influenced by co-catalysts used.[5,30,34]

3 The proposed process

With all the individual steps described, now it is possible to examine the overview for the proposed coupling of methane through a photo-thermal

[c] A specific silico-alumino-phosphate molecular sieve.[46,47]
[d] Zeolite Socony Mobil–5[48]

bromination (Figure 1**Error! Reference source not found.**). The thermal limitation comes from the bromination step, by operating at ≥450°C limits the dibromide formation while allowing mono-bromination to occure. The spectrum of the light source should enable Br_2 and AgBr photoexcitation, which could be realized by utilizing visible light (>400 nm) exclusively and avoiding deep UV radiation (<300 nm) to prevent excitation of CH_3Br. The coupling of methyl bromide over a solid acid should be separated from the bromination step to minimize the bromination of higher order hydrocarbons, this can be achieved through condensing as methyl bromide boils near freezing at 1 bar. The release of hydrogen from the decomposition of HBr over silver functions at elevated temperatures and under illumination. and can be concurrent with bromination. A feedback loop to recycle the HBr formed in coupling can return the bromine to the reaction chamber.

4 Experimental apparatus

4.1 Chemicals used

Ammonium hydroxide (ACS reagent grade 28-30%, Sigma), (D)-glucose (99.5%, Sigma), hydrobromic acid (47-49%, Alfa), Methane (HiQ 5.5, Linde), Nitrogen (from liquid nitrogen, Praxair), silver bromide (99.5%, Alfa), silver nitrate (99%, Sigma), and Sodium hydroxide (98%, Sigma) were used.

4.2 Apparatus used

Gas wash bottles (500 mL,Corning) were used as batch reactors, and a high pressure Hg lamp (HP-120 Opsytec) was used as the light source. The light source produces 4 W of UV-A, and 8 W across the UV-Vis regimes (spectra shown in Figure *4*a). No filter was used; however, as the gas wash bottle used as a reactor is Pyrex and not quartz, considerable amounts of the UV regime would be attenuated.

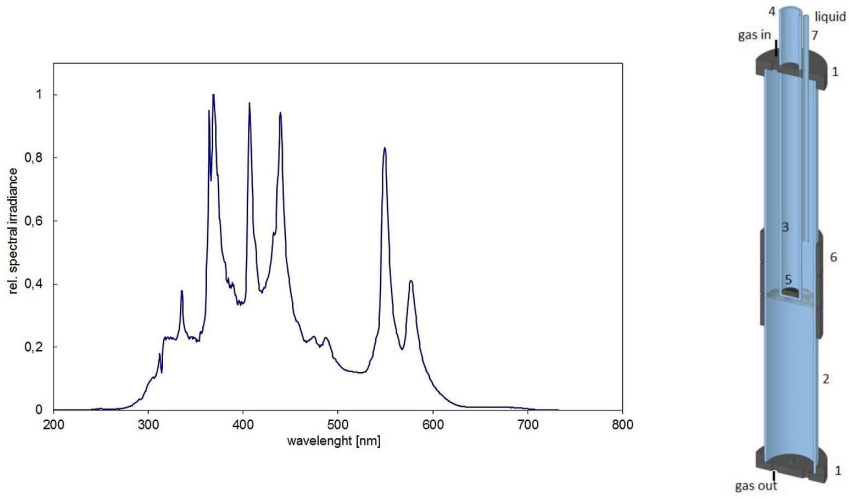

Figure 4: A) Spectral output of the HP-120, reproduced from opsytec.com. B) Scheme of the annular reactor used in later experiments, reproduced from reference 42 (MSc of Ilya Konter)

Later experiments were performed in an annular reactor (Fig. 4b), made inhouse. This reactor was comprised of steel fittings (1) holding a glass tube (2) 50 cm tall with a 3 cm radius; inside this tube, a quartz tube sealed at one end functioned as a light pipe (3) with a 1 cm radius, 45° steel conical mirror (5). Swagelok fittings allowed the controlled introduction of gas (4) and a 6 mm diameter glass tube (7) allowed the introduction of liquids. The reactor had a frit, which acted to hold the catalyst bed, around which band heaters were (6) mounted and surrounded with insulation. The reactor was filled with glass beads to reduce the dead volume to 590 mL. The light from the HP-120 source was directed into the annular reactor and directly illuminated a 1 cm tall region.

4.3 Methods

Thin films of silver were produced through silver deposition using Tollen's reagent (the commonly called 'Silver Mirror Experiment'). Briefly, a solution of silver nitrate was mixed with ammonium hydroxide, forming first a dark precipitate which is then dissolved with the addition of more ammonium hydroxide. Sodium hydroxide was added forming a dark precipitate; the precipitate was redissolved using a minimum of ammonium hydroxide. This solution containing $[Ag(NH_3)_2]^{+}_{(aq)}$ was used to deposit silver metal through exposure to glucose.[37] This method was used to coat both reactors, and beads. This produced a nice silver coating, which when coating the inside of the gas wash bottle produced a mirrored finish from the outside. The coating of the beads resulted in a film which was clearly roughened silver, and varied from a dark black colour to a white finish. SEM of the beads revealed that all coloured beads had silver, but the amount of silver varied (Figure 5).[e] Reactions used $5\%_{v/v}$ methane in nitrogen.

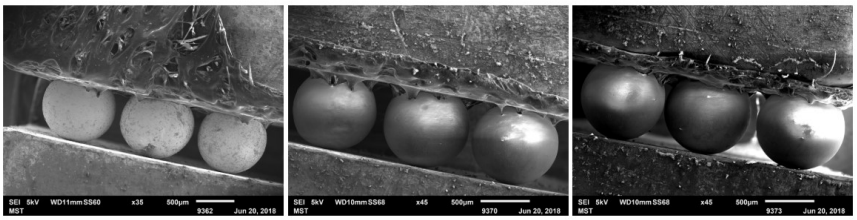

Figure 5: SEM images of glass beads. (a) thick films of silver resulting in bright coloured beads which reflected light. (b) a thin layer of silver which resulted in attenuation of light. (c) uncoated glass beads which transmit and scatter light through refraction. SEM images reproduced from the thesis of J. Stook.

5 Results, challenges, and how they might be faced

While AgBr may have a high absorption coefficient, it pales in comparison to the absorption cross section of silver nanoparticles which form because of AgBr photoexcitation. These silver nanoparticles exhibit plasmonic behaviours (intense absorption and scattering), and limit light penetration into AgBr. Plasmonic particles can have long ranging modes (such as the propagating modes found in nanowires), but in series of particles, light propagation perpendicular to a surface of particles has a minimal penetration depth.[18] For this reason, in this reaction thin films of AgBr are used, rather than powder loaded reactors.

[e] For additional information on the bead coating, please refer to the thesis of J. Stook.

5.1 Coated batch reactors: AgBr

Preliminary studies were performed using a silver coated gas wash bottle with AgBr placed in the bottom as a batch reactor. It was filled with 1 Bar of 5%$_{v/v}$ CH_4 in N_2 and illuminated with a high-pressure mercury lamp, and check valves were in place before and after the reactor. The reactor was wrapped in a heating filament, which was controlled by a simple feedback loop with a thermocouple. There was uneven effect of illuminating AgBr, and the location directly illuminated would be fully transparent after the 1-hour reaction. The rest of the AgBr varied in colour, indicating inhomogeneous reaction due to the uneven illumination. After the reaction, a portion of the product was fed into a gas chromatogram with flame ionization detection (GC-FID) for analysis.

These preliminary results (an example of them is shown in Figure *6*) showed no evidence of AgBr photoactivity towards CH_3Br; however, there was evidence that the intense illumination of the reactor when charged with methane resulted in methanol production. Interestingly, more CH_3Br was observed on initial contact with the hot AgBr, even when in the dark, evidence of a thermal reaction between AgBr and CH_4.

The preliminary results were plagued with issues, including small leaks of the observable CO_2 (the GC-Fid was equipped with a methanizer), and likely other atmospheric gasses (most notably oxygen was suspected to leak in, as to account for the production of both methanol, and CO_2 during illumination). The photochemical production of methanol may have stemmed from the high energy and high intensity output of the Hg-lamp, where oxygen may become excited, forming oxygen radicals and ozone (an observation for which further evidence is obtained in later

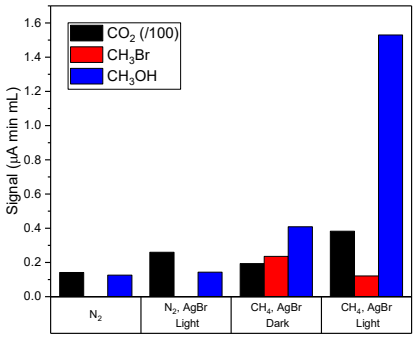

Figure 6: Preliminary results from direct illumination of AgBr in a heated reactor filled with 1 Bar of 5%$_{v/v}$ CH_4. The persistent CO_2 signal was due to leaks, and very little product was observed. Further, no evidence of photocatalysis to form CH_3Br was observed.

experiments showcased in section 5.2).[38] Alternatively, some humidity might have caused activation to hydroxyl radicals, known to react with hydrocarbons to alcohols.

The low yield of products is understood to be due to the low availability of surface bromide and conversion to bromine, both because of the very low surface area to volume ratio, and due to the inhomogeneous illumination of the reactor. To address this in part, HBr was flowed into the reactor. Since the vapour pressure of HBr above 49% $HBr_{(aq)}$ is only ~100 ppm, the concentration was unfortunately low. Introduction of HBr also added water vapour into the reaction medium, which could become photoexcited and react with the methane. Overall, little change in product distribution as compared to Figure 6 was observed.

5.2 Coated Reactors: Ag + $HBr_{(g)}$

In shifting to a mirror batch reactor from an AgBr coated one, reproducibility increased; however, the issue of methanol formation was retained (Figure 7). It should be noted that the amount of methanol produced was minimal (on the order of <10 ppm), although greater than CH_3Br formation (~1 ppm). The reaction suffered from low yields, compounded by the stress the reaction put on the GC-FID (corrosive halogen species), which made quantification difficult. To alleviate both issues, a new system was made, which used a (corrosion resistant) online mass spectrometer (MS) and an annular reactor packed with silver coated glass beads. In this way, both the poor detection and the low yield were thought to be addressed.

5.3 Mirrored beads

The move to mirrored beads came from the estimation of the needed surface area to volume ratio. For a suitable productivity, [Br•] or [Br_2] should be on the same order of magnitude as [CH_4]. As highlighted above regarding the low penetration depth into AgBr once silver nanoparticles form, an estimation of a 10 nm penetration depth was used to determine the surface area (SA) to volume (V) ratio. To determine the surface area of AgBr (and so the SA of Ag needed) the ideal gas law was used (at 600K), with ρ_{AgBr}=6.473 g/cm^3, and M_W=187.77 g/mol. To produce 0.5 bar of Br_2 a surface area of 58 m^2/L is needed.

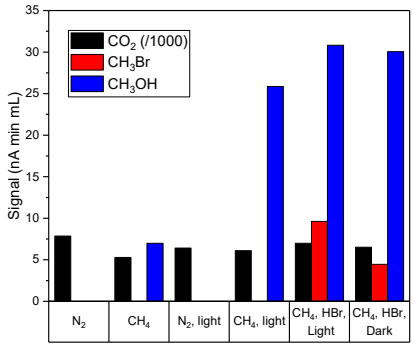

Figure 7: Products formed during reactions in a silver coated reactor, $HBr_{(g)}$ was fed in as a reagent by bubbling N_2 through 49% $HBr_{(aq)}$.

For a cylindrical annular reactor with internal radius r, external radius R, and height (h) the volume inside the reactor which could be filled with gas (V_g), and SA is simply given:

$$V_g = \pi h(R^2 - r^2), \qquad SA = 2\pi \Re h$$

Where $\Re$ is the radius of the coated surface (r, or R). This gives a SA/V ratio of:

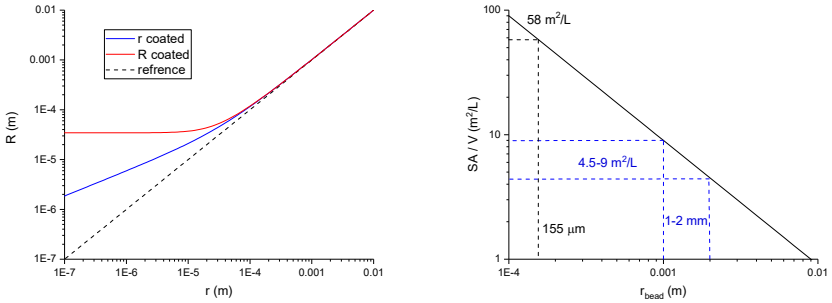

Figure 8: A) scaling of outer radius with inner radius for both coated inner and outer surfaces in a cylindrical annular reactor. The dashed line represents unity, where R=r. B) Surface area to volume ratio of a packed bed depending on spherical bead size. The dashed lines represent the relevant sizes: to achieve 58 m^2/L at 155 µm, and the SA/V ratio with 1-2 mm beads. Both plots are on log-log scales.

$$\frac{SA}{V} = \frac{\Re}{R^2 - r^2}$$

Solving this for the needed 58 m^2/L gives a range of viable radii (Figure 8a); unfortunately, the radii are not practical. For a coated outer surface, the solution tends towards the solution for the SA/V for a cylinder (R~35 μm). This is preferential as compared to if the inner surface is coated which requires a smaller outer diameter; using an optical fibre for the inner radius (r=62.5 μm) would require an outer radius of only 78 μm. Clearly then, the open annular reactor is unsuitable, and a packed bed is considered.

Ideal packing of spheres gives $V_{filled} = {}^{\pi}/_{3\sqrt{2}} \cong {}^{3}/_{4}$.[39] This gives the volume of a bead (V_b) the surface area of a bead (SA_b), the number of beads (n), and ultimately the solution for the SA/V as a function of the bead radius (r_b):

$$V_b = \frac{4}{3}\pi r_b^3, \quad SA_b = 4\pi r_b^2, \quad n = \frac{{}^{3}/_{4}\, V_g}{V_b}$$

$$\frac{SA}{V} = \frac{SA_{total}}{V_g - V_b} = \frac{n\, SA_b}{{}^{1}/_{4}\, V_g} = \frac{{}^{3}/_{4}\; SA_b \; {}^{V_g}\!/_{V_b}}{{}^{1}/_{4}\, V_g} = \frac{3\, SA_b}{V_b} = \frac{3 * 4\pi r_b^2}{{}^{4}/_{3}\, \pi r_b^3} = {}^{9}/_{r_b}$$

Which gives a bound of r_b< 155 μm beads to achieve a SA/V ratio of 58m^2/L (Figure *8*b). Using beads with r=0.5-1 mm which were readily available and allow some transmission of light, a surface area to volume ratio of ~4.5-9 m^2/L is possible.

Use of the beads prevents uninterrupted transmission of light; not only do the beads themselves scatter, refract and reflect light, but the addition of a silver (or silver bromide) film furthers this attenuation. Despite this, a brief preliminary test was run using the batch reactor for 3.1.

The preliminary runs through the mirrored beads, used a stream of CH_4, and N_2 to give 100 ppm of $HBr_{(g)}$; the results are consistent with section 3.1, where the order had a greater effect on the production of CH3Br than anything else (Figure 9). Despite continually supplying HBr(g) which should react with the silver, subsequent runs did not produce notable amounts of CH_3Br. Additionally, no

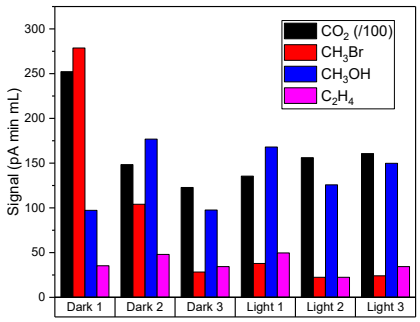

Figure 9: Mirrored beads in a heated gas wash bottle were exposed to CH_4 N_2 and $HBr_{(g)}$. Illumination has no observable effect on the production of CH_3Br; however, the production is greatest for the first run, and lowers with subsequent runs.

significant effect of illumination was observed for any products, unlike in previous studies, where an increase in methanol was observed. This is indicative of a non-catalytic process, but instead one where a reagent is consumed. Likely there was some oxygen (subsurface oxygen in silver has been shown to be relevant in oxidative methane coupling)[40] or other reactive species which participated in the reaction, which were consumed. Trace amounts of C_2H_4 were observed; however, it is suspected that this stems from decomposition of plastics in the set-up (despite using chemically resistant plastics, the $HBr_{(g)}$ would dissolve the plastics much like dichloromethane would). This contamination let part of the design of the new reactor which was studied in the MSc of I. Konter, and discussed in section 5.5.

5.4 Characterization of optical attenuation of mirrored beads[41]

The optical attenuation induced by the beads was briefly examined.[f] The attenuation of light through a 1 cm cuvette was examined, and the scattering was estimated by monitoring the intensity perpendicular to the light path through the cuvette (Figure 10).

[f] The investigation was carried out as the BSc assignment of J. Stook under the supervision of D.B. O'Neill, 2018

The average attenuation between 350 nm to 550 nm was compared, along with the effects of fluidization (Figure 10a); fluidization was investigated to allow for the switch between SA/V and light intensity. The uncoated beads had considerable attenuation, with an attenuation of ~2 OD/cm, attributed to scattering. The addition of silver resulted in additional attenuation; mixture of coated and uncoated beads was made to give approximately 25%, 50%, 75%, and 100% coated samples. The attenuation through 1 cm of fully coated beads was ~2.8 OD, 0.8 OD greater

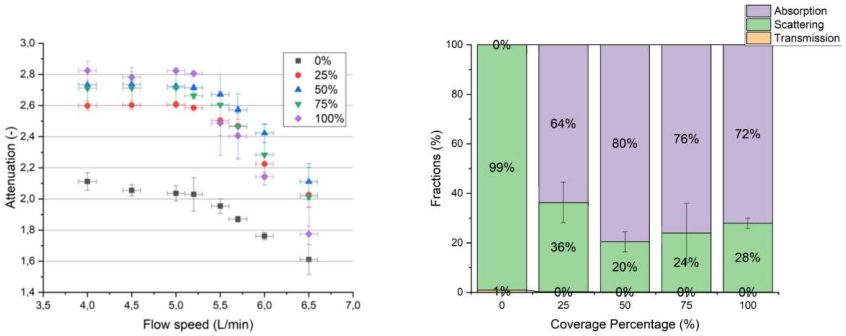

Figure 10: A) Attenuation through a 1 cm path of glass beads coated with varying amounts of silver metal. Before fluidization at ~5.3 L/min, the attenuation of coated beads is range between 2.6-2.9 OD/cm, as compared to the stationary beads which only attenuate 2.1 OD/cm. B) the transmitted light, estimation of scattered light (0% attenuation assumed for uncoated beads), and attenuation for stationary beads. Figures reproduced from the thesis of J. Stook

than the uncoated beads.

The scattering was estimated by using the intensity from the uncoated beads as the reference for the coated beads scattering profiles. The loss of scattered light observed in samples of beads coated in silver is attributed to absorption by the silver (Figure 10b). While there is little statistical significance to the degree of scattering with silver loading, there is a consistent 60-80% attenuation. In a cylindrical,

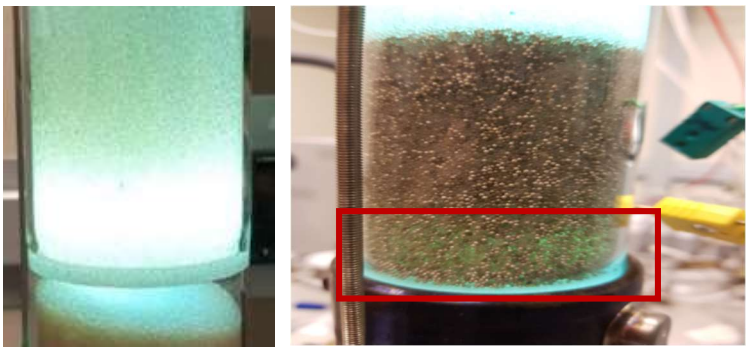

Figure 11: An annular internally illuminated photothermal reactor (insulation and heating mantles lowered) with a 45° conical steel mirror to provide ~1cm illumination, shown with uncoated (A), and 25% silver coated (B) beads. The red box in B is to highlight the ~1cm region which is directly illuminated.

internally illuminated annular reactor scattering is not significantly detrimental, as the majority of the light would remain in the reactor (light scattered out of the left of one segment, would enter through the right of the adjacent segment). This is seen in comparing the annular reactor with uncoated and 25% coated beads (Figure 11).

The effect of bromination of the silver on the optical properties was not examined but given the high degree of attenuation by the coated beads, it was expected that the light penetration would not exceed the reactor. Further, the internally illuminated annular photothermal reactor had issues with chemical contamination owing from the bromine source, an issue which was one of the many reasons why the project was abandoned without significant conversion of methane into methyl bromide.

5.5 An internally illuminated photothermal annular reactor: H_2 from HBr decomposition over Ag

The internally illuminated photothermal annular reactor was investigated as the MSc project.[42,g] Given that the bromination of methane requires the presence of Br•, which is derived from the photoexcitation of AgBr; the formation of AgBr was investigated, and notably, the production of H_2 from the decomposition of HBr was

[g] The investigation was carried out as the MSc assignment of I. Konter under the supervision of D.B. O'Neill, 2018; the study was broader than what is shown in this chapter, including work on thermal conditions inside and around the catalyst bed and reactor.

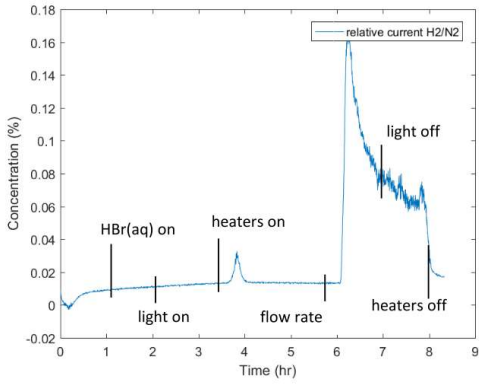

Figure 12: [H_2] output of the annular reactor with $HBr_{(aq)}$ pumped in, with flowing N_2. Room temperature illumination had no effect on H_2 production, once the reactor was heated at close to 3h of operation, a small spike was observed. With an increased $HBr_{(aq)}$ abundance an increase in [H_2] is seen; however, this did not appear to have any photoactivity. Figure reproduced from the thesis of I. Konter

observed. In the reactor 25% Ag coated beads were loaded into the illuminated region (the rest of the reactor was filled with clean, uncoated beads), and 49% $HBr_{(aq)}$ was fed into the reactor by a syringe pump while N_2 was flowed through the reactor. The downstream gas was bubbled through a CaO powder to neutralize any remaining HBr and remove water before being analyzed with the online-MS.

Initially, the cold reactor was purged with N_2 for an hour, the m/z region of 0-50 amu was monitored throughout (Figure 12). The initial flow rate of the $HBr_{(aq)}$ was 116 μL/hr, which was calculated to be the rate at which the water could be fully evaporated in the N_2 flow at room temperature, and so would prevent condensation at the exit of the reactor which was at room temperature. No H_2 production was observed until the reactor was heated, at which point a short-lived spike in the [H_2] is seen (~3.75 hr, Figure 12); this is attributed to the temporary increase in [HBr] as the HBr(aq) volatilized, including a portion in the glass inlet tube. Upon stabilizing, the flow of $HBr_{(aq)}$ was insufficient to observe H_2.

With certainty that no significant concentration of H_2 was being produced, the flow rate of $HBr_{(aq)}$ was increased to 100 μL/min (6 hr, Figure 12). This produced a pronounced effect, where the [H_2] sharply increased. Unfortunately, no effect of light was observed; with both the illuminated and unilluminated rates following the same exponential decay, trending towards a steady-state concentration of 0.063(1)%, or ~0.2% conversion of HBr. This was determined to be a fully thermal reaction as once the heaters were turned off the H_2 signal returned to the baseline.

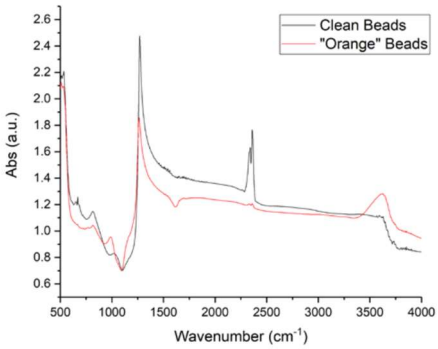

Figure 13: DRIFT spectra of clean, and contaminated beads; very little of note changes in the spectra, with insignificant changes in the 1700-4000 cm^{-1} region, and no significant development of a C-Br peak at ~600 cm^{-1}. A clean silver mirror was used as the spectral reference. Figure reproduced from the thesis of I. Konter

In addition to the small production of H_2, once the reactor was cooled (heating was stopped after 8hr, resulting in the drop in H_2 production), it was found to contain a notable amount of bright orange acidic liquid. Some of the contaminated beads were subjected to Diffuse Reflectance Infrared Fourier-Transform spectroscopy (DRIFT, Figure 13). Specifically, no CH, or CBr bonds were seen on the coated beads, and the only significant changes seen were the presence of water, and changes in the 500-1000 cm^{-1} region. The changes in the 500-1000 cm^{-1} region may be from water, or from other species, but the lack of any CH modes discount dissolved plastics. This suggests that the colour is caused by dissolved Br_2.

6 Prospects for the future

While HBr was observed to produce H_2 (and inferred to produce available Br_2), and methyl bromide was observed, at no point photoactivity was observed. Possibly the lack of photoactivity stems from the difficulty of having sufficient light in an environment with a suitably high surface area to volume ratio. The use of corrosive $HBr_{(aq)}$ or $HBr_{(g)}$ caused significant difficulty, as much of the set-up became disposable, as all steel and plastic components suffered from sever degradation (despite making use of chemically resistant materials, they proved to be only viable for short times). Ultimately, this led to the abandonment of the project.

It may be possible to make the reaction work, but at decreased pressures. In the photothermal reaction of bromine and methane the rate of product formation is inversely proportional to root of the total pressure.[2] In reducing the pressure it

would be possible to both accelerate the rate of methyl bromide production and decrease the needed SA/V ratio to achieve sufficient Br_2 availability. The reduced pressure will have an effect on the rate of regeneration of AgBr and would require actively maintaining the reduced pressure. As such, it is unlikely that there would be significant energetic benefit to the photothermal reaction as compared to a thermal reaction, for which there are established catalysts.[43,44]

7 References

1. Litchfield, R. B. *Tom Wedgwood, the first photographer*. (Duckworth and Co., 1903). pg 188-205

2. Kistiakowsky, G. B. & Van Artsdalen, E. R. Bromination of Hydrocarbons. I. Photochemical and Thermal Bromination of Methane and Methyl Bromine. Carbon-Hydrogen Bond Strength in Methane. *J. Chem. Phys.* **12**, 469 (1944).

3. McTigue, P. T. & Young, D. J. Phototarnishing of silver and copper. *Aust. J. Chem.* **18**, 1851–1853 (1965).

4. Young, D. J. & McTigue, P. T. The phototarnishing of silver and copper. Part II. *Oxid. Met.* **9**, 117–126 (1975).

5. Olah, G. A., Prakash, G. K. S., Ellis, R. W. & Olah, J. A. Remarks on the Mechanism of Ethylene Formation from Methyl Alcohol. *J. Chem. Soc., Chem. Commun*. 9–10 (1986).

6. Lorkovic, I. *et al.* C_1 Coupling via bromine activation and tandem catalytic condensation and neutralization over CaO / zeolite composites, **2**, 566–567 (2004).

7. Lorkovic, I. M. *et al.* Alkane Bromination Revisited : " Reproportionation " in Gas-Phase Methane Bromination Leads to Higher Selectivity for CH_3 Br at Moderate Temperatures. 8695–8700 (2006). doi:10.1021/jp061558h

8. Mitchell, B. Y. J. W. Photographic sensitivity. *Reports Prog. Phys.* **20**, 433–515 (1957).

9. Saunders, V. I., Tyler, R. W. & West, W. Displacement of Photoelectrons and Positive Holes in Sheet Crystals of Silver Bromide as Shown by Development Techniques. *J. Chem. Phys.* **37**, 1126–1132 (1962).

10. Brady, L. E. & Hamilton, J. F. Mechanism of Electron Trapping in Silver Bromide Photographic Grains Dissolving , trapping and detrapping mechanisms of hydrogen in bcc and fcc transition metals Mechanism of Electron Trapping in Silver Bromide Photographic Grains. *J. Appl. Phys.* **37**, 2268–2271 (1966).

11. Malinowski, J. Properties of photoexcited holes in silver bromide crystals Properties of Photoexcited Holes in Silver Bromide Crystals. *Contemp. Phys.* **8**, 285–301 (1967).

12. Scop, P. M. Band Structure of Silver Chloride and Silver Bromide. *Phys. Rev.* **139**, 934–940 (1962).

13. Gordienko, A. B., Zhuravlev, Y. N. & Poplavnoi, A. S. Electronic Structure of AgCl,

AgBr, and AgI. *Phys. Status Solidi* **168**, 149–156 (1991).

14. Glaus, S. & Calzaferri, G. The band structures of the silver halides AgF , AgCl , and AgBr : A comparative study. *Photochem. Photobiol.* **2**, 398–401 (2003).

15. Chen, W. *et al.* Luminescence Properties Of Indirect Bandgap Semiconductors: Nanocrystals Of Silver Bromide. *Mol. Cryst. Liq. Cryst.* **252**, 79–86 (1994).

16. Mallnowski, J. The Role of Holes in the Photographic Process The Role of Holes 1n the Photographic Process. *J. Photogr. Sci.* **16**, 57–62 (1968).

17. Willets, K. A. & Van Duyne, R. P. Localized Surface Plasmon Resonance Spectroscopy and Sensing. *Annu. Rev. Phys. Chem.* **58**, 267–297 (2007).

18. Zhou, W. *et al.* Polarization-dependent properties of the cladding modes of a single mode fiber covered with gold nanoparticles. *Opt. Express* **21**, 245–255 (2013).

19. Degirmenci, V., Uner, D. & Yilmaz, A. Methane to higher hydrocarbons via halogenation. *Catal. Today* **106**, 252–255 (2005).

20. Hubinger, S. and Nee, J.B. Absorption spectral of Cl_2, Br_2 and BrCl between 190 and 600 Nm. *Photochem. Photobiol.* **86**, 1–7 (1995).

21. Tiffany, W. B. Selective Photochemistry of Bromine Using a Ruby Laser. *J. Chem. Phys.* **48**, 3019–3031 (1968).

22. Asano, Y. & Yabushita, S. Theoretical study of nonadiabatic transitions in the photodissociation of Cl_2 and Br_2. *Chem. Phys. Lett.* **372**, 348–354 (2003).

23. Olah, G. A. *et al.* Selective Monohalogenation of Methane over Supported Acid or Platinum Metal Catalysts and Hydrolysis of Methyl Halides over y-Alumina-Supported Metal Oxide/Hydroxide Catalysts. A Feasible Path for the Oxidative Conversion of Methane into Methyl Alcohol/Di. *J. Am. Chem. Soc.* **107**, 7097–7105 (1985).

24. Lorkovic, I. M. *et al.* Alkane bromination revisited: 'Reproportionation' in gas-phase methane bromination leads to higher selectivity for CH_3Br at moderate temperatures. *J. Phys. Chem. A* **110**, 8695–8700 (2006).

25. Ding, K., Metiu, H. & Stucky, G. D. The Selective High-Yield Conversion of Methane Using Iodine-Catalyzed Methane Bromination. *ACS Catal.* 3(3), 474-477 (2013). doi:10.1021/cs300775m

26. Upham, D. C. *et al.* Bromine and iodine for selective partial oxidation of propane and methane. *Appl. Catal. A, Gen.* **580**, 102–110 (2019).

27. Guha, S. & Francisco, J. S. An ab initio study of the hydrogen abstraction reaction of methane by bromine atoms and bromine monoxide radicals. *J. Mol. Struct.* **573**, 171–180 (2001).

28. Mdlna, L. T., Moiina, M. J. & Rowland, F. S. Ultraviolet Absorption Cross Sections of Several Brominated Methanes and Ethanes of Atmospheric Interest. *J. Phys. Chem.*

86, 2672–2676 (1982).

29. Takacs, G. A. & Willard, J. e. Primary Products and Secondary Reactions in the Photodecomposition of Methyl Halides. *J. Phys. Chem.* **81**, 1343–1349 (1977).

30. Zhang, A. *et al.* Improved light olefin yield from methyl bromide coupling over modified SAPO-34 molecular sieves. *Phys. Chem. Chem. Phys.* **13**, 2550–5 (2011).

31. Batamack, P., Bucsi, I., Molnár, Á. & Olah, G. A. Electrophilic chlorination of methane over superacidic sulfated zirconia. *Catal. Lett* **25**, 11–19 (1994).

32. Paunovi, V., Zichittella, G., Moser, M., Amrute, A. P. & Pérez-Ramírez, J. Catalyst design for natural-gas upgrading through oxybromination chemistry. *Nat. Chem.*, **8**, 803–809 (2016).

33. McFarland, E. Unconventional chemistry for unconventional natural gas. *Science.* **338**, 341–342 (2012).

34. Osterwalder, N. & Stark, W. J. Direct coupling of bromine-mediated methane activation and carbon-deposit gasification. *ChemPhysChem* **8**, 297–303 (2007).

35. Li, L., Fan, S., Mu, X., Mi, Z. & Li, C. J. Photoinduced conversion of methane into benzene over GaN nanowires. *J. Am. Chem. Soc.* **136**, 7793–7796 (2014).

36. Liu, Y. *et al.* Efficient Conversion of Methane to Aromatics by Coupling Methylation Reaction. *ACS Catal.* **6**, 5366–5370 (2016).

37. Nuffield Foundation and the Royal Society of Chemistry. A giant silver mirror experiment. (2015).

38. Horowitz, A., Schneider, W. & Moortgat, G. K. The role of oxygen dimer in oxygen photolysis in the Herzberg continuum: a temperature dependence study. *J. Phys. Chem.* **93**, 7859–7863 (1989).

39. Hales, T. C. An overview of the Kepler conjecture. arXiv:math/9811071 [math.MG] (1998).

40. Nagy, A. J., Mestl, G. & Schlögl, R. The Role of Subsurface Oxygen in the Silver-Catalyzed, Oxidative Coupling of Methane. *J. Catal.* **188**, 58–68 (1999).

41. Stook, J. Silver coated glass beads: the influence on optical properties for photocatalysis. (University of Twente, 2018).

42. Konter, I. Characterization of an Internally Illuminated Flow Reactor., University of Twente (2018).

43. Olah, G. A. *et al.* Selective Monohalogenation of Methane over Supported Acid or Platinum Metal Catalysts and Hydrolysis of Methyl Halides over γ-Alumina-Supported Metal Oxide/Hydroxide Catalysts. A Feasible Path for the Oxidative Conversion of Methane into Methyl Alcohol/Di. *J. Am. Chem. Soc.* **107**, 7097–7105 (1985).

44. Angeles, L., Bucsi, I. & Olah, G. A. Selective monochlorination of methane over solid acid and zeolite catalysts. *Catal. Letters* **16**, 27–38 (1992).

45. McNaught, A. & WIlkinson, A. STP. *IUPAC. Compendium of Chemical Terminology, 2nd ed. (the 'Gold Book')* doi:https://doi.org/10.1351/goldbook.S06036

46. Wilson, S. T., Lok, B. M., Messina, C. A., Cannan, T. R. & Flanigen, E. M. Aluminophosphate Molecular Sieves : A New Class of microporous crystalline inorganic solids . *J. Am. Chem. Soc.* **104**, 1146–1147 (1982).

47. Lok, B. M. *et al.* Silicoaluminophosphate Molecular Sieves: Another New Class of Microporous Crystalline Inorganic Solids. *J. Am. Chem. Soc.* **106**, 6092–6093 (1984).

48. Argauer, R. J. & Landolt, G. R. Crystalline Zeolite ZMS-5 and Method of Preparing the Same. US Patent 3,702,886 (1972).

Silver Nanocubes Coated in Ceria: Core/Shell Size Effects on Light-Induced Charge Transfer[h]

Plasmonic sensitization of semiconductors is an attractive approach to increase light-induced photocatalytic performance; one method is to use plasmonic nanostructures in core@shell geometry. The occurrence and mechanism of synergetic effects in photocatalysis of such geometries are under intense debate and proposed to occur either through light-induced charge transfer (CT) or through thermal effects. This study focuses on the relation between the dimensions of Ag@CeO_2 nanocubes, the wavelength-dependent efficiency, and the mechanism of light-induced direct CT. A 4mercaptobenzoic acid (4-MBA) linker between core and shell acts as a Raman probe for CT. For all Ag@CeO_2 nanocubes, CT increases with decreasing excitation wavelength, with notable increase at and below 514 nm. This is fully explainable by CT from silver to the 4-MBA LUMO, with the increase for excitation wavelengths that exceed the Ag/4-MBA LUMO gap of 2.28 eV (543 nm). A second general trend observed is an increase in CT yield with ceria shell thickness, which is assigned to relaxation of the excited electron further into the ceria conduction band, potentially producing defects.

[h] This work has been published as *O'Neill, D.B. et al*, ACS Appl. Mater. Interfaces 2020, 12, 1, 1905-1912

Silver Nanocubes Coated in Ceria: Core/Shell Size Effects on Light-Induced Charge Transfer

1 Introduction

Sensitized photocatalysts are gaining increasing attention with the growing concerns about the state of the environment and, with it, the desire to use more sustainable energy sources. Nanostructures that support local surface plasmon resonances (LSPR), which is the photoinduced collective oscillation of electrons, can be used to sensitize semiconductors through decoration, incorporation, or hierarchical construction such as core@shell particles.[1−3] Core@shell nanostructures are attractive because they offer controllable overlap of the enhanced electric field with the semiconductor and even the boundary of the semiconductor with the external media by controlling the thickness of the shell.

Plasmonic enhancement of photocatalysts can be divided into four mechanisms: plasmon-induced resonance energy transfer (PIRET),[4−6] direct charge transfer (CT) during photoexcitation or before plasmon dephasing, indirect CT after plasmon dephasing,[4,7−9] and as a local heat source.[10] PIRET requires coupling of transition dipoles and is strongly dependent on the distance and spectral overlap of the plasmonic donor and the energy acceptor but can occur through space.[4,5] Unlike PIRET, both CT mechanisms need electronic coupling. Direct CT can be divided into three categories based on wavelength dependence and association with plasmonic modes. (1) Plasmon-induced interfacial CT transition (PICTT): a new electronic transition that requires strong coupling between the donor and acceptor across the interface of the plasmonic particle and semiconductor. (2) Direct interfacial CT transition (DICTT): a CT transition not associated with a plasmonic mode, but instead with a weaker metal−adsorbate transition possible above a threshold photon energy.[8] (3) Chemical interface dampening (CID): a new adsorbate-induced plasmon dephasing pathway, with a quantum yield in agreement with the LSPR absorption.[8,11] For indirect CT there is a sensitivity to the photon energy as excited electrons must overcome the Schottky barrier prior to relaxation through heat generation in the lattice.[4,5,7−10]

As well as acting as a sensitizer,[2,3] the LSPR is also a sensor for the local environment: changes to the local refractive index (n) cause spectral shifts[12] and enhance Raman intensities.[13,14] The LSPR spectral properties depend on the particle material, shape, size, and local environment.[15,16] Silver nanocubes support several LSPR modes; the most relevant to this study is the dominant corner mode (red-most mode for an isolated cube). This mode projects the furthest from the surface and is most sensitive to the local refractive index for supported cubes.[12,15−17] The distance-

dependent refractive index sensitivity (RIS(t), with t being the distance), determined from finite-domain time-difference (FDTD) simulations, allows for determination of the shell coverage.

CeO_2 is a well-known catalyst with demonstrable potential as a photocatalyst,[18−22] which supports Ce(IV) and Ce(III) states forming reactive oxygen vacancies[23,24] and catalyzes reactions such as reducing CO_2 into CO.[25] CeO_2 has a bulk direct band gap of 3.6 eV and an indirect band gap of ∼2.4 eV;[26] in addition, trap states may induce light absorption throughout the visible regime. Silver nanoparticles are an attractive choice to sensitize ceria as they have high quality plasmonic modes,[27] a high refractive index sensitivity,[28] and, through geometric control, light absorption throughout the visible and near-infrared regime.[29] Additionally, use of a core@shell geometry is of interest, as the metal core can be isolated—either to prevent reactions, such as silver dissolving, or to promote selectivity by only having the semiconductor as an available active site. There have been studies on Ag/CeO_2 (nano)composites,[30−34] but only few studies report on core@shell geometries,[35−39] despite their promise as photocatalysts. Silver nanocubes are attractive because of the spatial localization of modes[17] and high $|E|^2$ enhancement,[40] while preserving a high degree of symmetry. Generalizable fundamental understanding of structural effects on the photophysics is important, specifically on the occurrence, mechanism, and wavelength dependence of photoinduced CT.

The aim of this work is to investigate photoinduced CT in Ag@CeO_2 core@shell nanocubes through surface-enhanced Raman scattering (SERS) spectroscopy by using the method developed by Lombardi and Birke.[41] Comparing the intensities of totally and non-totally symmetric Raman modes allows for a quantification of the relative enhancement from the LSPR and from CT.[41] We have investigated the role of core and shell dimensions on CT by using a 4-mercaptobenzoic acid (4-MBA) tag between the silver and ceria as the Raman probe. Here, the wavelength-dependent effects of core and shell dimensions on CT have been examined. FDTD simulations have been performed to model the shell coverage of the Ag@CeO_2 core@shell nanocubes and determine the distance dependences of the refractive index sensitivity. These give insights into the relationship between Ag@CeO_2 core@shell nanostructure design and light-induced CT processes.

2 Materials and methods

2.1 Synthesis Ag Nanocubes.

Ag nanocubes of varied sizes were synthesized by using a method adapted from the polyol synthesis;[42,43] the solvent for all solutions used in the synthesis was ethylene glycol. A round-bottom flask, containing 40 mL of ethylene glycol (Fluka, >99.9%) and 0.4 g of polyvinylpyrrolidone (PVP, Sigma-Aldrich), was heated at 150 °C for 2 h. 0.4 mL of 3 mM Na_2S was then added, followed by the dropwise addition of 2.5 mL of 280 mM $AgNO_3$(Alfa Aesar, 99+%). The reaction was followed with a spectrometer (Avantis Starline AvaSpec-2048) and quenched by cooling when the desired spectrum was observed. After quenching, the product was cleaned through centrifugation (9000g) and redispersion into ethanol through sonication five times. The final suspensions were 10 mL and had an attenuance of 4×10^2 at the spectral maximum.

2.2 Synthesis Ag@CeO_2 Core−Shell Nanocubes.

Silver nanocubes with edge lengths of 47 ± 7 and 71 ± 9 nm were coated with conformal ceria shells of different thicknesses by varying the cerium nitrate and sodium hydroxide concentrations. A mild synthesis method to deposit the ceria shell on the plasmonic cube was chosen, as high temperatures or caustic reagents can easily damage or destroy the particles.[44]

Ceria was deposited on silver in a method adapted from bulk precipitation methods.[45] $Ce(NO_3)_3{\cdot}6H_2O_{(aq)}$ (Sigma-Aldrich, 99% trace metal) was exposed to a molar equivalent of $NaOH_{(aq)}$ (SigmaAldrich, >98%) in the presence of 4-MBA-modified Ag nanocubes. Specifically, 1000 μL of the OD ~ 400 particle suspension was added to 20 mL of water, followed by 100 μL of 3 mM 4-$MBA_{(EtOH)}$, and the suspension was then incubated for 10 min. The amount of ceria precursor and base to particles was varied to achieve different ceria shell thicknesses, where 10, 100, or 5000 μmol of both $Ce(NO_3)_{3(aq)}$ and $NaOH_{(aq)}$ was used. Samples were cleaned through centrifugation (4000g) and dispersion into Uvasol ethanol (VWR) three times.

Initial studies did not include 4-MBA, and ceria grew off the PVP on the Ag nanocubes; however, to observe CT the 4-MBA was included. In mildly acidic conditions 4-MBA attaches to silver by the thiol group;[46] precipitating ceria then binds to the free carboxylic group (similarly, the ceria can grow off the oxygen in PVP[37]) and grows off the Ag nanocubes. This allows for the 4-MBA to act as a linker and be in electronic contact with both the silver and ceria.

2.3 FDTD Simulations.

The program Lumerical FDTD Solutions was used for simulations for theoretical support of the experimental spectral changes caused by the shell deposition. Ag nanocubes were modeled with rounded edges and corners (r = 2.5 nm); ceria shells were modeled with the same structure. As thickness was increased, the radii of edges and corners were increased, such that the particle was spherical when the thickness is equal to the core size. Scattering and absorption were both considered to produce a calculated extinction relatable to experimental results. While the Johnson and Christy[47] model for silver was used, noncomplex indices of refraction were used to model the shell and surrounding media. The refractive index value n for the ceria shell was set at 2.2, and a value of 1.337 for the solvent (water) was used. Using a fixed value for the shell facilitates generalization of the results for use with the Lorentz−Lorenz equation.

2.4 Nanostructure Characterization.

The UV−vis spectra of Ag@ CeO_2 core−shell nanostructures in suspension were collected by using a ThermoSci EVO600 spectrometer. For refractive index sensitivity measurements, the solvents used were deionized water, ethanol, and ethylene glycol. Characterization of the nanoparticles used a Philips CM300ST-FEG transmission electron microscope (TEM) with acceleration voltage of 300 kV and energy dispersive X-ray analysis (EDX). The dimensions of uncoated Ag nanocubes and Ag@CeO_2 core−shell nanocubes were determined from 20 measurements of shells/crystallites on the particles. Scanning electron micrographs (SEM) were recorded by using a JSM-6010LA SEM. X-ray diffraction (XRD) analysis was performed on a Bruker D2 (Cu Kα source) diffractometer, which revealed increased shielding of the silver core with increased shell thickness; the diffractogram is shown in Figure S1 of the appendix. X-ray photoelectron spectroscopy (XPS) was performed with a Quantera SXM, with an Al Kα source (1486.6 eV).

2.5 Raman Measurements.

Raman measurements were performed on a diluted suspension of Ag@CeO_2 core−shell nanocubes in Milli-Q water. Raman spectra at 785 nm excitation were collected with an Avantes AvaRaman probe system, containing 1% ethanol. For Raman measurements with 458, 488, 514, and 568 nm excitations, the excitation source was an Ar/Kr ion laser (Coherent). A single grating monochromator (Jobin Yvon, focal length 640 mm) with a liquid N_2 cooled CCD camera (Princeton Instruments) was used for detection. Calibration of the Raman shift for these excitation energies was performed using cyclohexane as a reference. The Raman

spectra were invariant with respect to the excitation intensity between 2.5 and 10 mW (Figure S2).

3 Results and discussion

3.1 Nanostructural and Optical Characterization.

Figure 1 shows the TEM micrographs of the uncoated Ag nanocubes (i) and the Ag@CeO_2 core@shell nanocubes with different ceria shells (ii–iv), for cubes with an edge length of 47 ± 7 nm (A) and 71 ± 9 nm (B). For amounts of ceria insufficient to coat the Ag nanocubes fully, we observe an incomplete coverage with small CeO_2 crystallites (ii); otherwise, conformal CeO_2 shells with tunable thickness are formed (iii and iv). See Table S1 for specific values for each sample and Figure S3 for additional TEM and SEM micrographs showing no larger structures. There is no significant difference in the size of the isolated ceria crystallites between the 47 and 71 nm Ag nanocubes coated with ceria, with 2.6 ± 0.3 and 2.3 ± 0.2 nm sized crystallites, respectively. Aggregated crystallites form the thicker ceria shells, resulting in a relatively conformal coating of the Ag nanocubes. The TEM micrographs show that the ceria shells are porous, that is, have voids. This is most likely due to the absence of a chelating agent which would slow down the deposition of ceria.[38] XPS reveals a Ce^{3+}/Ce^{4+} ratio of 0.09 (see Figure S4 and Table S2). The

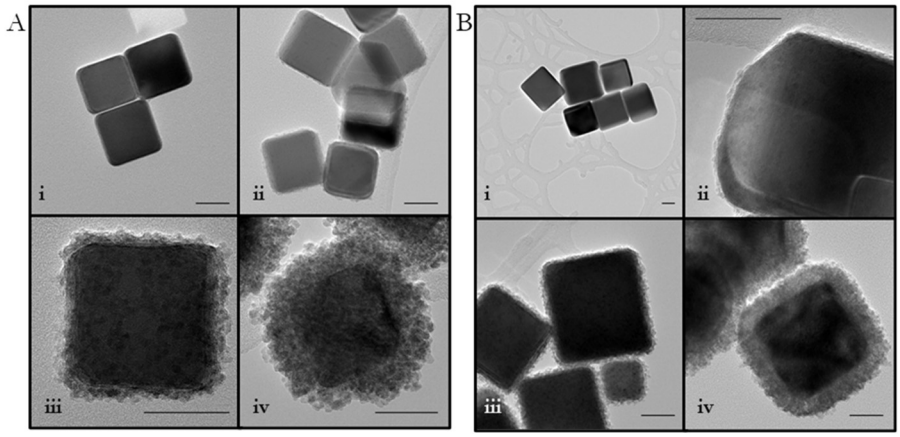

Figure 1: TEM of A) 47±7 nm silver cubes with i) no shell, ii) incomplete coverage with 2.6±0.3 nm CeO_2 crystallites, iii) a 4.6±1.3 nm shell, and iv) 14.1±3.9 nm shell; and B) 71±9 nm cubes with i) no shell, ii) incomplete coverage with 2.3±0.2 nm crystallites, iii) a 3.7±1.1 nm ceria shell, and iv) a 17.6±3.5 nm conformal shell. The scale bars in all micrographs are 30 nm. Core and shell dimensions have all been determined from no less than 20 measurements.

coverage has been determined from the simulated and experimental extinction properties in different solvents (see below). A summary of shell thicknesses and coverages is provided in Table S1.

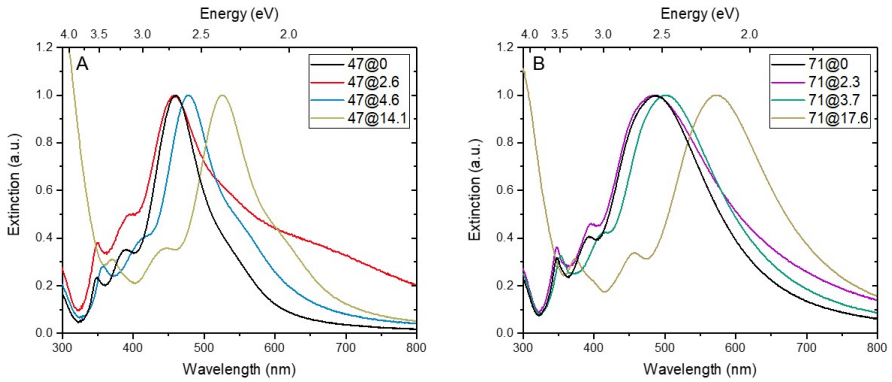

Figure 2: UV-Vis spectra of A) 47 nm and B) 71 nm silver nanocubes, PVP capped, and coated with ceria and treated with 4-MBA, in ethanol. Red-shifting of modes occurs due to the increased local index of refraction caused by the presence of CeO_2.

Figure 2 presents the UV−vis spectra of the uncoated and coated 47 nm (A) and 71 nm (B) Ag nanocubes. The silver interband transition around 300 nm red-shifts with CeO_2 shell thickness; this is likely due to interband scattering,[48] and, in particular, for the thickest shells, possibly from the CeO_2 bandgap (3.6 eV, 344 nm).[49,50] The red-shift of all the spectral features with increased CeO_2 shell thickness is due to an increase in local index of refraction, as the plasmonic modes are highly sensitive to the local environment.[15] CeO_2 has a refractive index between 2.2 and 2.8 in the visible regime,[49,50] significantly higher than the refractive index of water. The mode centered at 348 nm observed for uncoated 47 and 71 nm Ag cubes is localized on the face of the cube[17] and is highly sensitive to the sharpness of the corners.[51] The retention of this mode during coating suggests that no significant etching of the corners occurs. The mode at 390 nm (47 nm cubes) and 405 nm (71 nm cubes) is localized on the edges, while the intense, lowest energy mode at 460 nm (47 nm cubes) and 485 nm (71 nm cubes) is localized at the corners of the cube.[17] The latter mode is strongly dependent on the cube edge length and is the most sensitive to a change in local index of refraction.[16,17] The broad band around 700 nm for the 47 nm silver nanocubes with a 2.6 nm shell, and to a low extent those around 750 nm for the 71 nm silver nanocubes with a 2.3 nm shell, is most likely due to mild

aggregation. It is worth noting that no new electronic transitions indicative of direct CT is observed.

The ceria shell coverage, while accounting for the voids in the shell, has been determined by correlating experimental and simulated changes in the UV−vis spectrum induced by a change in the local refractive index by using (i) different solvents (Figure S5) and (ii) changing the ceria shell thickness. The volume fraction of the shell (ϕ_i) depends on the shell coverage (η) and the distance-dependent refractive index sensitivity (RIS(t), with t the distance) according to:

$$\varphi_i = \frac{\int_o^t \eta RIS(t)dt}{\int_o^\infty RIS(t)dt} = \eta\big(1 - \mathrm{RIS(t)}\big) \qquad [1]$$

due to the $|E|^2$ profile around the plasmonic nanostructure.[15] The value of ϕ_i has been determined by using the Lorentz− Lorenz equation:[52]

$$\frac{n_{eff}^2-1}{n_{eff}^2+2} = \sum \varphi_i \frac{n_i^2-1}{n_i^2+2} \qquad [2]$$

$n_{\mathrm{eff}} + 2\, n_i + 2$ (2) where n_{eff} is the effective refractive index, a function of the ith component's refractive index n_i and ϕ_i the volume fraction. There are only two components considered for this system: the shell and solvent as the PVP/4-MBA capping agent is a constant and needed to prevent aggregation. The effective refractive index of the Ag cubes has been determined from RIS(t) by dispersing

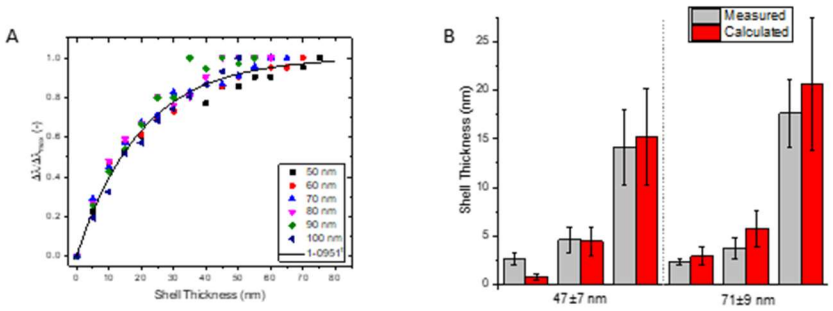

Figure 3: A) Simulated peak shift of the corner mode with respect to n for cubes of 50 to 100 nm, normalized from a pure solvent to a pure shell system, including a fit to RIS(t) = (0.951±0.009)^t, with t the shell thickness. B) Comparison of the shell thickness determined by TEM and UV-Vis using the results from FDTD and the average coverage, giving statistically similar results.

uncoated Ag cubes in solvents of different refractive indexes and determining the peak shift of the corner mode relative to n (see Figure S5).

Figure 3A shows the effect of ceria shell thickness on the peak shift of the corner mode, simulated by FDTD for cubes with an edge length ranging from 50 to 100 nm: for an edge length ≤90 nm, RIS(t) = $(0.951 \pm 0.009)^t$ (see fit included in Figure 3A and Figure S6). This model of RIS(t) has been validated by comparing all shell thicknesses as determined by TEM with simulated values (Figure 3B). Applying eq 1 yields an average shell coverage $\eta = 0.67 \pm 0.25$ (specific values for all samples are shown in Table S1), allowing quantification of the shell thickness through UV−vis spectra alone in future synthesis of$Ag@CeO_2$ nanocubes.

3.2 Photoinduced Charge Transfer.

The 4-MBA linker has been used as a SERS probe for photoinduced CT and facilitates examination of the role of photoexcitation wavelength and core@shell dimensions. The degree of CT (ρ_{CT}) has been determined using the theory developed by Lombardi and Birke. Equation 3 compares the selective enhancement of the nontotally symmetric vibrational modes, which are enhanced by CT, relative to totally symmetric modes which are only enhanced by the LSPR. A value of 0.5 implies equal Raman enhancement from LSPR and CT:[41]

$$\rho_{CT}(k) = \frac{I^k(CT) - I^k(LSPR)}{I^k(CT) + I^0(LSPR)} \qquad [3]$$

The parameter k is an index identifying individual molecular bands in the Raman spectrum. I^k(LSPR) is the intensity of line (k) where only the LSPR contributes to the SERS enhancement, while I^0(LSPR) denotes the intensity of a chosen totally symmetric line, also with only LSPR contribution. I^k(CT) is the intensity of a non-totally symmetric mode where both LSPR and CT contribute. For a non-totally symmetric line I^k(LSPR) will normally be small or zero, reducing eq 3 into

$$\rho_{CT}(k) = \frac{\frac{I^k(CT)}{I^0(LSPR)}}{1 + \frac{I^k(CT)}{I^0(LSPR)}} \qquad [4]$$

This method is only capable of observing direct CT that involves the 4-MBA linker. It is not possible to observe any CT directly from silver to ceria bypassing the 4-MBA. Additionally, there is no information regarding the directionality of the process. However, given the lack of light absorption by the ceria or 4MBA and the strong absorption by the silver, it can be concluded that CT originating from light absorbed by the silver is the most likely mechanism.

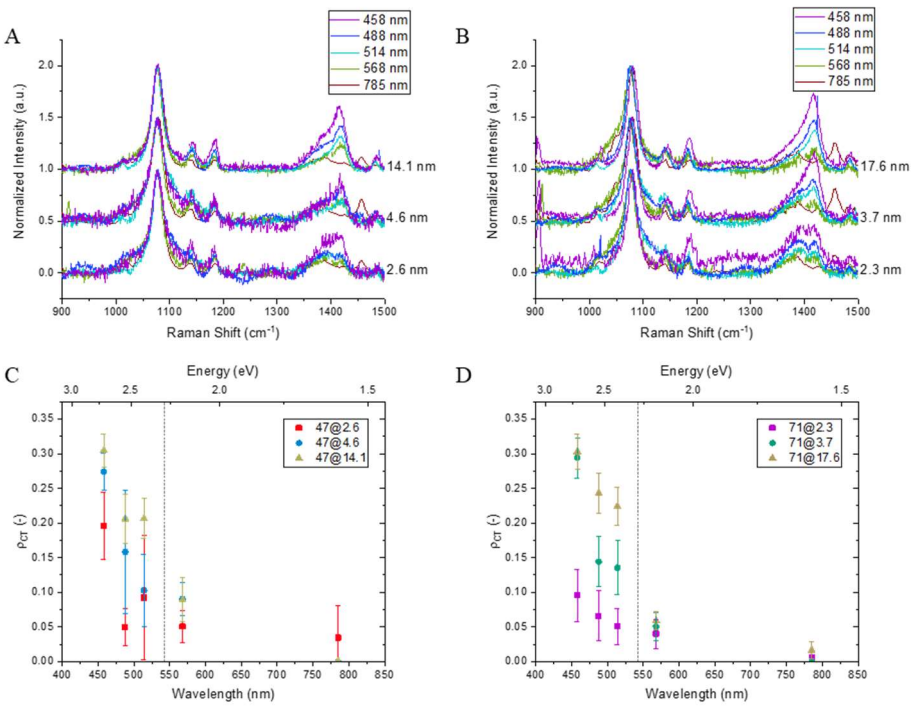

Figure 4: Raman spectra of 4-MBA between silver and ceria for A) 47 nm and B) 71 nm silver nanocubes, normalized to the intensity of the 1070 cm^{-1} mode. The degree of charge transfer, ρ_{CT}, at different excitation energies for C) 47 nm and D) 71 nm Ag@CeO_2 nanocubes with different shell thicknesses, the dashed vertical line is at 543 nm, the wavelength of light needed to excite an electron from the silver Fermi level to the 4-MBA LUMO. The ρ_{CT} was calculated using the variance of the 1415 cm^{-1} mode as compared to the 1070 cm^{-1} mode.

Figure 4 shows the Raman spectra at various excitation wavelengths for the 47 nm (A) and 71 nm (B) Ag nanocubes with 4-MBA linker and different ceria shell thicknesses. The Raman spectra are invariant to the laser intensity between 2.5 and 10 mW (see Figure S2). The mode at 1070 cm^{-1} used for normalization of the Raman spectra is the C−S stretch and a symmetric ring breathing mode (νCS and 1)[53−55] and has A_1 character. The assignment of the 1140 and 1180 cm^{-1} modes is in debate; however, not the modes at 1370 and 1415 cm^{-1} which are of B_2 character.[54−58] Specifically, the 1415 cm^{-1} mode is the asymmetric ring mode 18b, and the 1370 cm^{-1} is assigned to βO−H, νC−ph, 19a, and asymmetric νCO_2 vibrations.[53−55] Table 1 summarizes the assignments of the modes. On the basis of these assignments, we have used the 1415 cm^{-1} mode as I^k(CT) and the 1070 cm^{-1} mode as I^0(LSPR) to

Wavenumber (cm^{-1})	Band Assignment*	Symmetry	Ref
1070	νCS and 1	A1	56,58,64
1140	9a+ γ OH	A1	56
	δCH+ν15	B2	58,64
1180	βOH+9a	B2	56
	δ CH+9a	A1	57
	νCH	A1	57, 59
1370	βOH+νC–ph+19a & $\nu_{as}CO_2$	B2	56
1415	18b	B2	56, 59
	βOH+νC–ph+19a & $\nu_{as}CO_2$	B2	57
	νCOO^-		59,63
1600	9a	A1	56
	νCC	A1	57, 59, 63

Table 1: Raman mode and symmetry assignments from literature for 4-MBA.

*ν symmetric stretching, ν_{as} asymmetric stretching ,β bending, δ deformation.

resolve ρ_{CT}. For quantification of ρ_{CT}, the spectra have been fit with Gaussian functions (see the appendix for details).

An important parameter to address is the 4-MBA layer thickness. In the ideal case a monolayer is present, with the 4MBA molecule likely attached to the Ag core via the thiol group and to the ceria shell via the carboxylic acid group,46 implying a subnanometer 4-MBA layer thickness. Multilayer structures may be formed through hydrogen bonding between the thiol and the carboxylic acid groups and by van der Waals interactions. However, such a multilayer structure would show a βOH Raman mode which would vary between an incomplete shell to the complete shell; that is, variation of the 1180 cm^{-1} mode and the 1370 cm^{-1} mode.[46] As such effect is absent in the Raman spectra (Figure 4A,B), it can be concluded that a multilayer of 4-MBA

is unlikely, which is further supported by the TEM experiments (Figure 1) unable to resolve the 4-MBA linker. Incomplete coverage of the Ag surface can however not be excluded, although no PVP Raman signals have been observed.

Figure 4C shows ρ_{CT} as a function of excitation wavelength for the 47 nm Ag nanocubes with three different ceria shell thicknesses. The measurements at 785 nm excitation have 1% ethanol, which gives rise to the extraneous peak at 1460 cm^{-1}. For both nanocube edge lengths, the most pronounced effect on the intensities of the 1370 and 1415 cm^{-1} modes is observed at 488 and 458 nm excitation. At 785 nm excitation ρ_{CT} is close to zero for all three ceria shell thicknesses, as can be expected for photon energies significantly lower than both the LSPR and a potential Ag to 4-MBA electronic transition. The ρ_{CT} value significantly increases on decreasing the excitation wavelength, with a notable increase at 514 nm and shorter wavelengths. In addition, ρ_{CT} is higher for thicker ceria shells. Figure 4D, presenting ρ_{CT} values for the 71 nm Ag nanocubes coated with different ceria shell thicknesses, shows similar trends. The absence of a band at 1415 cm^{-1} for Ag cubes coated with 4-MBA only (Figure S7) demonstrates that the ceria shell is crucial for the CT process.

Figure 5 shows an energy level diagram[24,59] and the proposed CT mechanism. If the CT were to occur through PICTT, CID, or indirect CT, then it would be expected that ρ_{CT} would follow the LSPR absorption of the silver core.[60] Given that no LSPR dependency is observed here, CT is most likely dominated by the DICTT mechanism. The increase in ρ_{CT} at 514 nm and shorter wavelengths can be assigned to CT of an electron from the Ag core to the LUMO of the 4-MBA, which is allowed for photon energies >2.28 eV (i.e., <543 nm) through the DICTT mechanism. The increase with photon energy likely originates from the increasing probability for CT from an electron at a greater depth in the Fermi sea; on average, half the photon energy is left in the hole formed on photoexcitation.[6] Indeed, at 785 nm excitation CT is insignificant for all core@shell geometries. However, all ρ_{CT} values at 568 nm excitation exceed those at 785 nm, indicating some CT, although inefficient. The photon energy at 568 nm light (2.18 eV) is 0.1 eV below the energy gap between the Ag Fermi level and the LUMO of the 4MBA linker.[59] Within the thermal distribution of electrons at room temperature, there is a 2% chance of the state 0.1 eV above the silver Fermi level being populated (Figure S8), which likely accounts for the low ρ_{CT}. Additionally, CT from the 4-MBA HOMO to the silver may occur. While this may have some contribution to ρ_{CT}, it is not expected to demonstrate the trends seen here, as it would lead to relatively constant ρ_{CT} values for wavelengths shorter than 543 nm, which is not observed.

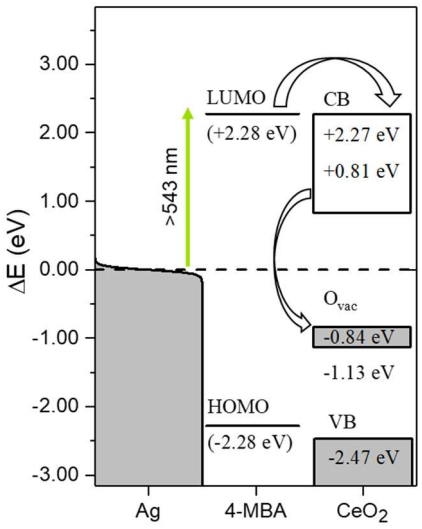

Figure 5: Energy diagram and proposed mechanisms of light-induced CT, the black dashed line is the Fermi energy of silver used as a reference.[60,65] Photoexcitation could promote an electron from the Ag core to the 4-MBA linker, followed by electron transfer from the 4-MBA to the CeO_2. The latter process may result in the formation of an oxygen vacancy (O_{vac}).

Aside from this excitation wavelength effect on ρ_{CT}, a second general trend observed is a higher ρ_{CT} value with increasing ceria layer thickness. This dependency indicates that not only the 4MBA intermediate layer affects the CT process but also the ceria outer shell. There are statistically significant increases in ρ_{CT} with a thicker shell through the 4-MBA pathway (Figure 4C,D), which indicate that the electron excited from the Ag core to the 4-MBA can relax into the CeO_2 conduction band (CB). Similar observations were made for a Au/4-MBA/TiO_2 system, where the metal to 4-MBA CT occurs, and then the electron is transferred to the semiconductor.[60] The ρ_{CT} value for, in particular, the thinnest shells may be limited by charge buildup, which impedes further CT.[61] This effect likely decreases with increasing shell thickness, explaining the higher ρ_{CT} observed.

Interestingly, a dependency on the core size is not observed here. In other works,[11,60] there has been a significant increase in ρ_{CT} values for excitation wavelengths that were in resonance. Here we observed a ρ_{CT} dependency purely determined by incident photon energy, apparently independent of the LSPR position, indicating a difference in mechanism (DICTT here, CID in ref 7, and PIRET in ref 8). Additionally, no significant shift of the Raman peaks that could be induced by a strong electric field[62,63] is observed for the two core sizes studied here.

Only a slight shift is seen in the 1070 cm^{-1} mode for Ag cubes without a ceria shell (Figure S7), indicative of a difference in hydrogen bonding.[64] This Ag@CeO_2 system merits further studies through photocatalytic activity testing and ultrafast spectroscopy to investigate photoinduced formation of oxygen vacancies.

4 Conclusions

This study focuses on the relation between the dimensions of Ag@CeO_2 nanocubes and the efficiency and mechanism of light-induced CT. A 4-MBA linker between core and shell has been used as a probe for light-induced direct CT by Raman spectroscopy. The ceria shell coverage has been determined with FDTD simulations, which describe the distance-dependent refractive index sensitivity, and UV−vis spectroscopy.

The degree of photoinduced CT has been determined by comparing the intensities of totally symmetric and non-totally symmetric modes. For all Ag@CeO_2 nanocubes investigated, the degree of CT increases with decreasing excitation wavelength, with a pronounced increase around 514 nm. This trend is fully explicable through a direct CT mechanism from the silver Fermi level to the 4-MBA LUMO. Interestingly, there was no trend seen relating to the core size or to the extinction of the silver nanocube core.

A second general trend observed is a higher CT yield with increasing ceria shell thickness, indicating further electron transfer from the 4-MBA to the ceria shell. It may be that electron transfer from 4-MBA to CeO_2 becomes more likely with increasing shell thickness. As this process could lead to formation of oxygen vacancies, this shows promise for photocatalytic application. These results provide deeper understanding of light-induced charge transfer in plasmonic@ semiconductor nanocubes.

5 References

1. Kubacka, A.; Fernandez-García, M.; Colón, G. Advanced Nanoarchitectures for Solar Photocatalytic Applications. Chem. Rev. 2012, 112 (3), 1555−1614.
2. Gust, D.; Moore, T. A.; Moore, A. L. Solar Fuels via Artificial Photosynthesis. Acc. Chem. Res. 2009, 42 (12), 1890−1898.
3. Linic, S.; Christopher, P.; Ingram, D. B. Plasmonic-Metal Nanostructures for Efficient Conversion of Solar to Chemical Energy. Nat. Mater. 2011, 10 (12), 911−921.
4. Cushing, S. K.; Li, J.; Bright, J.; Yost, B. T.; Zheng, P.; Bristow, A. D.; Wu, N. Controlling Plasmon-Induced Resonance Energy Transfer and Hot Electron

Injection Processes in Metal@TiO2 Core−Shell Nanoparticles. J. Phys. Chem. C 2015, 119 (28), 16239−16244.

5. Li, J.; Cushing, S. K.; Meng, F.; Senty, T. R.; Bristow, A. D.; Wu, N. Plasmon-Induced Resonance Energy Transfer for Solar Energy Conversion. Nat. Photonics 2015, 9 (9), 601−607.

6. Gieseking, R. L.; Ratner, M. A.; Schatz, G. C. Review of PlasmonInduced Hot-Electron Dynamics and Related SERS Chemical Effects. ACS Symp. Ser. 2016, 1245, 1−22.

7. Kale, M. J.; Christopher, P. Plasmons at the Interface. Science 2015, 349 (6248), 587−588.

8. Wu, K.; Chen, J.; McBride, J. R.; Lian, T. Efficient Hot-Electron Transfer by a Plasmon-Induced Interfacial Charge-Transfer Transition. Science 2015, 349 (6248), 632−635.

9. Boerigter, C.; Aslam, U.; Linic, S. Mechanism of Charge Transfer from Plasmonic Nanostructures to Chemically Attached Materials. ACS Nano 2016, 10 (6), 6108−6115.

10. Baffou, G.; Quidant, R. Thermo-Plasmonics: Using Metallic Nanostructures as Nano-Sources of Heat. Laser Photon. Rev. 2013, 7 (2), 171−187.

11. Kale, M. J.; Avanesian, T.; Xin, H.; Yan, J.; Christopher, P. Controlling Catalytic Selectivity on Metal Nanoparticles by Direct Photoexcitation of Adsorbate−Metal Bonds. Nano Lett. 2014, 14 (9), 5405−5412.

12. Ahamad, N.; Bottomley, A.; Ianoul, A. Optimizing Refractive Index Sensitivity of Supported Silver Nanocube Monolayers. J. Phys. Chem. C 2012, 116 (1), 185−192.

13. Wu, X.; Xia, Y.; Huang, Y.; Li, J.; Ruan, H.; Chen, T.; Luo, L.; Shen, Z.; Wu, A. Improved SERS-Active Nanoparticles with Various Shapes for CTC Detection without Enrichment Process with Supersensitivity and High Specificity. ACS Appl. Mater. Interfaces 2016, 8 (31), 19928−19938.

14. Dutta, S.; Ray, C.; Sarkar, S.; Pradhan, M.; Negishi, Y.; Pal, T. Silver Nanoparticle Decorated Reduced Graphene Oxide (RGO) Nanosheet: A Platform for SERS Based Low-Level Detection of Uranyl Ion. ACS Appl. Mater. Interfaces 2013, 5 (17), 8724−8732.

15. Willets, K. A.; Van Duyne, R. P. Localized Surface Plasmon Resonance Spectroscopy and Sensing. Annu. Rev. Phys. Chem. 2007, 58 (1), 267−297.

16. Sherry, L. J.; Chang, S.-H.; Schatz, G. C.; Van Duyne, R. P.; Wiley, B. J.; Xia, Y. Localized Surface Plasmon Resonance Spectroscopy of Single Silver Nanocubes. Nano Lett. 2005, 5 (10), 2034−2038.

17. Nicoletti, O.; de la Peña, F.; Leary, R. K.; Holland, D. J.; Ducati, C.; Midgley, P. A. Three-Dimensional Imaging of Localized Surface Plasmon Resonances of Metal Nanoparticles. Nature 2013, 502 (7469), 80−84.

18. Shelef, M.; McCabe, R. W. Twenty-Five Years after Introduction of Automotive Catalysts: What Next? Catal. Today 2000, 62 (1), 35− 50.

19. Montini, T.; Melchionna, M.; Monai, M.; Fornasiero, P. Fundamentals and Catalytic Applications of CeO_2-Based Materials. Chem. Rev. 2016, 116 (10), 5987−6041.

20. Kaspar, J.; Fornasiero, P.; Hickey, N. Automotive Catalytic̆ Converters: Current Status and Some Perspectives. Catal. Today 2003, 77 (4), 419−449.

21. Liu, Z. E.; Wang, J.; Li, Y.; Hu, X.; Yin, J.; Peng, Y.; Li, Z.; Li, Y.; Li, B.; Yuan, Q. Near-Infrared Light Manipulated Chemoselective Reductions Enabled by an Upconversional Supersandwich Nanostructure. ACS Appl. Mater. Interfaces 2015, 7 (34), 19416−19423.

22. Jia, H.; Zhu, X. M.; Jiang, R.; Wang, J. Aerosol-Sprayed Gold/ Ceria Photocatalyst with Superior Plasmonic Hot Electron-Enabled Visible-Light Activity. ACS Appl. Mater. Interfaces 2017, 9 (3), 2560− 2571.

23. Zhang, Y. C.; Li, Z.; Zhang, L.; Pan, L.; Zhang, X.; Wang, L.; Fazal-e-Aleem; Zou, J. J. Role of Oxygen Vacancies in Photocatalytic Water Oxidation on Ceria Oxide: Experiment and DFT Studies. Appl. Catal., B 2018, 224, 101−108.

24. Ma, R.; Jahurul Islam, M.; Amaranatha Reddy, D.; Kim, T. K. Transformation of CeO_2 into a Mixed Phase CeO_2/Ce_2O_3 Nanohybrid by Liquid Phase Pulsed Laser Ablation for Enhanced Photocatalytic Activity through Z-Scheme Pattern. Ceram. Int. 2016, 42 (16), 18495− 18502.

25. Goguet, A.; Meunier, F. C.; Tibiletti, D.; Breen, J. P.; Burch, R. Spectrokinetic Investigation of Reverse Water-Gas-Shift Reaction Intermediates over a Pt/CeO2 catalyst. J. Phys. Chem. B 2004, 108 (52), 20240−20246.

26. Inerbaev, T. M.; Karakoti, A. S.; Kuchibhatla, S. V. N. T. N. T.; Kumar, A.; Masunov, A. E.; Seal, S. Aqueous Medium Induced Optical Transitions in Cerium Oxide Nanoparticles. Phys. Chem. Chem. Phys. 2015, 17 (9), 6217−6221.

27. Wang, F.; Shen, Y. R. General Properties of Local Plasmons in Metal Nanostructures. Phys. Rev. Lett. 2006, 97 (20), 1−4.

28. Singh Sekhon, J.; Verma, S. S. Refractive Index Sensitivity Analysis of Ag, Au, and Cu Nanoparticles. Plasmonics 2011, 6 (2), 311− 317.

29. Cobley, C. M.; Skrabalak, S. E.; Campbell, D. J.; Xia, Y. ShapeControlled Synthesis of Silver Nanoparticles for Plasmonic and Sensing Applications. Plasmonics 2009, 4 (2), 171−179.

30. Chen, M.; Gu, J.; Sun, C.; Zhao, Y.; Zhang, R.; You, X.; Liu, Q.; Zhang, W.; Su, Y.; Su, H. Light-Driven Overall Water Splitting Enabled by a Photo-Dember Effect Realized on 3D Plasmonic Structures. ACS Nano 2016, 10 (7), 6693−6701.

31. Yu, L.; Peng, R.; Chen, L.; Fu, M.; Wu, J.; Ye, D. Ag Supported on CeO_2 with Different Morphologies for the Catalytic Oxidation of HCHO. Chem. Eng. J. 2018, 334, 2480−2487.

32. Raudonyte-Svirbutaviciene, E.; Neagu, A.; Vickackaite, V.; Jasulaitiene, V.; Zarkov, A.; Tai, C. W.; Katelnikovas, A. Two-Step Photochemical Inorganic Approach to the Synthesis of Ag-CeO_2 nanoheterostructures and Their Photocatalytic Activity on Tributyltin Degradation. J. Photochem. Photobiol., A 2018, 351, 29−41.

33. Grabchenko, M. V.; Mikheeva, N. N.; Mamontov, G. V.; Salaev, M. A.; Liotta, L. F.; Vodyankina, O. V. Ag/CeO_2 Composites for Catalytic Abatement of CO, Soot and VOCs. Catalysts 2018, 8 (7), 285.

34. Chang, S.; Li, M.; Hua, Q.; Zhang, L.; Ma, Y.; Ye, B.; Huang, W. Shape-Dependent Interplay between Oxygen Vacancies and $AgCeO_2$ interaction in Ag/CeO_2 catalysts and Their Influence on the Catalytic Activity. J. Catal. 2012, 293, 195−204.

35. Wang, Y.-Y.; Shu, Y.; Xu, J.; Pang, H. Facile One-Step Synthesis of Ag@CeO_2 Core−Shell Nanospheres with Efficient Catalytic Activity for the Reduction of 4-Nitrophenol. CrystEngComm 2017, 19 (4), 684− 689.

36. Chen, S.-Y.; Tseng, E.; Lai, Y.-T.; Lee, W.; Gloter, A. Interface Interactions and Enhanced Room Temperature Ferromagnetism of Ag@CeO2 Nanostructures. Nanoscale 2017, 9 (30), 10764−10772.

37. Wu, L.; Fang, S.; Ge, L.; Han, C.; Qiu, P.; Xin, Y. Facile Synthesis of Ag@CeO_2 Core−Shell Plasmonic Photocatalysts with Enhanced Visible-Light Photocatalytic Performance. J. Hazard. Mater. 2015, 300 (18), 93−103.

38. Wang, J. J.; Li, B.; Gu, T.; Ming, T.; Wang, J. J.; Wang, P.; Yu, J. C. (Gold Core) at (Ceria Shell) Nanostructures for Plasmon-Enhanced Catalytic Reactions under Visible Light. ACS Nano 2014, 8 (8), 8152− 8162.

39. Pelli Cresi, J. S.; Spadaro, M. C.; D'Addato, S.; Valeri, S.; Benedetti, S.; di Bona, A.; Catone, D.; Di Mario, L.; O'Keeffe, P.; Paladini, A.; et al. Highly Efficient Plasmon-Mediated Electron Injection into Cerium Oxide from Embedded Silver Nanoparticles. Nanoscale 2019, 11 (21), 10282−10291.

40. Yang, Y.; Matsubara, S.; Xiong, L.; Hayakawa, T.; Nogami, M. Solvothermal Synthesis of Multiple Shapes of Silver Nanoparticles and Their SERS Properties. J. Phys. Chem. C 2007, 111 (26), 9095−9104.

41. Lombardi, J. R.; Birke, R. L. A Unified Approach to SurfaceEnhanced Raman Spectroscopy. J. Phys. Chem. C 2008, 112 (14), 5605−5617.

42. Skrabalak, S. E.; Au, L.; Li, X.; Xia, Y. Facile Synthesis of Ag Nanocubes and Au Nanocages. Nat. Protoc. 2007, 2 (9), 2182−2190.

43. Bottomley, A.; Prezgot, D.; Ianoul, A. Plasmonic Properties of Silver Nanocube Monolayers on High Refractive Index Substrates. Appl. Phys. A: Mater. Sci. Process. 2012, 109, 869−872.

44. Garnett, E. C.; Cai, W.; Cha, J. J.; Mahmood, F.; Connor, S. T.; Greyson Christoforo, M.; Cui, Y.; McGehee, M. D.; Brongersma, M. L. Self-Limited Plasmonic Welding of Silver Nanowire Junctions. Nat. Mater. 2012, 11 (3), 241−249.

45. Tseng, C. H. T.; Paul, B. K.; Chang, C.-H.; Engelhard, M. H. Continuous Precipitation of Ceria Nanoparticles from a Continuous Flow Micromixer. Int. J. Adv. Manuf. Technol. 2013, 64 (1−4), 579− 586.

46. Ho, C. H.; Lee, S. SERS and DFT Investigation of the Adsorption Behavior of 4-Mercaptobenzoic Acid on Silver Colloids. Colloids Surf., A 2015, 474, 29−35.

47. Johnson, P. B.; Christy, R. W. Optical Constants of the Noble Metals. Phys. Rev. B 1972, 6 (12), 4370−4379.

48. See, K. C.; Spicer, J. B.; Brupbacher, J.; Zhang, D.; Vargo, T. G. Modeling Interband Transitions in Silver Nanoparticle-Fluoropolymer Composites. J. Phys. Chem. B 2005, 109 (7), 2693−2698.

49. Bruno, G.; Gasparotto, A.; Tondello, E.; Barreca, D.; Losurdo, M. Nanostructure and Optical Properties of CeO_2 Thin Films Obtained by Plasma-Enhanced Chemical Vapor Deposition. Mater. Sci. Eng., C 2003, 23 (6−8), 1013−1016.

50. Oh, T. S.; Tokpanov, Y. S.; Hao, Y.; Jung, W.; Haile, S. M. Determination of Optical and Microstructural Parameters of Ceria Films. J. Appl. Phys. 2012, 112 (10), 103535.

51. Grillet, N.; Manchon, D.; Bertorelle, F.; Bonnet, C.; Broyer, M.; Cottancin, E.; Lerme, J.; Hillenkamp, M.; Pellarin, M. Plasmoń Coupling in Silver Nanocube Dimers: Resonance Splitting Induced by Edge Rounding. ACS Nano 2011, 5 (12), 9450−9462.

52. Aspnes, D. E. Local field Effects and Effective medium Theory: A Microscopic Perspective. Am. J. Phys. 1982, 50 (8), 704−709.

53. Preuss, M.; Bechstedt, F. Vibrational Spectra of Ammonia, Benzene, and Benzene Adsorbed on Si (001) by First Principles Calculations with Periodic Boundary Conditions. Phys. Rev. B: Condens. Matter Mater. Phys. 2006, 73 (15), 155413.

54. Andrejeva, A.; Gardner, A. M.; Tuttle, W. D.; Wright, T. G. Consistent Assignment of the Vibrations of Symmetric and Asymmetric Para -Disubstituted Benzene Molecules. J. Mol. Spectrosc. 2016, 321 (4), 28−49.

55. Li, R.; Lv, H.; Zhang, X.; Liu, P.; Chen, L.; Cheng, J.; Zhao, B. Vibrational Spectroscopy and Density Functional Theory Study of 4-Mercaptobenzoic Acid. Spectrochim. Acta, Part A 2015, 148, 369−374.

56. Xue, X.; Ji, W.; Mao, Z.; Mao, H.; Wang, Y.; Wang, X.; Ruan, W.; Zhao, B.; Lombardi, J. R. Raman Investigation of Nanosized TiO_2: Effect of Crystallite Size and Quantum Confinement. J. Phys. Chem. C 2012, 116 (15), 8792−8797.

57. Guo, L.; Zhang, X.; Li, P.; Han, R.; Liu, Y.; Han, X.; Zhao, B. Surface-Enhanced Raman Scattering (SERS) as a Probe for Detection of Charge-Transfer between TiO_2 and CdS Nanoparticles. New J. Chem. 2019, 43 (1), 230−237.

58. Chen, L.; Sun, H.; Zhao, Y.; Zhang, Y.; Wang, Y.; Liu, Y.; Zhang, X.; Jiang, Y.; Hua, Z.; Yang, J. Plasmonic-Induced SERS Enhancement of Shell-Dependent Ag@Cu_2O Core-Shell Nanoparticles. RSC Adv. 2017, 7 (27), 16553−16560.

59. Zhang, X.; Yu, Z.; Ji, W.; Sui, H.; Cong, Q.; Wang, X.; Zhao, B. Charge-Transfer Effect on Surface-Enhanced Raman Scattering (SERS) in an Ordered Ag NPs/4-Mercaptobenzoic Acid/TiO_2 System. J. Phys. Chem. C 2015, 119 (39), 22439−22444.

60. Han, R.; Song, W.; Wang, X.; Mao, Z.; Han, X. X.; Zhao, B. Investigation of Charge Transfer at the TiO_2-MBA-Au Interface Based on Surface-Enhanced Raman Scattering: SPR Contribution. Phys. Chem. Chem. Phys. 2018, 20 (8), 5666−5673.

61. Sheldon, M.; van de Groep, J.; Brown, A.; Polman, A.; Atwater, H. Plasmoelectric Potentials in Metal. Science 2014, 346 (6211), 828− 831.

62. Banik, M.; El-Khoury, P. Z.; Nag, A.; Rodriguez-Perez, A.; Guarrottxena, N.; Bazan, G. C.; Apkarian, V. A. Surface-Enhanced Raman Trajectories on a Nano-Dumbbell: Transition from Field to Charge Transfer Plasmons as the Spheres Fuse. ACS Nano 2012, 6 (11), 10343−10354.

63. Nie, S.; Emory, S. R. Probing Single Molecules and Single Nanoparticles by Surface-Enhanced Raman Scattering. Science 1997, 275 (5303), 1102−1106.

64. Wang, Y.; Ji, W.; Sui, H.; Kitahama, Y.; Ruan, W.; Ozaki, Y.; Zhao,B. Exploring the Effect of Intermolecular H-Bonding: A Study on Charge-Transfer Contribution to Surface-Enhanced Raman Scattering of p-Mercaptobenzoic Acid. J. Phys. Chem. C 2014, 118 (19), 10191− 10197.

65. Chen, L.; Sun, H.; Zhao, Y.; Zhang, Y.; Wang, Y.; Liu, Y.; Zhang, X.; Jiang, Y.; Hua, Z.; Yang, J. Plasmonic-Induced SERS Enhancement of Shell-Dependent Ag@Cu2O Core-Shell Nanoparticles. RSC Adv. 2017, 7 (27), 16553−16560.

66. Esch, F.; Africh, C.; Comelli, G.; Fabris, S.; Fornasiero, P.; Montini, T.; Rosei, R.; Zhou, L. Electron Localization Determines Defect Formation on Ceria Substrates. Science 2005, 309 (5735), 752− 755.

Appendix A: Supporting Information for Chapter 3

Supplementary figures and tables

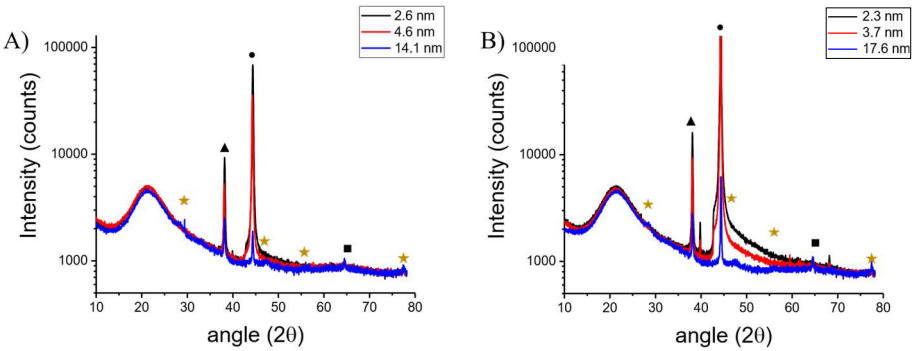

Figure S1: X-ray diffraction pattern of A) 47±7 nm and B) 71±9 nm silver nanocubes, coated with ceria shells with thicknesses indicated in the legend. While ceria is generally not resolved, a shielding of the silver core with thicker ceria shells is observed. The peaks are shifted due to height, as the samples were deposited on quartz slides, which elevated the sample by 1 mm. The silver peaks are ascribed to (111) at 38° (▲), (220) at 47° (●), and (220) at 64° (□). Silver nanocubes are known to be single crystal,[1] as twinning would lead to different morphologies, this is supported by the sharpness of the silver peaks and the presence of monochromator artifacts. The lack of peaks from ceria is consistent with literature data for uncalcined ceria[2,3] and likely due to the very small particle size, causing extreme peak broadening. An argument could be made that weak ceria peaks are visible for the thickest ceria shells: (111) at 28°, (220) at 47°, (311) at 56° and (331) at 77° (yellow stars).

Table S1: Overview of the $Ag@CeO_2$ shell thickness/coverage for each different core and shell sizes, obtained from TEM measurements (N>20). The coverage was determined by relating the LSPR shift to the distance dependent refractive index sensitivity (see main text).

47±7 nm	71±9 nm
2.6±0.3 nm / 20%	2.3±0.2 nm / 82%
4.6±1.3 nm / 63%	3.7±1.1 nm / 95%
14.1±3.9 nm / 69%	17.6±3.5 nm / 33%

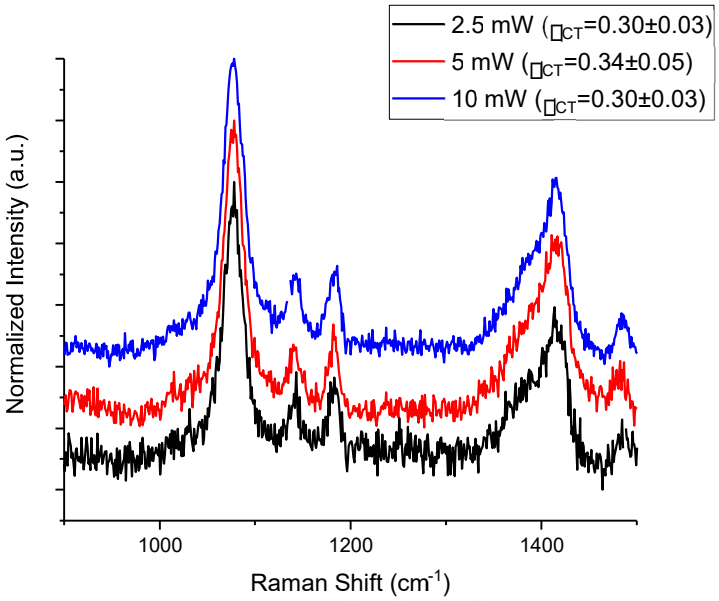

Figure S2: Raman measurements taken for 47±7 nm cubes with a 14.1±3.9 nm shell at 488 nm excitation at different incident intensities, showing invariance with incident intensity after normalization to the amplitude of the 1070 cm^{-1} mode

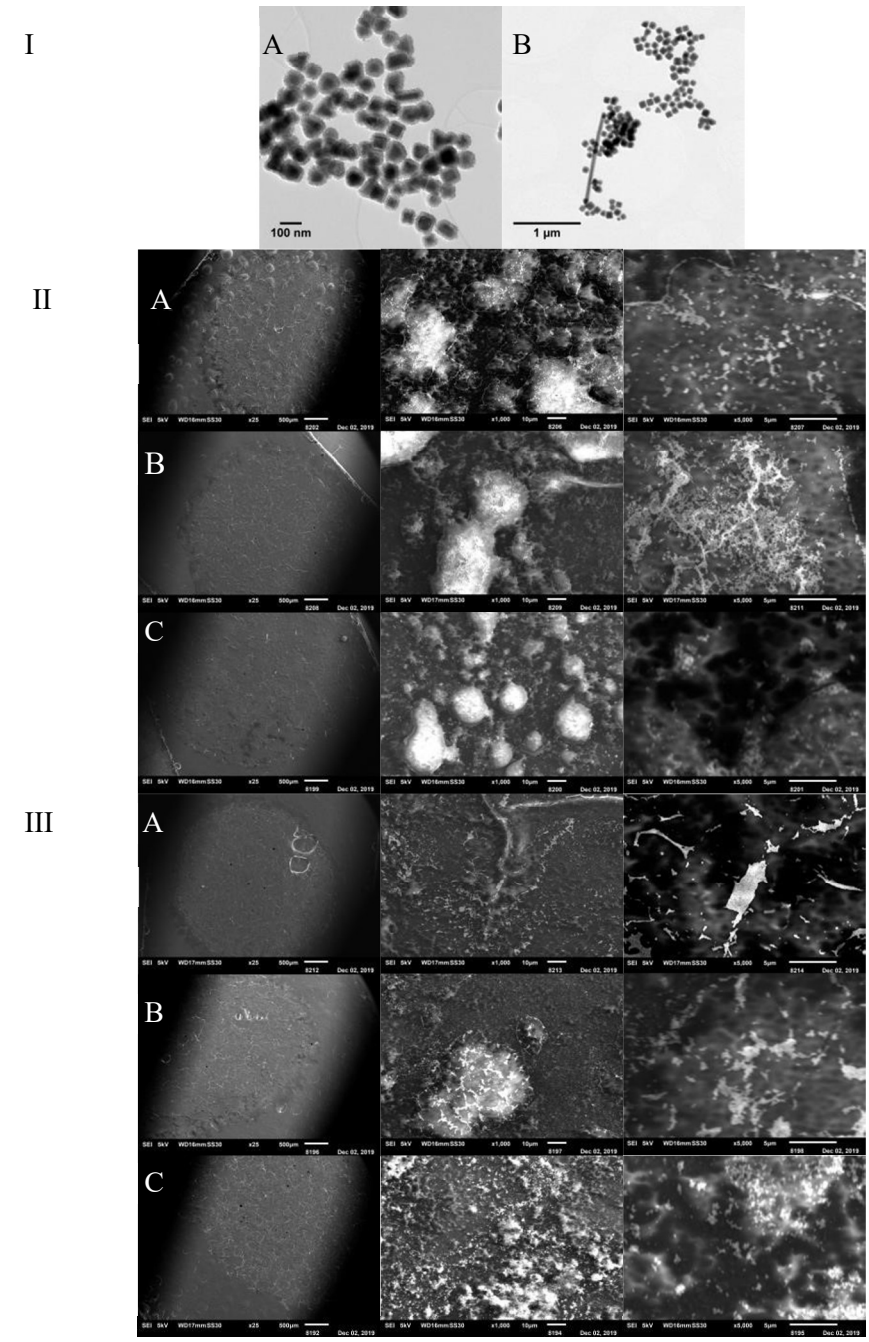

. Figure S3: I) TEM images of A) 47 nm Ag cubes with 14.1 nm ceria shell and B) 71 nm Ag cubes with 17.6 nm ceria shell. While there is some geometric distribution in the samples, even with the thickest shells there are no large, or loose

ceria particles. II) SEM images of 47 nm Ag cubes with A) 2.6 nm crystallites, B) 4.6 nm shell, and C) 14.1 nm shell. III) SEM images of 71 nm cubes with A) 2.3 nm crystallites, B) 3.7 nm shell, and C) 17.6 nm shell; it is clear that there are no particles so large that they would not be seen in the TEM, and no large isolated particles are seen in the TEM.

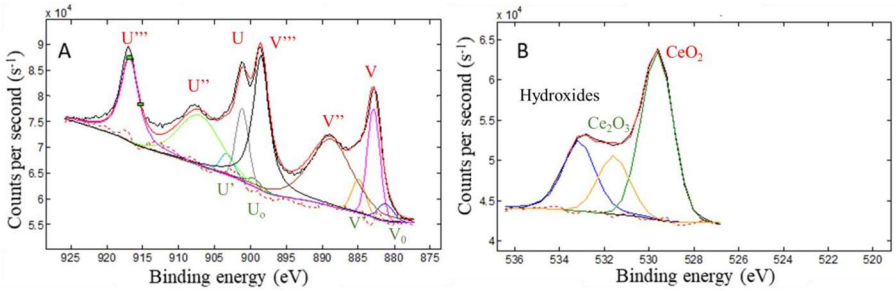

Figure S4: XPS for 71 nm Ag nanocubes with 17.6 nm ceria shells. A) Ce 3d peaks, fit with 5 doublets, of which 3 are assigned to Ce^{4+} (red) and 2 to Ce^{3+} (green).[4–7] The area of the peaks was used to determine the relative abundance of the Ce^{3+} to the Ce^{4+} oxidation state (Table S2) by comparing the relative intensity of the areas($[Ce^{3+}] = \frac{area_{Ce^{3+}}}{area_{Ce^{3+}} + area_{Ce^{4+}}}$. B) O 1s peaks which show the presence of oxygen vacancies (Ce_2O_3, Ce^{3+}) and hydroxides.[4,5]

Table S2: Results of Ce 3d peak fitting.

Band	Position (eV)	FWHM (eV)	Height (s^{-1})	Area (eV s^{-1})	Area (%)	Assignment
1	881.19	2.46	3440	9001	1.82	Ce^{3+} (V_0)
2	882.85	2.10	21255	47442	9.60	Ce^{4+} (V)
3	884.93	2.25	6553	15911	3.22	Ce^{3+} (V')
4	888.76	6.93	13073	117218	23.71	Ce^{4+} (V")
5	898.52	2.66	26344	106426	21.53	Ce^{4+} (V"")
6	899.49	2.46	1614	6030	1.22	Ce^{3+} (U_0)
7	901.15	2.10	14241	31786	6.43	Ce^{4+} (U)
8	903.23	2.25	4225	10660	2.16	Ce^{3+} (U')
9	907.06	6.93	9874	78536	15.89	Ce^{4+} (U")
10	916.82	2.99	16426	71306	14.43	Ce^{4+} (U"")

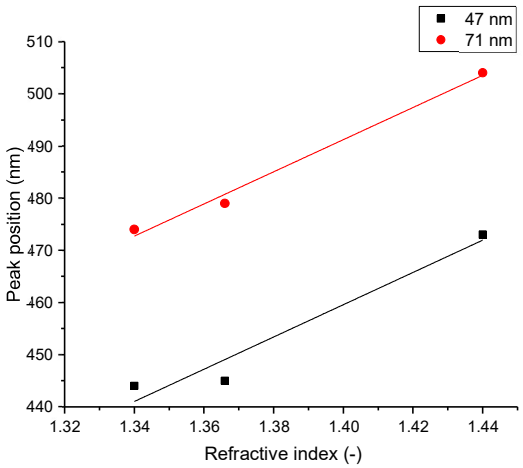

Figure S5: Refractive index sensitivity of the Ag cubes' dominant corner mode determined by dispersing the cubes in water,[8] ethanol,[9] and ethylene glycol[10] was found to be 310±70 nm/RIU and 310±30 nm/RIU for 47±7 nm and 71±9 nm cubes.

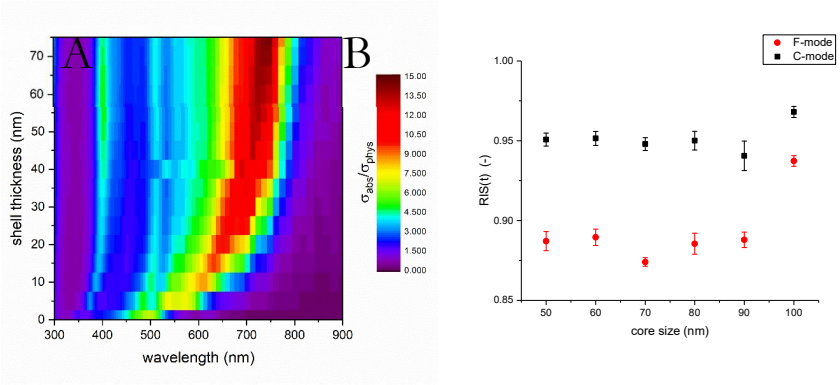

Figure S6: FDTD results: A) simulated absorption spectra for a 50 nm Agnanocube in water with a shell of various thicknesses (nshell=2.2) used to determine RIS(t). B)RIS(t) forthe dominant corner mode (C-mode) and highest energy facial mode (F-mode)for different core sizes.

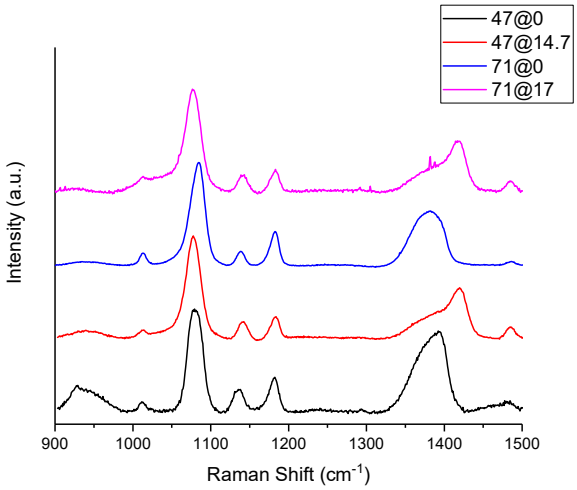

Figure S7: Raman spectra at 488 nm excitation of 47 and 71 nanometer cubes functionalized with 4-MBA, with and without ceria shell; and of CeO_2 nanoparticles in water at 785 nm excitation. The ceria Raman intensity is normalized to the F_{2g} mode at 412 cm^{-1}.[11] The 1415 cm^{-1} peak indicative of charge transfer is not present in the absence of the ceria shell. The slight shift in the 1070 cm^{-1} mode and intensity of the 1370 cm^{-1} mode for Ag cubes coated with 4-MBA only are both explicable by different H-bonding relative to the ceria coated analogues.[12] For assignment of the Raman peaks, see main text.

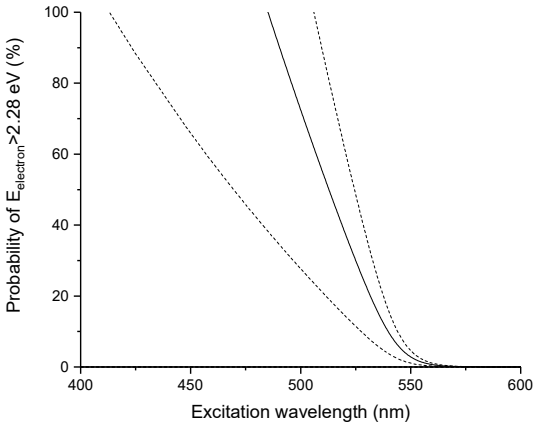

Figure S8: Probability (and uncertainty thereof, dashed lines) that an electron excited by the dephasing of the plasmon has sufficient energy to enter the 4-MBA LUMO (2.28 eV above the Ag Fermi level), calculated by comparing the area of

the Fermi distribution for silver that would allow the transition to all allowed transitions. Generally, this supports the excitation wavelength dependency seen in the ρ_{CT} values.

Raman Spectrum Processing

While analyzing the data, it was found that the result of ρ_{CT} could vary non-trivially depending on how the Raman spectra were baselined. To account for this, a robust baselining method for is needed for quantitative analysis. Common approaches include use of derivatives, filters, or manual polynomial fitting.[13] The latter most approach was used to achieve this: a MATLAB script was made to algorithmically baseline the data through the ***msbackadj*** function, which estimates the baseline through a spline approximation of multiply shifted windows. To prevent calculating ρ_{CT} for an incorrect baseline, the algorithm uses a loop for ***msbackadj*** step sizes of 2 to 250 data points, and then calculates the ρ_{CT} for each baseline. Initialization of the script first allows for the calibration of the detector (convert pixel to wavenumber) using cyclohexane. All Raman data sets except for 785 nm excitation require this step.

The second step of the script is to import the remaining spectra of the set and then to begin treating the data. The script allowed for the removal of artifacts through the "zap" function, which removed the offending data point from the set of Raman spectra (in the processing, one set was all the spectra from a single excitation energy and measured on the same day). To calculate ρ_{CT} the user is prompted to select a window in which the 1070 cm^{-1} reference peak is, and then the window where the varying 1400 cm^{-1} peak is. The 1070 cm^{-1} peak is fit with a single Gaussian; while the reference peak was fit with two Gaussian peaks, as there is are two asymmetric modes present. This gives the area of the peaks from which ρ_{CT} is calculated.

The choice of Gaussian, and not a mixed, or convoluted system was reached as the convoluted system requires knowledge, or manual parameterization of the ratio of Gaussian and Lorentzian peaks (which introduce bias), and the mixed system is a further fitting parameter which had neutral benefit. The mixed Gaussian-Lorentzian peak more correctly models the SERS peak, however the persistent error induced by the use of Gaussian fitting was countered by the systematic deconvolution of the doublet peak. That is, use of a mixed peak fitting would have necessitated either a reduction in the baseline accuracy, or an introduction of a user parameter and therefore a bias. Summarily the Gaussian fit was used, and the error induced by this fit is minimized by averaging over many baselines.

It was observed that the average of the set is approximately the same as the calculated ρ_{CT} for very small step sizes. The method produces few outliers which varied considerably from the rest of the set of ρ_{CT} found for a single Raman spectrum; the most extreme are cut from the data in a consistent manner: exclusion of ρ_{CT} which are 3 times greater than the ρ_{CT} for small step sizes (ρ_{CT}=0.2 was set if no ρ_{CT} was calculatable). The calculated ρ_{CT} for a spectrum is then averaged for all nonexcluded baselines, with the standard deviation as the error.

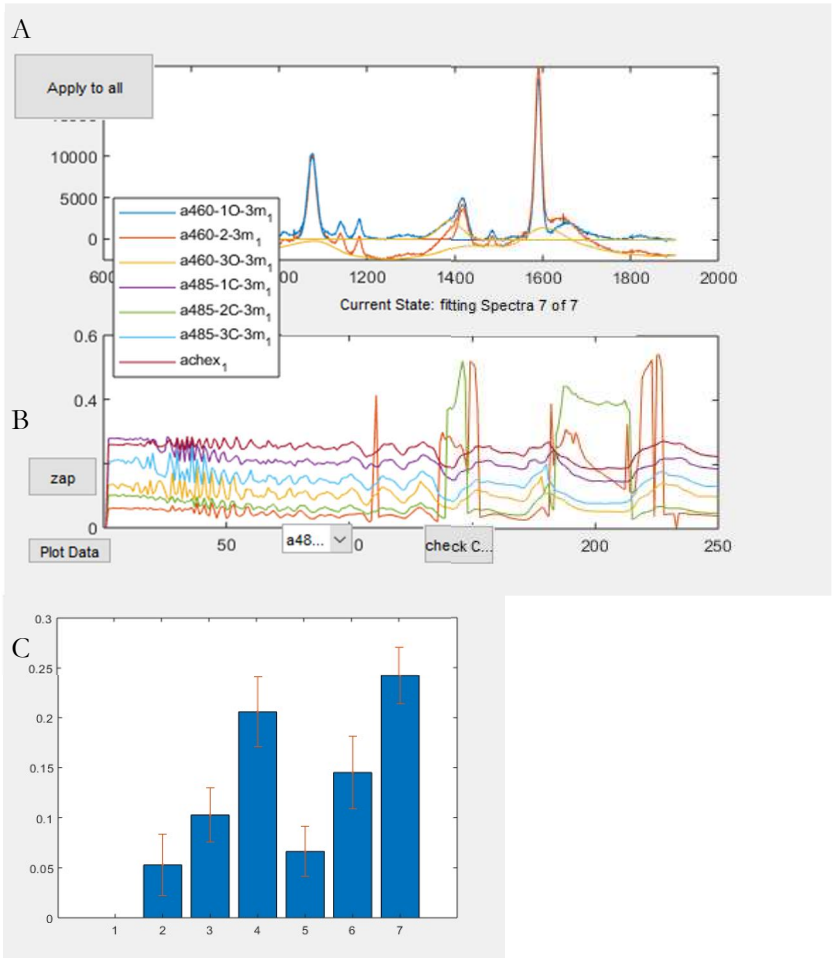

Figure S7: A) The data from 488 nm excitation being treated. The upper plot shows the raw data (subtracting the average of the initial points), and the baseline corrected data for a step size of 100. B) The lower pane shows the calculated ϱ_{CT} for the set of data, and the legend overlaying both panes pertains to the lower. C) An average ϱ_{CT}, and standard deviation are determined from the output in B.

References

1. Xia, Y.; Xiong, Y.; Lim, B.; Skrabalak, S. E. Shape-Controlled Synthesis of Metal Nanocrystals: Simple Chemistry Meets Complex Physics? *Angew. Chem. Int. Ed.* **2009**, *48* (1), 60–103.
2. Saitzek, S.; Blach, J.-F.; Villain, S.; Gavarri, J.-R. Nanostructured Ceria: A Comparative Study from X-Ray Diffraction, Raman Spectroscopy and BET Specific Surface Measurements. *Phys. Status Solidi* **2008**, *205* (7), 1534–1539.

3. Sahoo, S. K.; Mohapatra, M.; Singh, A. K.; Anand, S. Hydrothermal Synthesis of Single Crystalline Nano CeO_2 and Its Structural, Optical, and Electronic Characterization. *Mater. Manuf. Process.* **2010**, *25* (9), 982–989.
4. Ma, R.; Jahurul Islam, M.; Amaranatha Reddy, D.; Kim, T. K. Transformation of CeO2 into a Mixed Phase CeO_2/Ce_2O_3 Nanohybrid by Liquid Phase Pulsed Laser Ablation for Enhanced Photocatalytic Activity through Z-Scheme Pattern. *Ceram. Int.* **2016**, *42* (16), 18495–18502. https://doi.org/10.1016/j.ceramint.2016.08.186.
5. Świątowska, J.; Lair, V.; Pereira-Nabais, C.; Cote, G.; Marcus, P.; Chagnes, A. XPS, XRD and SEM Characterization of a Thin Ceria Layer Deposited onto Graphite Electrode for Application in Lithium-Ion Batteries. *Appl. Surf. Sci.* **2011**, *257* (21), 9110–9119.
6. Świątowska, J. *et al,* XPS, XRD and SEM characterization of a thin ceria layer deposited onto graphite electrode for application in lithium-ion batteries*, App. Surf. Sci.,* **2011**, 257(21) 9110-9119
7. Paparazzo, E. On the Curve-Fitting of XPS Ce(3d) Spectra of Cerium Oxides. *Mater. Res. Bull.* **2011**, *46* (2), 323–326.
8. Burroughs, P.; Hamnett, A.; Orchard, A. F.; Thornton, G. Satellite Structure in the X-Ray Photoelectron Spectra of Some Binary and Mixed Oxides of Lanthanum and Cerium. *J. Chem. Soc. Dalt. Trans.* **1976**, No. 17, 1686-1698. https://doi.org/10.1039/dt9760001686.
9. Kedenburg, S.; Vieweg, M.; Gissibl, T.; Giessen, H. Linear Refractive Index and
10. Absorption Measurements of Nonlinear Optical Liquids in the Visible and Near-Infrared Spectral Region. *Opt. Mater. Express* **2012**, *2* (11), 1588-1611. https://doi.org/10.1364/ome.2.001588.
11. Sani, E.; Dell'Oro, A. Spectral Optical Constants of Ethanol and Isopropanol from Ultraviolet to Far Infrared. *Opt. Mater. (Amst).* **2016**, *60*, 137–141. https://doi.org/10.1016/j.optmat.2016.06.041.
12. Sani, E.; Dell'Oro, A. Optical Constants of Ethylene Glycol over an Extremely Wide Spectral Range. *Opt. Mater. (Amst).* **2014**, *37*, 36–41. https://doi.org/10.1016/j.optmat.2014.04.035.
13. Filtschew, A.; Hofmann, K.; Hess, C. Ceria and Its Defect Structure: New Insights from a Combined Spectroscopic Approach. *J. Phys. Chem. C* **2016**, *120* (12), 6694–6703. https://doi.org/10.1021/acs.jpcc.6b00959.
14. Wang, Y.; Ji, W.; Sui, H.; Kitahama, Y.; Ruan, W.; Ozaki, Y.; Zhao, B. Exploring the Effect of Intermolecular H-Bonding: A Study on Charge-Transfer Contribution to SurfaceEnhanced Raman Scattering of p-Mercaptobenzoic Acid. *J. Phys. Chem. C* **2014**, *118* (19), 10191–10197. https://doi.org/10.1021/jp5025284.
15. Sun, K.; Su, H.; Yao, Z.; Huang, P. Baseline Correction for Raman Spectra Based on Piecewise Linear Fitting. *Spectroscopy* **2014**, *29* (2), 54–61.

Influencing Energy and Charge Transfer Between Plasmonic Nanoparticles and Semiconductors: $Au/Ce_{1-x}Pr_xO_2$[i]

The sensitization of semiconductors by plasmonic nanoparticles has great potential for a myriad of applications. There are several mechanisms by which the sensitization can occur. Indeed plasmon-induced resonant energy transfer (PIRET), chemical interface dampening (CID), and ballistic charge transfer (BCT) have all been identified as means of transferring energy or charge. In this study, a gold nanoparticle/cerium-praseodymium oxide system was analyzed by means of femtosecond transient absorption spectroscopy. Interestingly, the concentration of praseodymium influences the photophysical mechanisms involved: without praseodymium BCT occurs, for moderate praseodymium loadings ($3\%_{Pr}$ and $5\%_{Pr}$) CID appears to be dominant, and with $10\%_{Pr}$ PIRET appears to become significant. That the mechanism of plasmonic sensitization of ceria is dependent on the praseodymium loading, despite minimal change to the steady state spectra and oxidation state (measured by *ex-situ* XPS), is of importance for the optimization of gold nanoparticle/cerium-praseodymium oxide for applications in photocatalysis and has implications for other plasmon-sensitized semiconductor systems.

[i] This work was done in collaboration with Kaijian Zhu of the PCS group at the University of Twente. K. Zhu was instrumental in measuring the TA spectra of the samples.

Influencing Energy and Charge Transfer Between Plasmonic Nanoparticles and Semiconductors: $Au/Ce_{1-x}Pr_xO_2$

1 Introduction

Plasmonic nanomaterials have garnered interest in recent years as a means of facilitating photocatalysis and photovoltaics[1–3], either directly[4,5] or through semiconductor sensitization.[6–9] While noble metals are expensive, the amount needed to capture a significant fraction of incident light is low, as the absorption cross section of such nanomaterials far exceeds the physical cross section.[10,11] This is due to the localized surface plasmon resonance (LSPR), where photoexcitation results in the collective oscillation of electrons in the material.[10]

The LSPR can decay non-radiatively:[12] in the absence of charge or resonant energy transfer, the non-radiative decay of the LSPR will generate excited non-equilibrium hot electrons (which could have ballistic transport properties)[13] through Landau dampening with, on average, an equal distribution of energy above and below the Fermi level.[13–15] Following this, there is electron-electron (e-e) scattering where the hot carriers' energy is transferred to the other charge carriers in the particle, generating a thermalized new Fermi distribution, usually occurring over about one half of a picosecond.[12] These thermalized carriers then couple to the lattice through electron-phonon (e-ph) coupling over several picoseconds, which heats the particle lattice. Ultimately, heat can be dissipated to the environment, which typically takes place on a time scale of tens to hundreds of ps.[12,16]

Additional competitive non-radiative relaxation pathways can exist through energy or charge transfer. Coupling of the transition dipoles of the particle and a semiconductor can result in plasmon-induced resonant energy transfer (PIRET) where the dephasing of the semiconductor-coupled LSPR results in promotion of an electron from the valence band to the conduction band of the semiconductor; this can occur through space but requires spectral overlap between the LSPR and the semiconductor.[17] The LSPR can also decay into an interfacial charge-transfer state via chemical interface damping (CID, also sometimes called plasmon induced charge transfer transition or PICTT[18,19]), which results in LSPR linewidth broadening and a decrease in attenuation, with some indication of a new mode being formed in the steady state attenuation spectra.[5,18–21] Additionally, charge transfer can occur if there are accepting electronic energy levels available in the semiconductor: ballistic charge transfer (BCT) of hot carriers and thermalized charge transfer (TCT), depending on when in time following photoexcitation the charge transfer

occurs.[12,13,18,22] The direct metal to semiconductor charge transfer transition may also occur, but when reported it is substantially weaker than either bulk metal transitions or plasmonic transitions.[23–26] In considering the different mechanisms of energy and charge transfer, there are two main features which can be used to identify them: when they occur, and what features they impart on the system.

Firstly, the time scales over which the mechanisms transfer the energy or charge varies. PIRET[17] and CID[5] both are competitive with the dephasing of the LSPR through Landau damping, and both shorten the LSPR lifetime.[12,17] Any signal from these should develop within a few femtoseconds after photoexcitation. In contrast, BCT occurs after Landau damping but before e-e scattering, and so is expected to occur over the first tens of femtoseconds; after which there have been several e-e

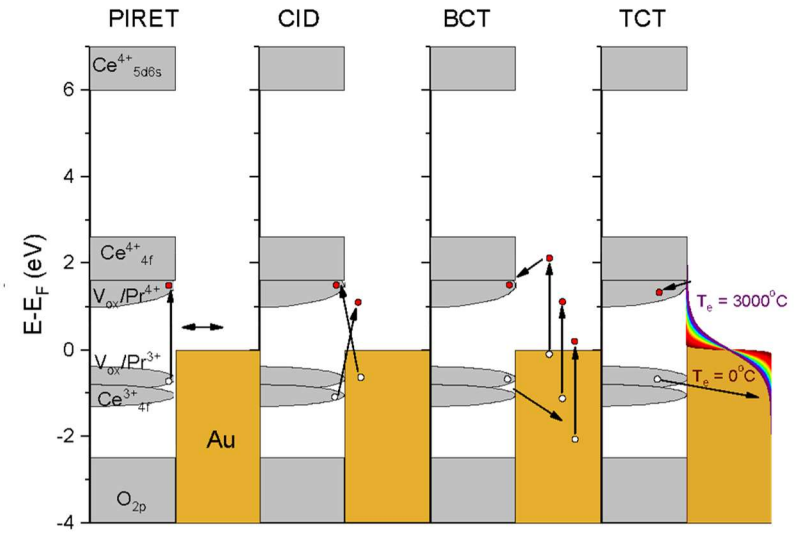

Figure 1: Schematic representation of the different mechanisms of energy and charge transfer, in the context of the gold/cerium-praseodymium oxide system studied here, unfilled circles represent holes and filled circles represent electrons. PIRET promotes an electron from the $Ce^{3+}{}_{4f}$ (or associated oxygen vacancy or $Pr^{3+}{}_{4f}$) to the $Ce^{4+}{}_{4f}$ (or associated oxygen vacancy or $Pr^{4+}{}_{4f}$) band. CID can result in the population of the $Ce^{4+}{}_{4f}$ band or can depopulate the $Ce^{3+}{}_{4f}$ band (both are shown, although only one would occur for a single photoexcitation event). BCT shows the range that a 2 eV photon could excite electrons or holes in gold (from or to the edge of the Fermi sea), which could allow for BCT to occur. Finally, the TCT mechanism shows that only the hottest electrons, those nearing 3000°C, have sufficient energy to undergo TCT.

scattering events lowering the energy of an individual non-equilibrium electron.[13,27] Finally, TCT occurs after e-e scattering, and so should occur after an initial delay of ~0.5 ps.[12,28] The different mechanisms are shown schematically in Figure 1.

Secondly, the features and requirements of each mechanism vary considerably as well. PIRET needs spectral overlap between energy donor and acceptor[17] and can occur through space, although the rate largely decreases with distance, while the other processes need electronic interaction between charge donor and acceptor.[18,29–31] PIRET will excite an electron in the acceptor which will depopulate the ground state electronic level and form a photobleach.[17] If CID occurs, then either an electron or a hole will be transferred to the semiconductor, and there should be a corresponding change in the particle electron density.[5,19] For both PIRET and CID, there is reduced generation of hot carriers in the metal, and the consequent generation of heat. With BCT, much like CID, there would be either an electron or hole transferred across the interface between particle and semiconductor, and the associated change in electron density would be observable - although this occurs after the generation of non-equilibrium carriers in the metal. Consequently, distinguishing between CID and BCT can be done through observation of the generation of either non-equilibrium electrons in the plasmonic particle (allowing BCT) or LSPR broadening and a decrease in attenuation due to a decrease in LSPR lifetime (CID). Additionally, as a non-equilibrium carrier is removed, the generation of heat in the plasmonic particle would be diminished for both BCT and CID. In TCT there may still be considerable heat generation, but also potentially more considerable change in electron density in the plasmonic particle owing to the greater number of electrons which share the energy of the initial excitation.[32,33]

Control of the competition between these processes is essential for application in photocatalysis, since PIRET yields an electron-hole pair in the semiconductor, allowing localized surface oxidation and reduction reactions, while charge transfer results in charge separation between the plasmonic particle and semiconductor. Heat generation is influenced as well. In this work, the energy and charge transfer dynamics between gold nanoparticles (AuNP) and ceria-praseodymium oxide (CPO) are examined to control the degree of energy and charge transfer following excitation of the gold nanoparticles' LSPR. The variation of the concentration of Pr (from $0\%_{Pr}$ to $10\%_{Pr}$ in CPO influences the system by increasing the spectral overlap between CPO and the AuNP, while minimizing the changes to the electronic energy levels in the oxide layer. Ceria easily forms oxygen vacancies (V_{ox}), in part due to the low energy needed to reduce or oxidize it.[34] This combination of Ce(III) and Ce(IV) with associated V_{ox} results in numerous electron and hole traps depending on the non-stoichiometry of a CeO_{2-x} sample; however, as it is relative easy to reduce or oxidize

ceria, this may not present the most stable system. It has been shown that the addition of praseodymium into ceria can promote V_{ox},[35,36] and that the energy levels it introduces in CPO are at comparable energies to the V_{ox}.[32,33,37–41] Additionally, much like increasing V_{ox} in CeO_2,[42] the introduction of praseodymium in CeO_2 promotes visible light attenuation,[43–45] thereby enhancing spectral overlap with the Au particles. It should be noted that the presence of praseodymium does influence both the ionic and electronic conductivity of the CPO.[46,47] A diagram of the energy levels is shown in concert with the mechanism described above in Figure 1. An extended discussion is included in the supporting information, a table of the expected evidence for each mechanism is shown in Table S1.

The steady state spectra show a broadening and lessening of the AuNP attenuation with increased [Pr], which indicate greater damping of the Au nanoparticles' LSPR with [Pr][5,18–21]; which is attributed to PIRET and CID. Transient absorption spectroscopy presented in this study, indicates BCT for samples without praseodymium, CID in samples with $3\%_{Pr\ n/n}$ and $5\%_{Pr\ n/n}$, while PIRET likely occurs with $10\%_{Pr\ n/n}$, showing that Pr loading steers the competition between energy and charge transfer between AuNP and CPO.

2 Results and Discussion

2.1 Nanostructure characterization

Quartz substrates were decorated with Au nanoparticles and calcined before CPO films were deposited; these particles have a surface population of 200.6 particles/μm^2 and a bimodal size distribution, 75 ± 6% being 40 ±20 nm in size, and the remainder being 25 ± 5 nm (Figure S3). The CPO films, which were produced through the calcination of spin-coated methanolic solutions of metal nitrates in citric acid, are uniform thin films with some nanoscale defects (Figure S4). X-ray diffraction (XRD) of the thin films show little change with Pr loading, and the presence of gold only influences the XRD patterns by introducing a gold reflection; analysis of the Scherrer grain size shows minimal change with Pr loading, even to $25\%_{n/n}$ (Figure S5). The concentration of Pr was confirmed by XPS, and in good agreement with expected concentration (94% of expected, Figure S6); the deviation

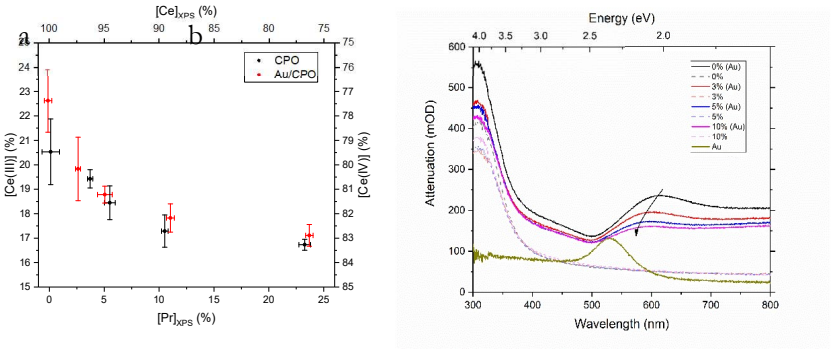

Figure 2: a) Concentration of Ce(III) and Ce(IV), as determined by XPS, with changing praseodymium loading. The presence of AuNPs has no significant effect. b) UV-Vis spectra for AuNP/CPO and CPO thin films with different mol% of praseodymium. With increased [Pr] loading, the damping of the AuNP LSPR increases, resulting in a broader and less intense and blue shifted attenuation (arrow).

from expected is likely due to the uncertain concentration of water in the $Pr(NO_3)_3 \bullet nH_2O$. The X-ray Photoelectron Spectroscopy (XPS) of both Pr and Ce can give insight to the oxidation state; and indicates a slight decrease in Ce(III) concentration relative to Ce(IV) with Pr loading, although the statistical relevance of this change is minimal (Figure 2a, representative XPS data shown in Figure S7 and S8).

The steady state UV-Vis spectra are shown in Figure 2b, clearly showing the CPO bandgap (E_g = 3.1 eV, Figure S9) and the AuNPs LSPR (603 ± 7 nm) and inter-band transition (λ < 454 ± 11 nm); spectral deconvolution[48] is shown in Figure S10. There are two interesting features to note about the effect that praseodymium loading has on the spectra: 1) that there is no change in the bandgap, and 2) that the LSPR broadens, decreases in intensity and shows a blueshift. The first feature, that the CPO films in the absence of AuNPs have near identical spectra (with a band gap of 3.1 eV, independent of [Pr], Figure 2b, tauc plot shown in Figure S9), is likely due to the very thin films having been calcined in ambient air and therefore are likely highly oxidized. This is supported by the XPS data which show very little change in the oxidation state of the cerium with increasing Pr loading, and no meaningful change in the oxidation state of the praseodymium. Interestingly, with thicker films (produced with 0.3 M solutions of metal nitrate) a more striking change in the steady state UV-Vis spectrum is seen (Figure S11). The second feature, that the Au LSPR appears to lessen in intensity, and blueshift with an increased [Pr], is a demonstration of the LSPR damping which is indicative of a decrease in LSPR lifetime (spectral

deconvolution shown in Figure S11)[48,49], and strong interaction with the environment, and is consistent with an increase in the extent of either CID or PIRET.[5,17,20,50] The presence of the blueshift seen in Figure 2b is interesting, and spectral deconvolution[48] of the Au/CPO samples with an additional mode to account for the broad near infrared (NIR) feature suggests there may not be a consistent blueshift. The deconvolution shows that the dominant peak is located at 611 nm for the $0\%_{Pr}$ sample, at 597 nm with $3\%_{Pr}$, at 609 nm with $5\%_{Pr}$, and at 598 nm with $10\%_{Pr}$. The presence of a second peak may be indicative of interference between the plasmon modes of the gold nanoparticle.[51] Barring the presence of a second peak, the blueshift may originate from the addition of the praseodymium, as PrO_x films have a refractive index of ~1.6 (depending on oxidation state) near 600 nm,[52] while the refractive index of CeO_x exceeds 2.[53] From the steady state spectra alone it cannot be concluded what mechanism is dominant: Transient absorption (TA) spectroscopy studies have therefore been carried out.

2.2 Effect Pr loading on ultrafast photodynamics

In Figure 3 TA contour plots and the spectra at selected time delays between pump and probe are shown for Au/CPO samples excited with 600 nm pulses. This wavelength was selected to minimize inter-band excitation while maximizing LSPR excitation; additionally, it still retains spectral overlap between the gold and CPO visible attenuation allowing PIRET. In the TA spectra there are several key features to note. First, at early delay times there is an intense photobleach near the LSPR resonance (~600 nm) and a related positive signal at ~500 nm. These are the well-known features of excited electrons in plasmonic nanoparticles.[9,54–56] Generally these features develop with time, and show a sequential decay, first during e-e coupling in ~500 fs, and then more sharply over ~10 ps during e-ph coupling; finally the feature slowly (100's ps) dissipates as the lattice cools.[12,54,57] Secondly, the broader weak photobleach from 600-750 nm at early times observed in the $10\%_{Pr}$ sample only, is indicative of a depopulation of a broad spectral feature. Third, the signal in the near-infrared (NIR) which is predominantly seen in the $0\%_{Pr}$ sample, but also seems weakly present in the 10% sample, is indicative of a O_{2p} to $Ce^{3+}{}_{4f}$ transition in the CeO_2 which is likely formed by the introduction of a vacancy in the usually populated $Ce^{3+}{}_{4f}$ band.[37–41]

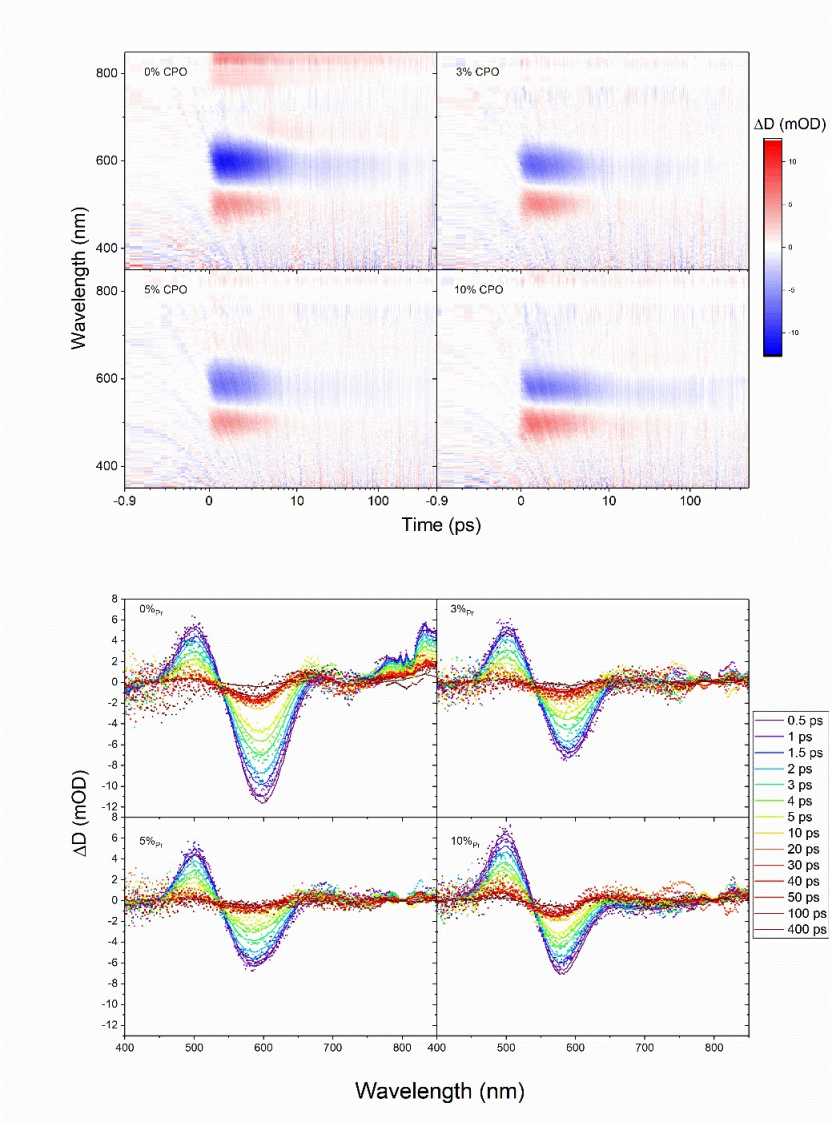

Figure 3: TA contour plots and spectra for the change in attenuation (ΔD) of Au/CPO layers with different [Pr] loading, on excitation with 600 nm pulses. There is an attenuation of signal at 800 nm owing to filters to cut the white light generation seed. Fits from target analysis are included as solid lines; this will be discussed in the next section.

2.3 Photophysical modeling

In order to properly interpret the TA data, a model was developed for target analysis in Glotaran (Figure 4), and fit to the data.[58] This model fit the data well and describes the spectra well (Figure 5). The model used here consists of four species each with an individual species associated spectrum (SAS): a short-lived non-equilibrated species (non-eq), a carrier species, a thermalized electron species (T_e), and a thermalized lattice species (T_l). Only the non-eq and carrier species were modeled as present at excitation, as this represents the dephasing of the LSPR allowing for CID and PIRET. This non-eq. species allows for the deconvolution of non-equilibrated hot-electrons from changes to the charge density (that is, this species is instrumental in disambiguating CID, and BCT). The non-eq. species has two competitive decay paths, one to the carrier species which represents the BCT mechanism, and the other to the T_e species representing e-e coupling. As a decay in the LSPR signal occurring over ~500 fs was observed for all samples, a time constant of 5 ps^{-1} was used for both, this value is consistent with existing literature.[59] The T_e component decays sequentially into T_l and then the ground state, these were found to have a rate of 0.3 ps^{-1} and 0.004 ps^{-1} based on global analysis of the samples. The carrier signal was modeled as decaying with a rate constant of 0.001 ps^{-1}, this value was taken from literature[60] with consideration for the results. The modelling of carriers into heat resulted in overfitting in Glotaran, so they were set to decay into the ground state for the model. During the model fitting the spectra where allowed the vary, but the times were not. As there was no evidence of carrier signal development after ~500 fs, no TCT component was included. The model provided species associated spectra (SAS) for each of the modeled species (Figure 5): SAS_{non-eq}, $SAS_{carrier}$, SAS_{Te}, and SAS_{Tl}.

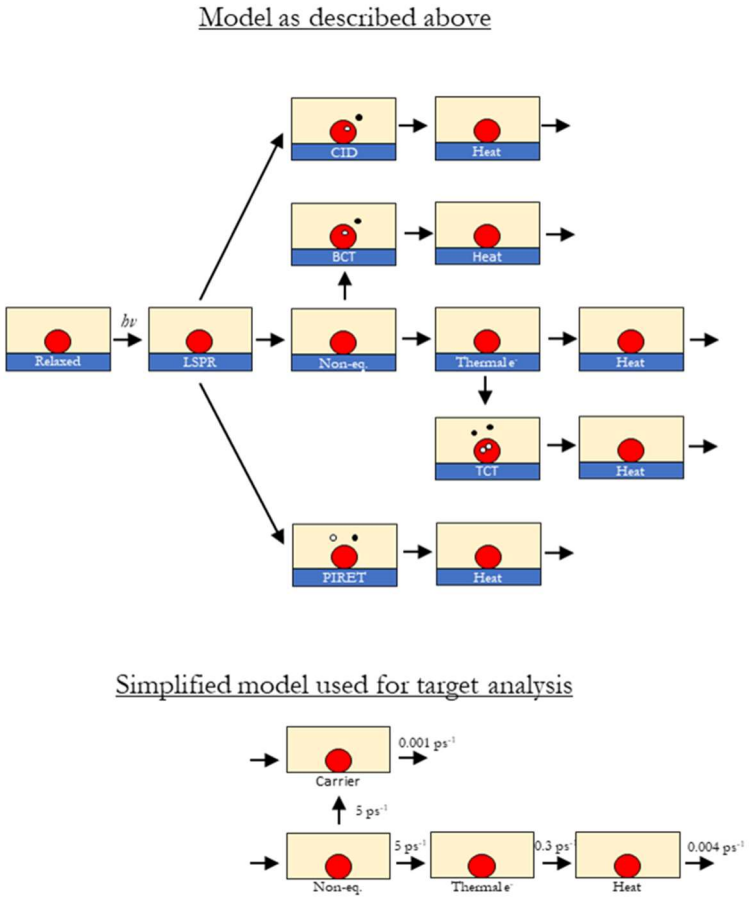

Figure 4: Schematic representation of the photophysical model, as described and as used for TA target analysis to produce the species associated spectra (SAS, see Fig. 6): a short-lived non-equilibrated species (non-eq), a carrier species, a thermalized electron species (T_e), and a thermalized lattice species (T_l). Competition exists between thermal relaxation (e-e coupling, e-ph coupling, and heat dissipation) and energy or charge transfer to CPO through PIRET, CID, and BCT. White and black circles represent either an electron or a hole. The gold nanoparticle (red circle) is supported on quartz (blue) and encased in CPO (yellow). Charge carriers in CPO are assumed to decay non-radiatively and produce heat; however, the contribution was found to be minimal (perhaps due to a multiple-step decay) and excluded from target analysis.

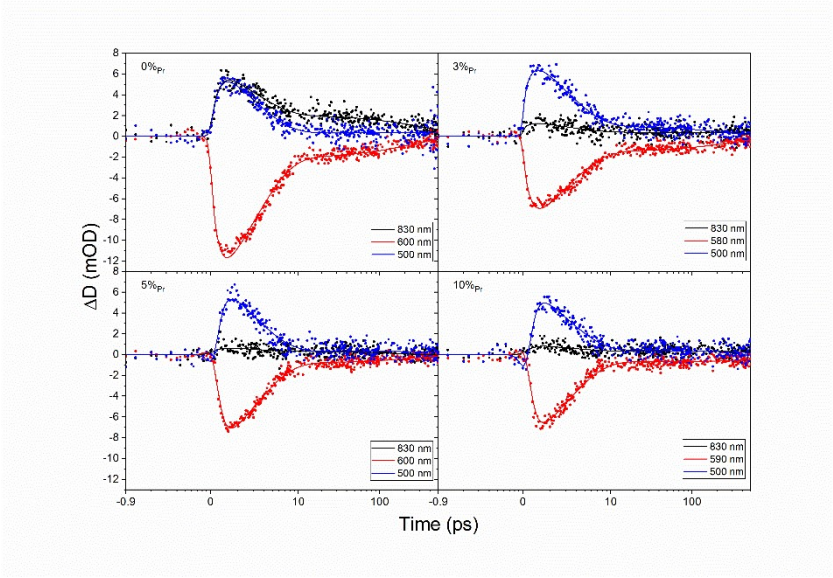

Figure 5: Kinetic traces (dots) for the four samples with different %$_{Pr}$ loading at 830 nm (representative of hole transfer to the CPO), and at the maximum (580-600 nm) and minimum (500 nm) of the LSPR induced transient feature. The solid lines indicate fits from target analysis.

Figure 5 shows the kinetic traces at key wavelengths: 830 nm (representative of hole transfer to the CPO), and at the maximum (580 - 600 nm) and minimum (500 nm) of the LSPR induced transient feature. The model (fits are included as solid lines) describes the ingrowth of the transient signal and change in rate at 10 ps accurately. For most samples, the early time is well described; however, the 600 nm trace of the 0%$_{Pr}$ and the 500 nm trace of the 5%$_{Pr}$ show a discrepancy between 0-2 ps. This is likely due to a mediocre fitting of the e-e scattering component, which in the model shares a rate with BCT (decoupling of the two led to significant overfitting). Despite the imperfect fit, the model still describes the data reasonably well, but it must be kept in mind that there is likely more e-e scattering occurring in the 0%$_{Pr}$ sample, and less in the 5%$_{Pr}$ sample than shown in the SAS. Additionally, noting the 830 nm transient, it is clear that there is considerable signal in the 0%$_{Pr}$ sample, but the others are less clear: the 3%$_{Pr}$ and 5%$_{Pr}$ samples have a trace which is non-zero for only ~1 ps, the 10%$_{Pr}$ sample shows non-zero intensity until nearly 10 ps. Given that the data is well described, it is sensible to then consider the SAS generated by the model, which are presented in Fig. 6.

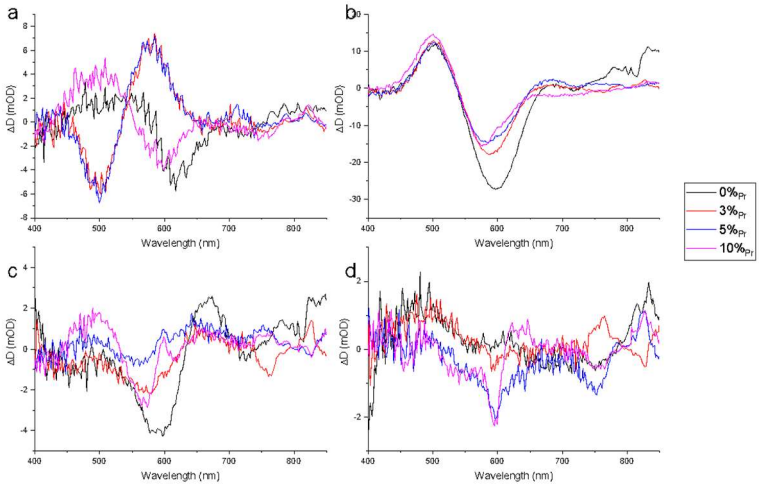

Figure 6: Species associated spectra (SAS) for the photophysical model shown in Figure 4. A) for the non-equilibrium period of the system, b) for the T_e component presenting thermal electrons, c) for the T_l component presenting heat generation, and d) for the carriers in the CPO component.

Beginning with the $SAS_{non\text{-}eq.}$ (Figure 6a) there is a divide: the $0\%_{Pr}$ and $10\%_{Pr}$ samples have approximately similar $SAS_{non\text{-}eq}$, as do the $3\%_{Pr}$ and the $5\%_{Pr}$. The $0\%_{Pr}$ sample shows a dip at 600 nm, and a slight rise in the higher energy region, this is characteristic of non-equilibrium electrons in AuNPs;[28,55] additionally, there is a small rise in the NIR, which may be indicative of an O_{2p} to $Ce^{3+}{}_{4f}$ transition in the CeO_2 which is formed by the introduction of a vacancy in the usually populated $Ce^{3+}{}_{4f}$ band[37–41]. The $10\%_{Pr}$ sample is quite similar, although slightly blueshifted (likely due to the apparent blueshift in the steady state attenuation spectrum). Strikingly, the $3\%_{Pr}$ and $5\%_{Pr}$ are near identical, and resemble nothing so much as a red-shift; it is likely that this feature is due to the loss of electron density in the AuNPs, which is known to result in a red-shift of the LSPR.[32] From the $SAS_{non\text{-}eq.}$ we can deduce that within the instrumental time resolution, light-induced charge transfer has already occurred for the $3\%_{Pr}$ and $5\%_{Pr}$ samples, likely through the CID mechanism, while non-equilibrium electrons are present in the Au nanoparticles for the $0\%_{Pr}$ and the $10\%_{Pr}$ samples.

The second SAS to consider is SAS_{Te} (Figure 6b), and there are two features to be discussed: the significant decrease in attenuation centered at 600 nm and a rise at 500 nm, and the more subtle differences at 600 nm – 800 nm. The former feature is quite comparable to the calculated Mie extinction for the gold nanoparticles at different temperatures (Figure S13a),[10,61] and is indicative of the temperature.[28] When the SAS_{Te} is scaled to the steady state UV-Vis attenuation at 600 nm, the difference in the magnitude of the spectra between samples becomes insignificant (Figure S13). That is to say, the amount of heating of the electrons in the Au nanoparticles appears to be more closely related to the total light attenuation, rather than changing with the concentration of praseodymium. The second feature to note is in the NIR: in the $0\%_{Pr}$ sample the TA signal between 700 nm – 800 nm matches the expected signal from a depopulation of the $Ce^{3+}{}_{4f}$ band. This is consistent with a previous study which showed that the population of the $Ce^{4+}{}_{5d6s}$ band after photoexcitation of plasmonic silver nanoparticles will have a component which follows the T_e regime in addition to the long-lived component.[9] In the $10\%_{Pr}$ sample there is a very different feature: a broad attenuation of ~2 mOD from 600 nm to 800 nm. This feature changes the shape of the decreased attenuation at 600 nm and appears to be a broad photobleach in the spectrum, suggesting the depopulation of a band with mild attenuation throughout the low photon energy side of the spectrum. This could be an indication of PIRET, as the transfer of energy resulting in a transition in the acceptor would lead to the depopulation of a band with spectral overlap with the LSPR.[17] Interestingly, when the samples were later measured again to acquire a finer resolution on short time scales, the signal near 830 nm was not observed, and the broad bleach with $10\%_{Pr}$ was only seen in the non-eq. species (Figure S14). This may indicate that atmospheric hydration quenched much of the charge or energy transfer, and calls for greater study of the system.

The SAS_{Tl} (Figure 6c) largely shows the characteristic spectra of hot gold nanoparticles;[28] however, the $0\%_{Pr}$ sample shows a notable red-shift which the other samples do not. This red-shift is likely due to the heating of the local environment, resulting in an increase in the index of refraction of the CPO (Figure S12b)[62]. The $0\%_{Pr}$ SAS_{Tl} differs from the SAS_{Te} significantly, possibly indicating substantial generation of heat; interestingly, this is substantially reduced for samples containing Pr. This suggests that there may be more energy or charge transfer than is observed in the NIR.

The $SAS_{carrier}$ (Figure 6d) describes the 830 nm feature indicative of an O_{2p} to $Ce^{3+}{}_{4f}$ transition in the CPO, which is formed by the introduction of a vacancy in the usually populated $Ce^{3+}{}_{4f}$ band.[32,33,37–41] This feature is unambiguous for the $0\%_{Pr}$ and present in the $10\%_{Pr}$ systems, but is absent for $3\%_{Pr}$ and $5\%_{Pr}$. Although there

is a degree of overfitting for 3%$_{Pr}$ and 5%$_{Pr}$, as there are sharp features seen near 800 nm with the inverse the SAS_{TI} and relative populations result in the fitting of the insignificant signal seen in the TA data. Accordingly, when considering the $SAS_{carrier}$ in the context of the actual TA signals, there is not considerable evidence for a O_{2p} to $Ce^{3+}{}_{4f}$ transition for the 3%$_{Pr}$ and 5%$_{Pr}$ samples. There may be a slight blueshift in the $SAS_{carrier}$ as well, but the signal to noise of the spectrum makes this a difficult assignment. If there is indeed a blueshift, it may be due to a change in the index of refraction of the CPO due to the change in carrier population and distribution, as similar effects have been seen in other materials.[63]

To summarize, there is evidence at the earliest times (<100 fs, during LSPR dephasing) that there is charge transfer in samples with 3%$_{Pr}$ and 5%$_{Pr}$, likely through CID, and of PIRET occurring with 10%$_{Pr}$. In the 0%$_{Pr}$ sample charge transfer likely takes place after LSPR dephasing by Landau damping, attributed to BCT of non-equilibrium electrons, with a lack of evidence of PIRET, CID, or TCT. This suggests that the dominant photosensitization mechanism varies notably with praseodymium loading: with BCT likely being dominant in the absence of Pr, CID likely being dominant for 3%$_{Pr}$ and 5%$_{Pr}$, and PIRET likely becoming significant for 10%$_{Pr}$ loading. These results have significant implications for utilization of plasmonic nanoparticles for the sensitization of semiconductors. The ability to tune the mechanism of sensitization allows for greater control; while PIRET can function across an insulating barrier,[30] CID does not, as it requires the direct interfacial contact.[18–20] The sensitization of semiconductors towards PIRET, if in electrical contact with the nanoparticle may also demonstrate enhanced CID, which while this may complicate academic studies, may also be of great benefit for photocatalytic or photovoltaic processes. Since PIRET relies on both the spectral overlap of materials and on the excitation dephasing in the semiconductor being faster than in the nanoparticle,[17] it is possible that the lower Pr loadings, while having a moderate spectral overlap, do not promote dephasing in the semiconductor. This may be due to the change in Pr ionization energy with loading (a ~0.5 eV decrease from >1%$_{Pr}$ to 10%$_{Pr}$).[64]

2.4 Conclusion

In this work we show by fs transient absorption spectroscopy that photoexcited gold sensitized cerium-praseodymium oxide undergoes charge or energy transfer through different mechanisms depending on the praseodymium content. For samples without praseodymium the dominant mechanism appears to be BCT, and there is notable heat generation at longer times. For samples with praseodymium the mechanism varies: low loading (3%$_{Pr\ n/n}$, and 5%$_{Pr\ n/n}$) are likely dominated by CID, while 10%$_{Pr\ n/n}$ likely demonstrates significant PIRET, consistent with steady state

absorption spectra showing that LSPR damping increases with praseodymium loading. This study establishes that the sensitization of ceria towards PIRET by Pr doping may additionally promote CID. While the study has been carried out on CPO with AuNPs, the findings may extend to other systems; accordingly, tuning the mechanism of sensitization of semiconductors with plasmonic materials to allow for multiple mechanisms could allow for increased light to carrier conversion efficiency.

3 Experimental methods

3.1 AuNP synthesis

Gold nanoparticles were synthesized using the established Turkevich method:[65,66] 50 mL of 38.8 mM sodium citrate (Sigma, 99%) was added to 500 mL of boiling 1 mM $HAuCl_4$ (Sigma, 99.995%) and allowed to boil for 15 minutes before being cooled. The yellow $HauCl_4$ became transparent and then progressed to a deep red color. The solution was cooled, and then stored for extended periods of time at 4°C in a glass vessel.

3.2 Au/CPO thin film preparation

Quartz substrates were prepared soaking for 15 minutes in first aqua regia, and then piranha, and then were rinsed thoroughly with water. For the deposition of gold, the slides from above were placed in an ethanoic $1\%_{v/v}$ 3-ainopropyl trimethoxy silane (APTMS, alfa) solution for 1 h. The slides were then very well rinsed with first 10 times with ethanol, then 10 times with water, before being placed in a solution of gold particles, prepared by the Turkevich method,[65,66] overnight. If any trace of APTMS or ethanol remains, the gold particles will aggregate and fall out of solution, producing a substandard film. After gold colloid deposition, the films were calcined at 500°C for 5 hours. The size and loading of gold particles was determined from SEM (Figure S3a) using ImageJ particle analyzer (bimodal distribution with 75 ± 6% of particles 40 ± 10 nm in diameter, and 24 ± 2% 25 ± 5 nm, Figure S3b). Removal of a portion of the Au nanoparticles on the covered slide, to act as a control, was done through simple manual abrasion.

Synthesis of cerium praseodymium oxide (CPO) was done through a modification of established spin-coat sol-gel methods.[67,68] In brief, a solution of methanol containing 0.06 M ($Ce(NO_3)_3$ + $Pr(NO_3)_3$) and 0.5 M citric acid was prepared, and allowed to age at room temperature for not less than 48 hours; after which a pale yellow-green colour was observed. This solution was then used as is, and 0.2 mL was placed on 10x30x2 mm quartz substrates and spun at 3500 RPM for 15 seconds. The films where then calcined in air at 500°C for 5 h (10°C/min

ramp rate). The CPO could be removed with Aqua Fortis, and the gold film would be recovered; while the films used in this study were fresh films, the recovery of the gold film was a strong indicator that the gold nanoparticles remain on the quartz/CPO interface after CPO annealing. Films were characterized with XRD, XPS, SEM, and UV-Vis. A photograph of the prepared films is shown in Figure S15.

3.3 Transient absorption

Femtosecond transient absorption experiments were performed using a home-built setup. The initial 800 nm pulses (FWHM 35 ± 1 fs) were produced by a Ti:Sapphire amplifier (Coherent Legend) operating at 5 kHz repetition rate. The output was split into two beams using a 90:10 beam splitter. The pump beam was generated by sending the major part of the 800 nm beam into an optical parametric amplifier (Coherent, Opera), producing pulses with tunable center wavelength and a pulse duration of ca. 50 fs FWHM. The differential absorbance between pump on and off was obtained by chopping the pump beam at 2.5 kHz. The pump was further attenuated using a neutral density filter. The white light continuum probe was produced through supercontinuum generation by guiding the remaining part of the 800 nm beam through a mechanical delay stage, variable neutral density filter wheel and focusing into a CaF_2 crystal (Newlight Photonics, 3 mm thickness, 001-cut, uncoated, the crystal was continuously moved to prevent damage). A NIR neutral density filter was used to attenuate the 800 nm seed pulse while allowing for detection to 840 nm.. The polarizations of the pump and probe were set to 54.7° (magic angle) to avoid anisotropy effects.[69,70] The pump was focused to a spot of ca. 250 μm diameter, significantly larger than the focused probe spot (ca. 100 μm diameter) and it is thus reasonable to assume that we probe a homogeneously photoexcited sample. Detection of the signal was achieved using a 15 cm spectrograph coupled to a 256-pixel diode array detector. The time resolution was determined to be 100 – 150 fs, and the TA signal decay was verified to not be caused by persistent effects. The pump power was kept relatively low (~5 x 10^{14} photons/(cm^2 pulse)) and verified to be in the linear regime. The UV-Vis extinction of the samples was verified to be identical before and after experiments to ensure that no significant permanent bleaching. Data analysis was performed using Matlab for chirp correction and Glotaran[58] for fitting.

4 References

1. Qi, J., Dang, X., Hammond, P. T. & Belcher, A. M. Highly efficient plasmon-enhanced dye-sensitized solar cells through metal@oxide core-shell nanostructure. *ACS Nano* **5**, 7108–7116 (2011).

2. Su, Y. H., Ke, Y. F., Cai, S. L. & Yao, Q. Y. Surface plasmon resonance of layer-by-layer gold nanoparticles induced photoelectric current in environmentally-friendly plasmon-sensitized solar cell. *Light Sci. Appl.* **1**, 2–6 (2012).

3. Brown, M. D. *et al.* Plasmonic dye-sensitized solar cells using core-shell metal-insulator nanoparticles. *Nano Lett.* **11**, 438–445 (2011).

4. Christopher, P., Xin, H. & Linic, S. Visible-light-enhanced catalytic oxidation reactions on plasmonic silver nanostructures. *Nat. Chem.* **3**, 467–472 (2011).

5. Therrien, A. J. *et al.* Impact of chemical interface damping on surface plasmon dephasing. *Faraday Discuss.* **214**, 59–72 (2019).

6. Mukherjee, S. *et al.* Hot electrons do the impossible: Plasmon-induced dissociation of H_2 on Au. *Nano Lett.* **13**, 240–247 (2013).

7. Knight, M. W., Sobhani, H., Nordlander, P. & Halas, N. J. Photodetection with Active Optical Antennas. *Science* **332**, 702–704 (2011).

8. Ingram, D. B. & Linic, S. Water splitting on composite plasmonic-metal/semiconductor photoelectrodes: Evidence for selective plasmon-induced formation of charge carriers near the semiconductor surface. *J. Am. Chem. Soc.* **133**, 5202–5205 (2011).

9. Pelli Cresi, J. S. *et al.* Highly efficient plasmon-mediated electron injection into cerium oxide from embedded silver nanoparticles. *Nanoscale* **11**, 10282–10291 (2019).

10. Willets, K. A. & Van Duyne, R. P. Localized Surface Plasmon Resonance Spectroscopy and Sensing. *Annu. Rev. Phys. Chem.* **58**, 267–297 (2007).

11. Maestro, L. M. *et al.* Quantum dot thermometry evaluation of geometry dependent heating efficiency in gold nanoparticles. *Langmuir* **30**, 1650–1658 (2014).

12. Brongersma, M. L., Halas, N. J. & Nordlander, P. Plasmon-induced hot carrier science and technology. *Nat. Nanotechnol.* **10**, 25–34 (2015).

13. Christopher, P. & Moskovits, M. Hot Charge Carrier Transmission from Plasmonic Nanostructures. *Annu. Rev. Phys. Chem.* **68**, 379–398 (2017).

14. Guillon, C., Langot, P., Del Fatti, N. & Vallee, F. Ultrafast surface plasmon resonance Landau damping and electron kinetics in metal nanoparticles. in *Ultrafast Phenomena in Semiconductors and Nanostructure Materials VIII* (eds. Tsen, K.-T., Song, J.-J. & Jiang, H.) **5352**, 65 (2004).

15. Kawabata, A. & Kubo, R. Electronic Properties of Fine Metallic Particles. II. Plasma Resonance Absorption. *J. Phys. Soc. Japan* **21**, 1765–1772 (1966).

16. Baffou, G. & Quidant, R. Thermo-plasmonics: using metallic nanostructures as nano-sources of heat. *Laser Photon. Rev.* **7**, 171–187 (2013).

17. Li, J. *et al.* Plasmon-induced resonance energy transfer for solar energy conversion. *Nat. Photonics* **9**, 601–607 (2015).

18. Kale, M. J. & Christopher, P. Plasmons at the interface. *Science* **349**, 587–588 (2015).

19. Wu, K., Chen, J., McBride, J. R. & Lian, T. Efficient hot-electron transfer by a plasmon-induced interfacial charge-transfer transition. *Science* **349**, 632–635 (2015).

20. Foerster, B. *et al.* Chemical Interface Damping Depends on Electrons Reaching the Surface. *ACS Nano* **11**, 2886–2893 (2017).

21. Liu, Y., Chen, Q., Cullen, D. A., Xie, Z. & Lian, T. Efficient Hot Electron Transfer from Small Au Nanoparticles. *Nano Lett.* **20**, 4322–4329 (2020).

22. Furube, A., Du, L., Hara, K., Katoh, R. & Tachiya, M. Ultrafast plasmon-induced electron transfer from gold nanodots into TiO_2 nanoparticles. *J. Am. Chem. Soc.* **129**, 14852–14853 (2007).

23. Chou, K. C., Westerberg, S., Shen, Y. R., Ross, P. N. & Somorjai, G. A. Probing the charge-transfer state of CO on Pt(111) by two-dimensional infrared-visible sum frequency generation spectroscopy. *Phys. Rev. B - Condens. Matter Mater. Phys.* **69**, 1–4 (2004).

24. Kale, M. J., Avanesian, T., Xin, H., Yan, J. & Christopher, P. Controlling Catalytic Selectivity on Metal Nanoparticles by Direct Photoexcitation of Adsorbate–Metal Bonds. *Nano Lett.* **14**, 5405–5412 (2014).

25. Petek, H., Weida, M. J., Nagano, H. & Ogawa, S. Real-time observation of adsorbate atom motion above a metal surface. *Science* **288**, 1402–1404 (2000).

26. Agrawal, H. & Garnett, E. C. Nanocube Imprint Lithography. *ACS Nano* **14**, 11009–11016 (2020).

27. Merschdorf, M., Kennerknecht, C. & Pfeiffer, W. Collective and single-particle dynamics in time-resolved two-photon photoemission. *Phys. Rev. B* **70**, 193401 (2004).

28. Link, S. & El-Sayed, M. A. Spectral Properties and Relaxation Dynamics of Surface Plasmon Electronic Oscillations in Gold and Silver Nanodots and Nanorods. *J. Phys. Chem. B* **103**, 8410–8426 (1999).

29. Silverstein, T. P. Marcus Theory: Thermodynamics CAN Control the Kinetics of Electron Transfer Reactions. *J. Chem. Educ.* **89**, 1159–1167 (2012).

30. Cushing, S. K. *et al.* Controlling Plasmon-Induced Resonance Energy Transfer and Hot Electron Injection Processes in Metal@TiO_2 Core–Shell Nanoparticles. *J. Phys. Chem. C* **119**, 16239–16244 (2015).

31. Sayed, M., Zhang, L. & Yu, J. Plasmon-induced interfacial charge-transfer transition prompts enhanced CO_2 photoreduction over Cu/Cu_2O octahedrons. *Chem. Eng. J.* **397**, 125390 (2020).

32. Sheldon, M., van de Groep, J., Brown, A., Polman, A. & Atwater, H. Plasmoelectric potentials in metal nanostructures. *Science* **346(6211)**, 868-831 (2014).

33. Van De Groep, J., Sheldon, M. T., Atwater, H. A. & Polman, A. Thermodynamic theory of the plasmoelectric effect. *Sci. Rep.* **6**, 23283 (2016).

34. Murgida, G. E., Ferrari, V., Ganduglia-Pirovano, M. V. & Llois, A. M. Ordering of

oxygen vacancies and excess charge localization in bulk ceria: A DFT+U study. *Phys. Rev. B - Condens. Matter Mater. Phys.* **90**, 115120 (2014).

35. Logan, A. D. & Shelef, M. Oxygen availability in mixed cerium/praseodymium oxides and the effect of noble metals. *J. Mater. Res.* **9**, 468–475 (1994).

36. Stefanik, T. S. & Tuller, H. L. Nonstoichiometry and defect chemistry in praseodymium-cerium oxide. *J. Electroceramics* **13**, 799–803 (2004).

37. Michel, K., Bjørheim, T. S., Norby, T., Janek, J. & Elm, M. T. Importance of the Spin-Orbit Interaction for a Consistent Theoretical Description of Small Polarons in Pr-Doped CeO_2. *J. Phys. Chem. C* **124**, 15831–15838 (2020).

38. Esch, F. *et al.* Electron localization determines defect formation on ceria substrates. *Science* **309**, 752–755 (2005).

39. Pelli Cresi, J. S. *et al.* Highly efficient plasmon-mediated electron injection into cerium oxide from embedded silver nanoparticles. *Nanoscale* **11**, 10282–10291 (2019).

40. Aškrabić, S. *et al.* F-centre luminescence in nanocrystalline CeO_2. *J. Phys. D. Appl. Phys.* **46**, 495306 (2013).

41. Cristina de Oliveira, R. *et al.* Charge transfer in Pr-Doped cerium oxide: Experimental and theoretical investigations. *Mater. Chem. Phys.* **249**, 122967 (2020).

42. Zhao, K. *et al.* Efficient water oxidation under visible light by tuning surface defects on ceria nanorods. *J. Mater. Chem. A* **3**, 20465–20470 (2015).

43. Jamshidijam, M. *et al.* Influence of rare earth (RE=Nd, Y, Pr and Er) doping on the microstructural and optical properties of ceria nanostructures. *Ceram. Int.* **43**, 5216–5222 (2017).

44. Guo, M., Lu, J., Wu, Y., Wang, Y. & Luo, M. UV and visible Raman studies of oxygen vacancies in rare-earth-doped ceria. *Langmuir* **27**, 3872–3877 (2011).

45. Venkataswamy, P. *et al.* Transition (Mn, Fe) and rare earth (La, Pr) metal doped ceria solid solutions for high performance photocatalysis: Effect of metal doping on catalytic activity. *Res. Chem. Intermed.* **44**, 1–21 (2017).

46. Bishop, S. R., Stefanik, T. S. & Tuller, H. L. Defects and transport in Pr xCe 1-xO 2-δ: Composition trends. *J. Mater. Res.* **27**, 2009–2016 (2012).

47. Borchert, H. *et al.* Electronic and chemical properties of nanostructured cerium dioxide doped with praseodymium. *J. Phys. Chem. B* **109**, 5728–5738 (2005).

48. Engelbrekt, C., Crampton, K. T., Fishman, D. A., Law, M. & Apkarian, V. A. Efficient Plasmon-Mediated Energy Funneling to the Surface of Au@Pt Core-Shell Nanocrystals. *ACS Nano* **14**, 5061–5074 (2020).

49. Etchegoin, P. G., Le Ru, E. C. & Meyer, M. An analytic model for the optical properties of gold. *J. Chem. Phys.* **125**, 164705 (2006).

50. Lee, S. Y. *et al.* Tuning Chemical Interface Damping: Interfacial Electronic Effects of Adsorbate Molecules and Sharp Tips of Single Gold Bipyramids. *Nano Lett.* **19**, 2568–2574 (2019).

51. Prezgot, D., Bottomley, A., Coyle, J. P. & Ianoul, A. Unusually Sharp Localized Surface Plasmon Resonance in Supported Silver Nanocrystals with a Thin Dielectric Coating. *J. Phys. Chem. Lett.* **8**, 5555–5558 (2017).

52. Goswami, A. & Goswami, A. P. Optical properties of praseodymium oxide films. *Thin Solid Films* **27**, 123–128 (1975).

53. Chiu, F.-C. & Lai, C.-M. Optical and electrical characterizations of cerium oxide thin films. *J. Phys. D. Appl. Phys.* **43**, 075104 (2010).

54. Hartland, G. V. Optical studies of dynamics in noble metal nanostructures. *Chem. Rev.* **111**, 3858–3887 (2011).

55. Link, S., Burda, C., Mohamed, M., Nikoobakht, B. & El-Sayed, M. Femtosecond transient-absorption dynamics of colloidal gold nanorods: Shape independence of the electron-phonon relaxation time. *Phys. Rev. B - Condens. Matter Mater. Phys.* **61**, 6086–6090 (2000).

56. Mohamed, M. B., Ahmadi, T. S., Link, S., Braun, M. & El-sayed, M. A. Hot electron and phonon dynamics of gold nanoparticles embedded in a gel matrix. *Chem. Phys. Lett.* **343**, 55–63 (2001).

57. Staleva, H. & Hartland, G. V. Vibrational Dynamics of Silver Nanocubes and Nanowires Studied by Single-Particle Transient Absorption Spectroscopy. *Adv. Funct. Mater.* **18**, 3809–3817 (2008).

58. Snellenburg, J. J., Laptenok, S., Seger, R., Mullen, K. M. & van Stokkum, I. H. M. Glotaran: A Java-based graphical user interface for the R package TIMP. *J. Stat. Softw.* **49**, 1–22 (2012).

59. Link, S., Burda, C., Wang, Z. L. & El-Sayed, M. A. Electron dynamics in gold and gold-silver alloy nanoparticles: The influence of a nonequilibrium electron distribution and the size dependence of the electron-phonon relaxation. *J. Chem. Phys.* **111**, 1255–1264 (1999).

60. Pelli Cresi, J. S. *et al.* Highly efficient plasmon-mediated electron injection into cerium oxide from embedded silver nanoparticles - Supporting Information. *Nanoscale* **11**, 10282–10291 (2019).

61. Reddy, H. *et al.* Temperature-Dependent Optical Properties of Plasmonic Titanium Nitride Thin Films. *ACS Photonics* **4**, 1413–1420 (2017).

62. Patsalas, P., Logothetidis, S. & Metaxa, C. Optical performance of nanocrystalline transparent ceria films. *Appl. Phys. Lett.* **81**, 466–468 (2002).

63. Bennett, B. R., Soref, R. A. & Del Alamo, J. A. Carrier-Induced Change in Refractive Index of InP, GaAs, and InGaAsP. *IEEE J. Quantum Electron.* **26**, 113–122 (1990).

64. Stefanik, T. S. Electrical Properties and Defect Structure of Praseodymium-Cerium Oxide Solid Solutions. (Massachusetts Institute of Technology, 2004). Section 6.2.5.2

65. Turkevich, J., Stevenson, P. C. & Hillier, J. A study of the nucleation and growth processes in the synthesis of colloidal gold. *Discuss. Faraday Soc.* **11**, 55-75 (1951).

66. Kimling, J. *et al.* Turkevich Method for Gold Nanoparticle Synthesis Revisited. *J. Phys. Chem. B* **110**, 15700–15707 (2006).

67. Verma, A., Bakhshi, A. K. & Agnihotry, S. A. Effect of citric acid on properties of CeO_2 films for electrochromic windows. *Sol. Energy Mater. Sol. Cells* **90**, 1640–1655 (2006).

68. Channei, D., Nakaruk, A., Phanichphant, S., Koshy, P. & Sorrell, C. C. Cerium dioxide thin films using spin coating. *J. Chem.* **2013** 579284 (2013).

69. Lessing, H. E. & von Jena, A. Separation of rotational diffusion and level kinetics in transient absorption spectroscopy. *Chem. Phys. Lett.* **46**, 213–217 (1977).

70. Schott, S., Steinbacher, A., Buback, J., Nuernberger, P. & Brixner, T. Generalized magic angle for time-resolved spectroscopy with laser pulses of arbitrary ellipticity. *J. Phys. B At. Mol. Opt. Phys.* **47**, 124014 (2014).

71. Link, S. & El-Sayed, M. A. Spectral Properties and Relaxation Dynamics of Surface Plasmon Electronic Oscillations in Gold and Silver Nanodots and Nanorods. *J. Phys. Chem. B* **103**, 8410–8426 (1999).

72. Li, J. *et al.* Plasmon-induced resonance energy transfer for solar energy conversion. *Nat. Photonics* **9**, 601–607 (2015).

73. Zhu, Q. *et al.* Stable blue TiO_{2-x} nanoparticles for efficient visible light photocatalysts**.** *J. Mater. Chem. A* **2**, 4429 (2014).

74. Haghighatzadeh, A. & Mazinani, B. Ag/CeO2 Schottky-type nanoheterostructures: Enhanced third-order nonlinear optical susceptibility under the near infrared irradiation. *Opt. Laser Technol.* **131**, 106426 (2020).

75. Christopher, P. & Moskovits, M. Hot Charge Carrier Transmission from Plasmonic Nanostructures. *Annu. Rev. Phys. Chem.* **68**, 379–398 (2017).

Appendix B: Supplementary information for Chapter 4

Section 1: Energy levels of Ce(Pr)Ox

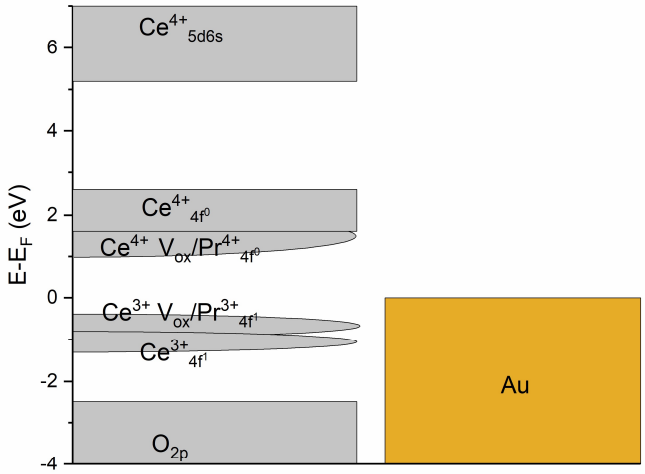

Figure S1: energy level diagram of Ce(Pr)O_x based on literature values.[37–41] The levels induced by praseodymium are near equivalent with those of oxygen vacancies in ceria; in this way increasing [Pr] mimics an increase in [V_{ox}]. Shown also is a gold surface with arrows indicating the range of excited carriers available with 2 eV photoexcitation.

The ceria valence band (VB) is comprised of the O_{2p} orbitals, while the conduction band (CB) originates from the empty $Ce^{4+}{}_{4f}$ orbitals with a band gap of ~3 eV (Figure S). There are additional levels stemming from $Ce^{3+}{}_{4f}$ orbitals, ~1.2-1.7 eV above the VB, and oxygen vacancies (V_{ox}) which populate the region between the Ce^{3+} and Ce^{4+}. The exact position of the V_{ox} depends on the electronic population: generally a V_{ox} acts as a trap for two electrons, and (partially) depopulating it will shift away from the Fermi level (E_F).[37–41]

The position of the Pr band depends on the concentration,[41,64] and on the oxidation state[37]. Specifically, that with increasing concentration the Pr band position varies slightly until by 10%$_{n/n}$ the Pr is no longer discreet states, but is instead a band at lower energy.[64] While the Pr is in discreet energy states the position of the Pr(IV) band is understood to be about 1 eV above E_F; however, upon reduction of the Pr to Pr(III) the band lowers to 1 eV below E_F due to spin orbit

coupling.[37] The result is that the praseodymium induced energy levels are very comparable to those induced by oxygen vacancies in the ceria.

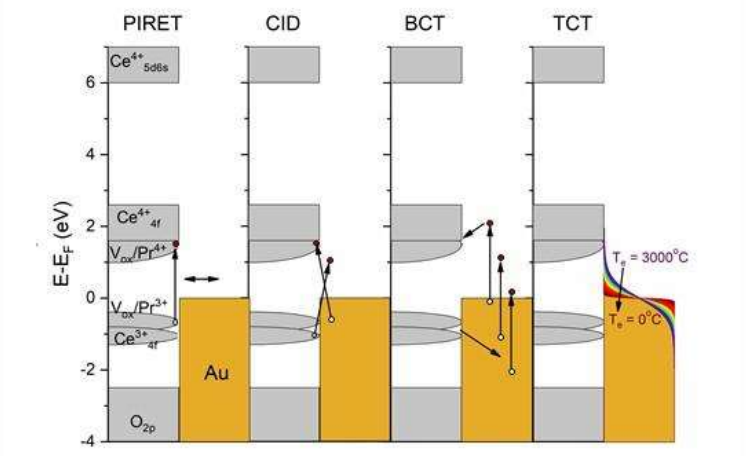

Figure S2: Proposed mechanisms of energy and charge transfer to the CPO from AuNP.

Each of the proposed mechanisms have some identifying features, either in the steady state (SS) or in the TA spectra. By noting these differences in the observations, it can be possible to determine which mechanisms occur. A summary of the features is shown in Table S1.

For CT there must be transitions which can occur for electrons promoted from the gold. This means that there must be some energy level at $E_F \pm h\nu$ so that either a ballistic electron or hole can transfer. Since ballistic carriers quickly undergo electron-electron interactions ($\tau_{e\text{-}e}$=500 fs)[71] after which thermalized electrons exist, then transitions of significantly less than $E_F \pm h\nu$ existing would allow for CT to occur. For CID the initial requirement of energy levels available at $E_F \pm h\nu$ stands; but additionally the additional damping caused by CID causes a broadening and decreased intensity of the LSPR.[20] The formation of a new absorption mode in the steady state spectra is an indication that there may be CID (although confirmation would require determining the quantum yield as it is invariant with excitation energy).[19] In contrast, if there is spectral overlap between the donor (LSPR) and acceptor (CPO) then PIRET may occur without the production of a new mode.[72]

Given the case of CPO, the $E_F \pm h\nu$ requirement for CT and CID make electron transfer to the $Ce^{4+}{}_{4f}$, the associated V_{ox} (both electronically vacant, or partially filled), or the Pr^{4+} bands available as there are acceptor levels at 1 to 2.6 eV.

Additionally, hole transfer to the $Ce^{3+}{}_{4f}$, the associated V_{ox} (both electronically vacant, or partially filled), or the Pr^{3+} bands can occur as the energy levels span -0.4 to -1.3 eV. Given that the hole acceptor levels are closer to E_F, and that the light energy is split between the electron and hole after LSPR dephasing, it is expected that the transfer of holes would be more likely than the transfer of electrons.

The TA spectra will show direct evidence of the mechanism, being that the population and depopulation of bands will induce spectral changes. The expected available transitions and expected minimum/maximum energies are shown in Table S2. The depopulation of a band, through the injection of a hole will result in a photoinduced bleach (PB) from that band but can cause a photoinduced absorption (PA) to that band. Additionally, PA bands can be formed by populating normally unpopulated bands with an electron, allowing transitions from that band.

It is worth comparing the expected results of CPO with TiO_2, as many spectroscopists may hold it as a standard for interpretation. When TiO_2 is photoexcited an IR signal forms due to the promotion of an electron to Ti resulting in the formation of Ti^{3+}. This results due to the proximity of the Ti conduction band to the Fermi level, and the proximity of the Ti^{3+} state to the Ti^{4+} band.[73] This differs considerably from CeO_2, where the Fermi level is reported as approximately half way between the O_{2p} and $Ce^{4+}{}_{5d6s}$ with the $Ce^{4+}{}_{4f}$ levels being 1 eV above E_F and $Ce^{3+}{}_{4f}$ levels being 1 eV below E_F.[41,74] It may be that population of the $Ce^{4+}V_{ox}$ band (or the Pr^{4+} band) would allow for very small excitations; however there does not appear to be literature of this occurring in CeO_2 at this time.

Table S1: Summary of the effects of the different mechanisms of CPO excitation by AuNP LSPR. Steady state changes are outlined in general, while the TA signals are outlined in more detail. Photoinduced absorption (PA) and photo-bleach (PB) can occur due to changes in electronic populations in the CPO.

	PIRET	CID	BCT	TCT
	Steady State			
	Spectral overlap[17,72] (LSPR coupling) [12,17]	LSPR coupling[12,17] spectral broadening and decreased attenuation[5,18–21]	Presence of donor/acceptor levels[18,29–31]	Presence of donor/acceptor levels[18,29–31]
	Transient Absorption			
e^-	345 nm PA[39]	345 nm PA[39]	345 nm PA[39]	345 nm PA[39]
h^+	830 nm PA[32,33,37–41] PB near excitation[17]	830 nm PA[32,33,37–41]	830 nm PA[32,33,37–41]	830 nm PA[32,33,37–41]
time	< 5 fs[12]	< 5 fs[12]	< 50 fs[12]	0.5-4 ps[12]
notes	Competitive with LSPR dephasing[17] Reduced heat generation with increased PIRET[12,17,30] PA/PB bands cannot form independent of one another[17]	Competitive with LSPR dephasing[19,20] Reduced heat generation with increased CID[12,18,19] LSPR shift due to change in electron density[5,19,32] PA bands can form independent of one another[19,75]	Competitive with e-e scattering[12,29] LSPR shift due to change in electron density[32] PA bands can form independent of one another[75]	Sequential with e-e scattering, competitive with e-ph coupling[12,29] LSPR shift due to change in electron density[32] PA bands can form independent of one another[75]

Table S2: The energies of possible transitions within CPO, redundant or symmetric transitions have not been shown for clarity.

From / To	O_{2p}	$Ce^{3+}{}_{4f}$	$Pr^{3+}/Ce^{3+}V_{ox}$	$Pr^{4+}/Ce^{4+}V_{ox}$	$Ce^{4+}{}_{4f}$
$Ce^{3+}{}_{4f}$	1.2/1.7				
Pr^{3+}/V_{ox}	1.7/2.1	-/0.9			
Pr^{4+}/V_{ox}	3.5/4.1	1.8/2.9	1.4/2.4		
$Ce^{4+}{}_{4f}$	4.1/5.1	2.4/3.9	2/3.4	-/1.6	
$Ce^{4+}{}_{5d6s}$	7.7	6/6.5	5.6/6	3.6/4.2	2.6/3.6

Section 2: Characterization of Au/CPO.

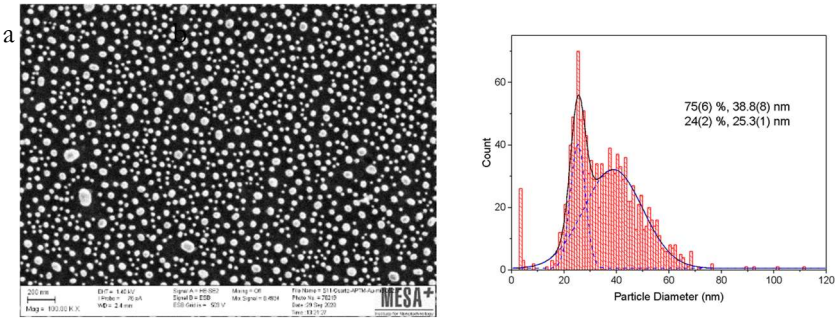

Figure S3: a) SEM micrograph and b) size distribution of gold nanoparticles on quartz. The surface density of gold nanoparticles was found to be 200.6 particles/μm^2.

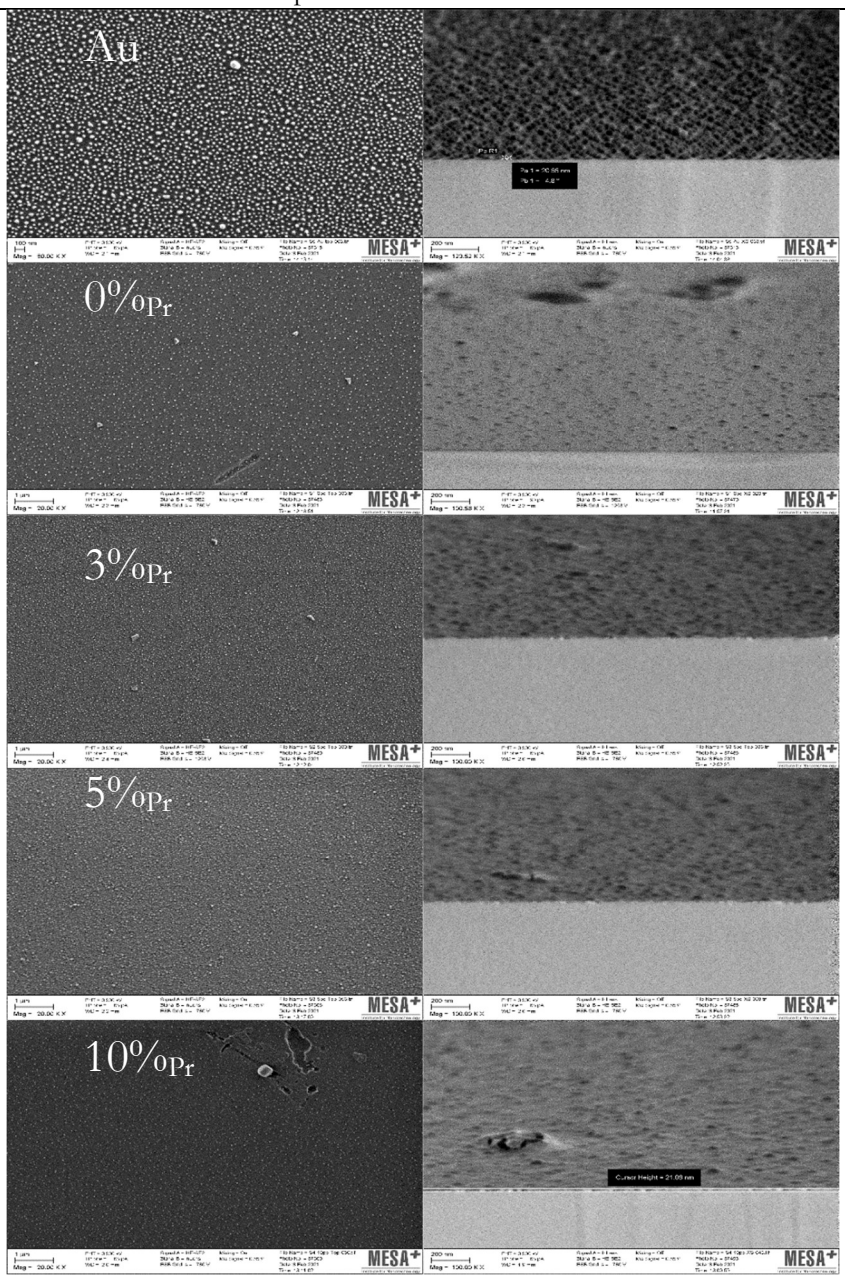

Figure S4: SEM images of samples, show both from top down and from 45°. This film is approximately 20 nm (specific thickness uncertain due to sample charging).

The gold film is a relatively dense film of spherical particles. There are charging effects which give rise to the bright spots on the 90° SEM micrographs.

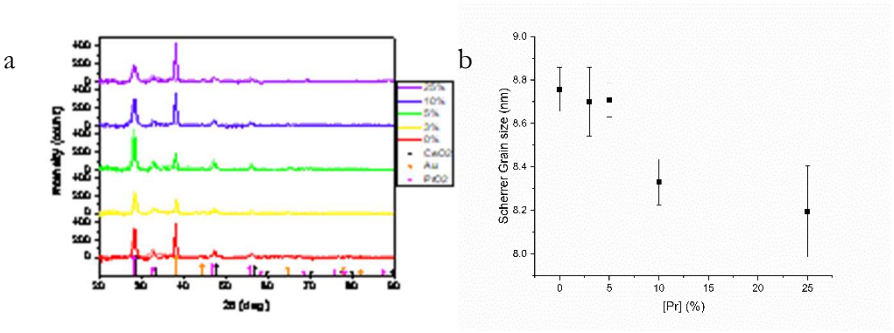

Figure S5: a) Stacked XRD of Au/CPO samples showing little change with the addition of Pr or Au (COD card entries: CeO_2 00-721-7887, PrO_2: 00-900-9031). b) Scherrer grain size based on the dominant XRD peak near 29°.

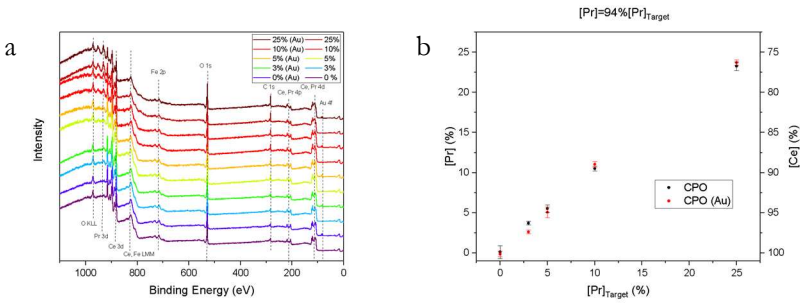

Figure S6: a) XPS spectra for all sample, including to 25% Pr and determination of actual loading. With no metal not accountable as part of the XPS instrument (Fe and C), the mixed metal oxide can be determined to be of only the expected cerium-praseodymium oxide; with b) $[Pr]_{actual}$ found to be 94% of $[Pr]_{target}$. The difference is attributed to the unknown hydration state of the salt used.

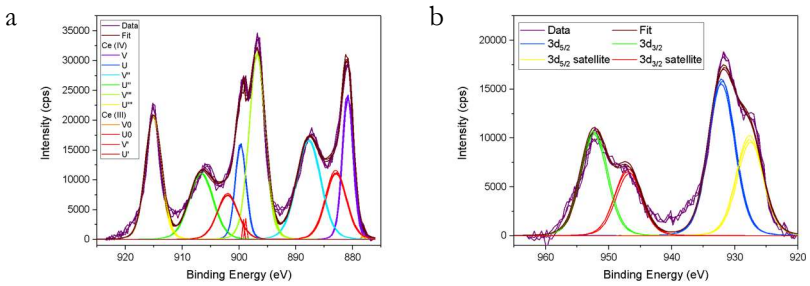

Figure S6: XPS of Ce (a) and Pr (b), showing peaks attributable to both the 3+ and 4+ states (V0, U0, V', and U' for Ce, satellite peaks for Pr). These were used to determine the relative concentration of Ce(III)/(Ce(III)+Ce(IV)) and of Pr/Ce. Note, that while the change in oxidation state for Pr was examined, there was no change in oxidation state of the Pr with loading.

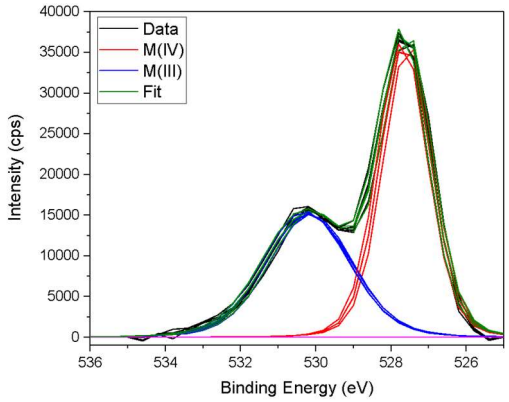

Figure S8: XPS of the O1s peak, with two states owing to M(IV) and M(III) species.

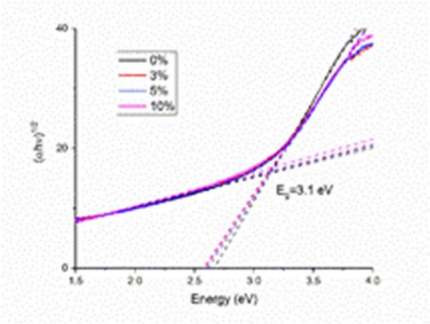

Figure S9: Tauc plot of thin films of CPO, showing an invariance in the CeO_x band gap with Pr loading concentration, while the visible component increases owing to the inclusion of praseodymium.

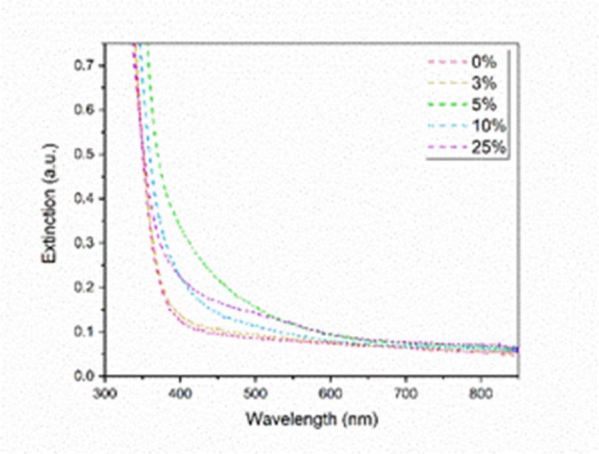

Figure S10: UV-Vis of Au/CPO with thicker films of CPO (estimated to be hundreds of nm based on literature).[68]

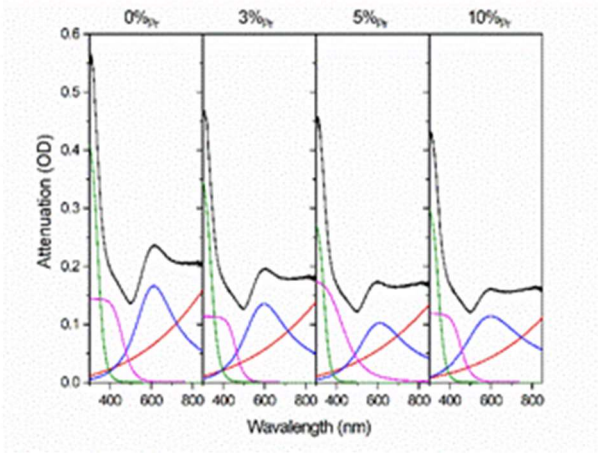

Figure S11: Spectral deconvolution of the SS UV-Vis, by use of two Lorentzian peaks for the LSPR, one Lorentzian for the CPO interband, and a switching function for the gold interband.[48,49]

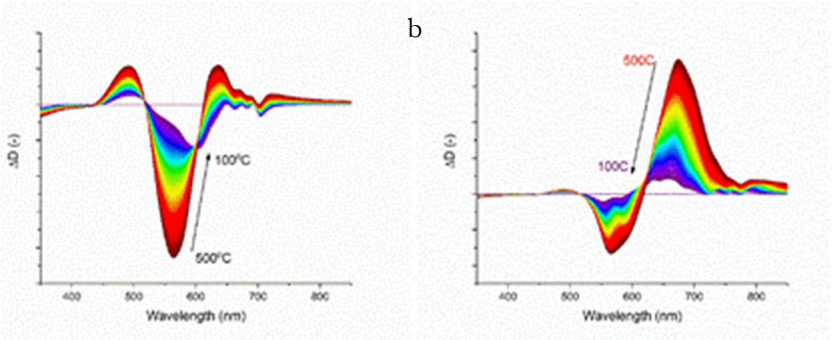

Figure S12: Calculated Mie scattering of gold nanoparticles (using the sample distribution) with the heating of a) only the gold, b) uniform heating of gold in a pure ceria matrix.

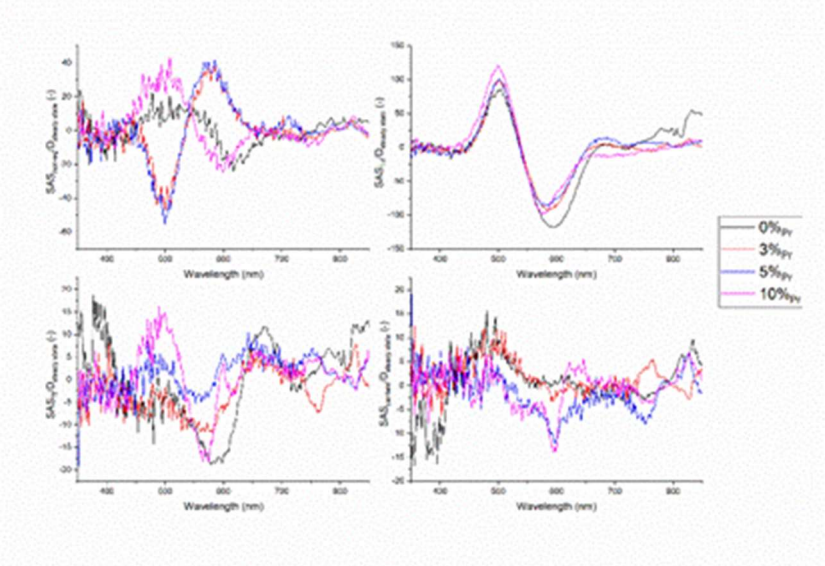

Figure S13: SAS spectra normalized by the steady state attenuation. Very little changes in the interpretation of the SAS, however the large difference between the samples in SAS_{Te} is largely reduced, signifying that the origin of that difference stems from the amount of light interaction, and not the relaxation pathway.

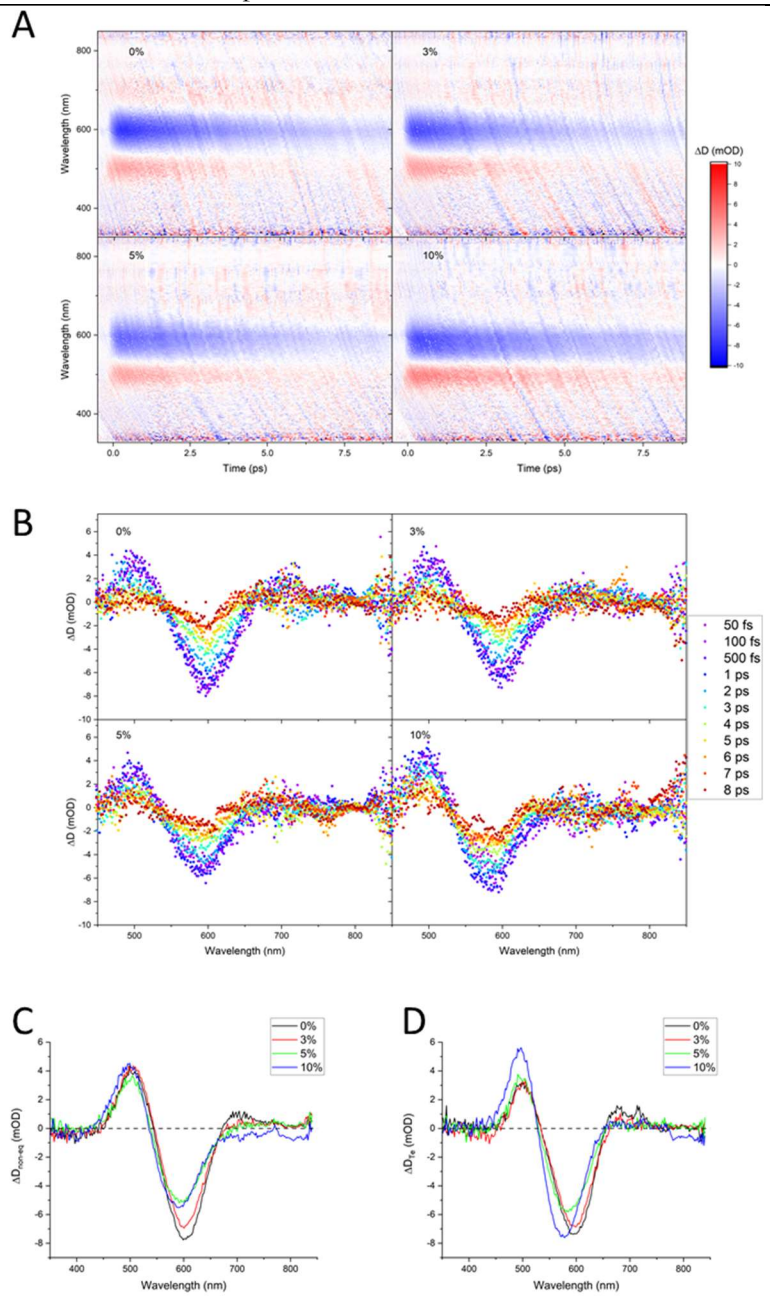

Figure S14: A) TA contour plot of the Au/CPO with 600 nm excitation, with smaller step sizes allowing for careful determination of the ingrowth behaviour. B) Spectra

of the same. C) the non-equilibrium component of the TA signal. D) T_e component of the TA signal. Noteworthy: while the 830 nm signal is not observed in the repeat, the PB band in the $10\%_{Pr}$ sample is retained.

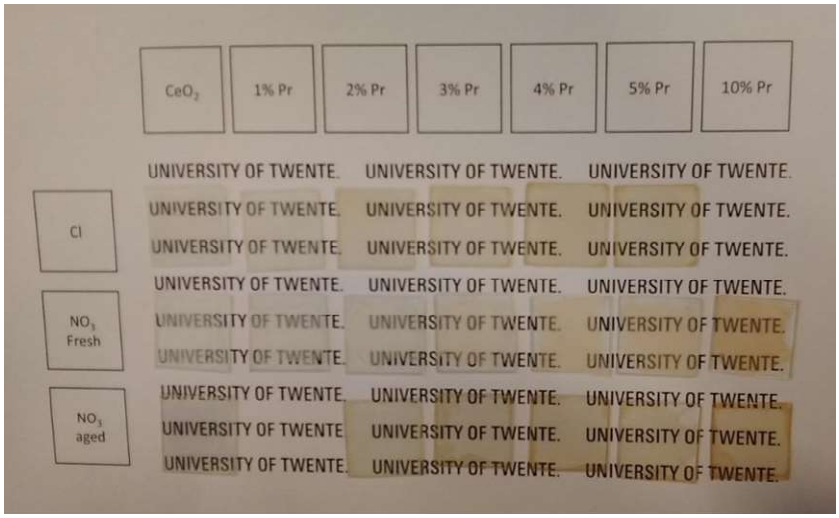

Figure S15: Effect of aging and concentration on thin films of CPO (produced with 0.3M metal nitrate salts). The method adapted from literature employed chloride salts; however, use of nitrate salts was desirable as nitrate is easily removed during calcination. It was found that aging the metal nitrate in a methanoic solution of citric acid produced high quality films, while a fresh solution produced more opaque, rough coatings.

Ultrafast photoinduced heat generation by plasmonic HfN nanoparticles[j]

There is great interest in the development of alternatives to noble metals for plasmonic nanostructures. Transition metal nitrides are promising due to their robust refractory properties. The photophysics of these nanostructures, particularly the hot carrier dynamics and photothermal response on ultrafast timescales, are not well understood, which limits their implementation in applications such as photothermal catalysis or solar thermophotovoltaics. In this study, the light-induced relaxation processes in water-dispersed HfN nanoparticles are elucidated by fs transient absorption, Lumerical FDTD and COMSOL Multiphysics simulations and temperature-dependent ellipsometry. We unequivocally demonstrate that HfN nanoparticles convert absorbed photons into heat within <100 fs; no signature of hot charge carriers is observed. Interestingly, under high photon energy or intense irradiation stimulated Raman scattering characteristic of oxynitride surface termination is observed. These findings suggest that transition metal nitrides could offer benefits over noble metals in the field of plasmonic photothermal catalysis.

[j] This work was a collaboration with Sven Askes (AMOLF), who synthesized and characterized the particles, and performed simulations; Erwin Zoeuthout (DIFFER) performed the temperature dependent ellipsometry.

Ultrafast photoinduced heat generation by plasmonic HfN nanoparticles

1 Introduction

Plasmonic nanostructures, especially those made from noble metals, attract widespread attention owing to their high and tunable optical cross section, light concentration effects and hot carrier generation.[1,2] This has led to significant interest in plasmonic nanostructures for photocatalysis, either through local heat generation or as a photosensitizer.[3,4] Materials in the family of plasmonic transition metal nitrides (e.g. TiN, HfN, NbN, WN) feature high thermo-mechanical robustness and recently have been proposed for applications requiring extreme operating conditions, such as photothermal catalysis or solar thermophotovoltaics.[5] These materials have high melting points and demonstrate high temperature durability, chemical stability, and corrosion resistance, while presenting an optical response similar to Au or Ag plasmonic nanostructures.[5,6] With a strong response in the visible range, high mechanical hardness, low material cost,[6–9] and outstanding performance in electrochemical reactions,[10,11] the photophysics of these materials requires further research. In the following we will briefly review the current level of understanding of the photophysics of noble metal plasmonic particles, followed by a discussion on transition metal nitride plasmonic nanoparticles.

Light absorption and heat generation by noble metal nanoparticles can be summarized as follows: first, the local surface plasmon resonance (LSPR) is excited, which lasts several fs and decays by non-radiative dephasing through Landau dampening (1 – 100 fs). This process generates hot carriers at regions with high optical absorption (hotspots), the hot carriers subsequently decay by electron-electron scattering (1 – 100 fs) followed by electron-phonon coupling (0.1 – 10 ps). Ultimately, phonons dissipate heat to the surroundings (1 – 10 ns).[4,12,13] There is increasing interest in hot carrier processes, chemical reactions induced by them, and determining whether the observed changes in chemical reactions are due to lattice heating or hot charge carriers.[14,15]

Since elementary chemical transformations typically occur on a 1 – 100 ps timescale,[16] it is essential to characterize the light-induced carrier dynamics and thermal relaxation of plasmonic systems that consist of non-noble metal materials. Recent studies have shown that in particular hafnium nitride (HfN) performs well at converting light into heat through thermo-plasmonic relaxation.[17,18] This efficient light-induced heating likely stems from a less negative real permittivity (ε') and a higher imaginary permittivity (ε") of HfN relative to noble metals, leading to a lossy plasmonic response accompanied by lower electric field magnification,[19–23] fast plasmonic dephasing, spectral broadening of the LSPR,[4] and, most importantly, high

optical absorption. Overall, these properties are highly attractive for plasmonic heat generation with broadband light sources, such as in photothermal catalysis or photothermal therapy.

Presently, the photodynamics of HfN are not well understood, with a discrepancy in the literature. On the one hand, experimental work on HfN thin films has ascribed a long-lived (ns) signal to the slow decay of hot carriers,[24–28] whereas on the other hand, theoretical work has predicted a maximum hot carrier lifetime of only 10 fs.[29] Furthermore, the understanding of TiN and ZrN thin-film photodynamics has shifted recently from long-lived carriers to the present understanding of very strong electron-phonon coupling with the use of fs spectroscopy.[29–33] Thus, further research is required to resolve this discrepancy and elucidate the hot carrier dynamics and photothermal temporal response of plasmonic HfN nanoparticles.

In this work, we investigate the photophysical relaxation processes in water-dispersed HfN nanoparticles using fs transient absorption (TA) spectroscopy. By combining the TA results with optical simulations and an advanced three-dimensional two-temperature model, it is unequivocally demonstrated that the photodynamics of HfN nanoparticles are characterized by an ultrashort hot carrier lifetime and concomitant ultrafast lattice heating. Furthermore, by using optical constants from temperature-dependent ellipsometry experiments we show that the observed transient spectral features could be faithfully reproduced by only implementing this thermal effect. Interestingly, under particular photoexcitation conditions a signature of stimulated Raman scattering at early times (~100 fs) is observed, indicative of a photochemical surface reaction. Finally, we given our experimental and numerical results, we hypothesize that the dominant mechanism for HfN in photochemical applications should be almost purely thermal (lattice heating), making it a useful system for mechanistic studies.

2 Results and Discussion

The HfN nanoparticles form a purple, transparent, colloidal suspension of well dispersed particles in water (Figure 1a), with a clear plasmonic UV-Vis absorption band centered at 555 nm and an inter-band transition in the UV region. The asymmetry of the plasmonic band is indicative of the effect of the size and shape distribution.[34] The x-ray diffraction pattern (Figure 1b) shows the narrow peaks of cubic rock-salt crystalline HfN[35], with a minor impurity of unreacted HfO_2

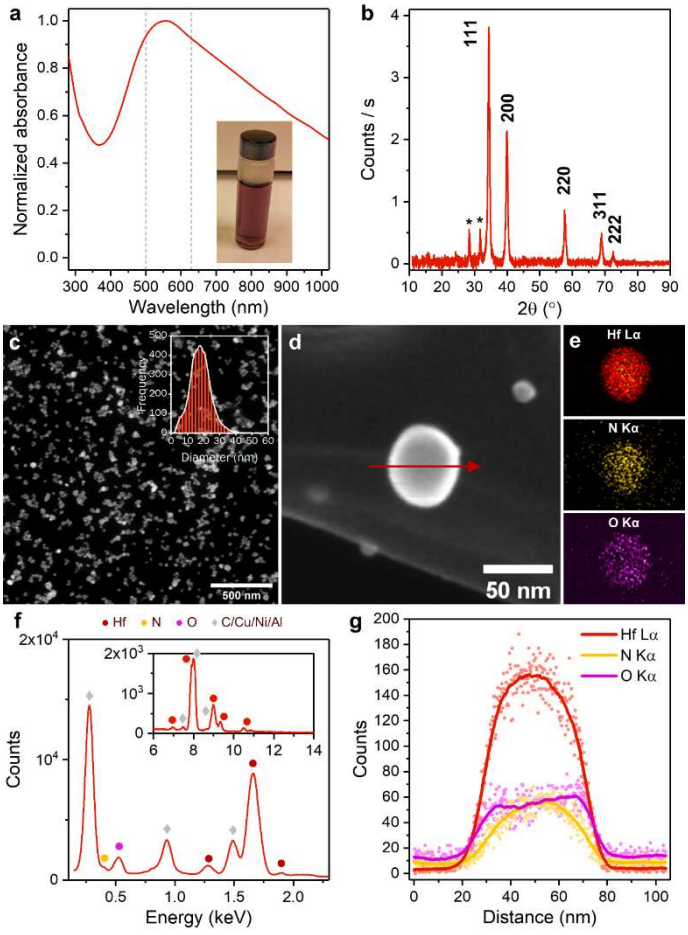

Figure 1. Physical and optical characterization of HfN nanoparticles. a) Normalized UV-Vis absorption spectrum with inset photograph of the nanoparticles in water. The photoexcitation wavelengths used in this work are indicated with dashed lines. b) X-ray diffraction pattern with indexed HfN peaks.[40] Asterisks (*) indicate HfO_2 peaks (COD card 400-1331). c-d) Scanning electron micrographs. Particle size distribution of multiple analyzed images shown as inset in panel c. e) Energy dispersive x-ray (EDX) analysis of the particle shown in panel d. f) EDX spectrum of the particle shown in panel d. Signals of the support grid and microscope indicated by grey diamonds. Inset shows the higher-energy region. g) EDX line scan of the particle in d, along the red arrow. Moving average lines are added to guide the eye. Note that the relative intensities of signals are not calibrated to reflect the atomic composition.

precursor. Since HfO_2 has no optical absorption in the visible range, no further purification is necessary.[36] Scanning electron microscopy (SEM) images show near-spherical particles with an average diameter of 18 nm (Figure 1c-d). Energy-dispersive x-ray spectroscopy (EDS) of single particles confirm the Hf and N constituents, and additionally show the signature of a self-passivating oxide or oxynitride shell around the particles (Figure 1e-g).[37–39] Overall, the HfN nanoparticles are of high quality and suitable for TA experiments.

Figure 2 shows the TA data of the HfN nanoparticles dispersed in water, recorded at 500 nm excitation (for data at 630 nm excitation, see Figure S1). We attribute the decrease in absorbance around 475 nm to attenuated LSPR absorption, while the positive signal $\lambda < 400$ nm is likely due to LSPR broadening.[41] The TA spectrum shape is constant at all time delays (Figure S2) showing little significant change in spectral shape in time; while the TA signal decays in several hundred ps. Changing the excitation wavelength from 500 nm to 630 nm shows no significant change in TA spectrum (Figure S3). At this point, it is important to realize that both light-induced changes in energy distribution of the charge carriers and lattice temperature contribute to the transient signals, with the electronic component typically being more pronounced than that arising from heat dissipation.[42] On the one hand, photoexcitation causes a change in energy distribution of the charge carriers, with less electrons at the Fermi level to contribute to the plasmon dipole, thereby attenuating and broadening the LSPR band. In a TA spectrum, this effect typically induces a loss of absorption around the LSPR wavelength (bleach) and gain in absorption at either side, which are typically referred to as "wings" (the lack of a positive wing at lower energies is attributed to the width of the HfN LSPR band, with the low energy wing being expected into the NIR).[41] On the other hand, the subsequent electron-electron scattering and electron-phonon coupling lead to thermal expansion of the lattice lowering the effective carrier concentration and metallicity (ε'), while the increasing phonon population and electron-phonon interactions result in higher losses (higher ε"). As a result, an elevated lattice temperature also produces a lower quality LSPR and broadens the absorption band, similar but not identical to electronic effects.[41–44] As the difference in relative intensities of electronic and thermal effects normally results in a multi-exponential decay in time,[41] and here only a single decay is observed; therefore, the observed spectral response cannot be unambiguously assigned to an electronic or thermal effect.

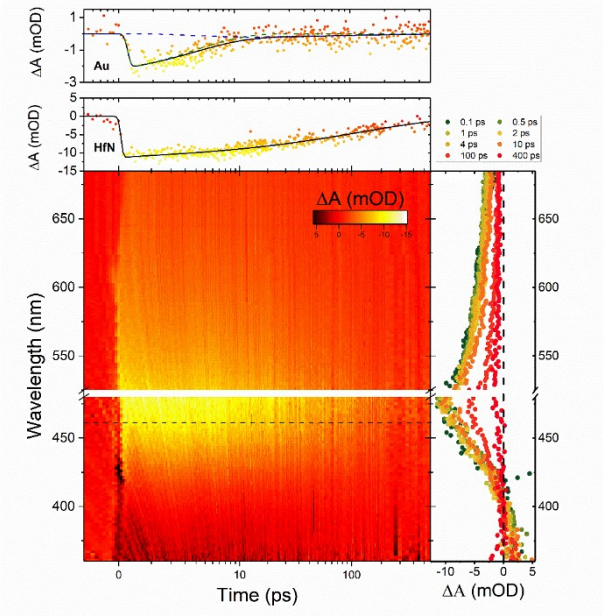

Figure 2. TA contour plot with $\lambda_{exc.}$ = 500 nm for HfN nanoparticles in water. Right: spectra at selected time delays. Top: time-trace of Au nanoparticles in water probed at 524 nm, with a two-component exponential fit (τ_1 = 4.6 ± 0.1 ps, τ_2 = 65 ± 4 ps). Middle: time-trace for HfN nanoparticles in water probed at 462 nm, with a stretched-exponential fit (Equation 1, see text).

When comparing the temporal response of HfN nanoparticles with Au nanoparticles as a well-studied benchmark, both dispersed in water (top panels Figure 2), a notable difference is evident. The TA decay of Au nanoparticles is well described by a two-component exponential decay (τ_1 = 4.6 ± 0.1 ps, τ_2 = 65 ± 4 ps, Figure S4a), for which the typical lifetime of hot electrons (τ_1) can be clearly distinguished[45] followed by thermal dissipation (τ_2). In contrast, the TA signal of the HfN nanoparticles decays in what appears to be a single process with no evidence of a two-component exponential decay. Since the observed decay roughly coincides with the time-regime of thermal dissipation in plasmonic systems (0.1 – 10 ns), we tentatively fit a stretched exponential function that is characteristic for this phenomenon[43] to the decay traces:

$$f(t) = Ae^{-(t/\tau)^{\beta}}\text{erf}\,(t/w)f(t) = Ae^{-(t/\tau)^{\beta}}\text{erf}\,(t/w) \quad \text{Equation 1}$$

where β modifies the rate of decay (reported as β ≈ 0.6-0.7 for 15 – 50 nm diameter spherical Au nanoparticles),[46] which is governed by the time constant τ, and the signal rise-time is modelled by an integrated Gaussian with width w, also known as an error function. While β is allowed to vary between 0.1 and 1 during the fitting, it converges to 0.5 ± 0.1 for both 500 nm and 630 nm excitation with excellent agreement at both short and long timescales. The decay time is found to be similar for the two photoexcitation wavelengths: $\tau_{500\text{ nm}}$ = 130 ± 10 ps, and $\tau_{630\text{ nm}}$ = 120 ± 20 ps. We have explored several other fitting functions to scrutinize the temporal decay as well. Fitting with a single-component exponential gives a discrepancy at longer time scales (Figure S5). A two-component exponential function affords a reasonable fit to the data, but both decay-associated spectra are virtually identical (Figure S6). This is also evident from the absence in spectral evolution in time (Figure 2), thus no transition from a hot electron regime to a thermal regime is observed. Overall, our TA data exclusively show signals of thermal dissipation in the HfN nanoparticles, with no sign of hot charge carrier decay, for which we present further evidence based on simulations below.

The normalized decay associated spectra (Figure S3) show little change with excitation wavelength (500 nm and 630 nm); interestingly, with the center wavelength for the bleach being some 80 nm blue-shifted from the center of the plasmonic band (in contrast to gold, where the bleach is centered on the plasmon band).[41] While there is normally a short-lived blue-shift in plasmonic particles after excitation owing to excited electrons,[47] this is not the case here as the blue-shift is retained throughout the observed time frame. Accordingly, this blue-shift most likely arises from the lattice temperature, which likely also causes a blue-shift in the plasmon resonance.[48]

The absence of a signature of hot carrier decay in the TA data strongly suggests that electron-phonon coupling occurs at the same timescale or faster than our temporal resolution of ~100 fs. To corroborate this implication, we have calculated the electron-phonon coupling constant (G in W/m^3.K) from literature data using Equation 2:[31,33,49]

$$G = \frac{3\gamma\lambda\langle\omega_2\rangle\rho}{\hbar\pi k_B M_W} \quad \text{Equation 2}$$

where γ is the Sommerfeld constant, λ is the Bardeen-Cooper-Schrieffer electron-phonon coupling constant, $\langle\omega_2\rangle$ is the second moment of the phonon spectrum, ρ is the material density, $\hbar$ is the reduced Planck's constant, k_B is the Boltzmann constant and M_W is the molar weight of HfN. Although $\langle\omega_2\rangle$ is not well known for HfN, it could be estimated from the Debye temperature θ_D. This results in calculated electron-phonon coupling constants of 1.4×10^{18} W/m^{3}K for HfN, and 2.8×10^{16} W/m^{3}K for Au (see Table S2, and associated text for more details).[31,50–54] Thus, the electron-phonon coupling in HfN is roughly 50 times stronger than in Au, which directly implies a significantly faster hot electron decay. Accordingly, with a hot electron-phonon coupling time $\tau_1 = 4.6 \pm 0.1$ ps for Au nanoparticles, the estimated time constant for HfN is on the order of 100 fs, close to the instrumental temporal resolution. As a result, hot electron decay is not resolved, and the TA decay almost certainly originates from thermal dissipation only.

To further explore the photophysical dynamics of the HfN nanoparticles, finite difference time domain (FDTD) simulations have been combined with an advanced 3D two-temperature model to simulate the energy flow in the system, fully accounting for thermal conduction of both electrons and phonons (see SI for details). These simulations, based on thin film optical constants of HfN[34] and Au, show that 20 nm diameter HfN and Au nanoparticles have similar dipole electric field enhancements (Figure 3a), with a higher internal electric field for HfN nanoparticles. We additionally consider the case where the HfN particle is covered with a thin 1 nm HfO_2 shell, which red-shifts the LSPR slightly. Since the absorbed power is proportional to the product of the square of the electric field and the imaginary permittivity, both HfN nanoparticles have a larger absorption cross section than an Au nanoparticle (Figure 3b). The spatial absorbed power map is used as laser heating term (q(x,y,z,t)) in the two-temperature model. This model is governed by Equations 3 and 4:

$$C_e(T_e)\frac{\partial T_e}{\partial t} = \nabla[\kappa_e(T_e)\,\nabla T_e] - G(T_e - T_l) + q(x,y,z,t) \qquad \text{Equation 3}$$

$$C_l(T_l)\frac{\partial T_l}{\partial t} = \nabla[\kappa_l(T_l)\,\nabla T_l] + G(T_e - T_l) \qquad \text{Equation 4}$$

where subscripts e and l distinguish between electronic and lattice terms, T is the temperature (in K), C(T) is the temperature-dependent volumetric heat capacity (in W/m^3.K), κ(T) is the temperature-dependent thermal conductivity (in W/m.K),

and G is the electron-phonon coupling constant that facilitates heat exchange between T_e and T_l. Although G is temperature-dependent as well,[55] from theoretical data on TiN and Au we estimate it to be roughly constant in the temperature range in this work.[56] These partial differential equations are solved with a finite element method in COMSOL Multiphysics, from which the spatial T_e and T_l time-profiles are extracted (Figure 3c-i).

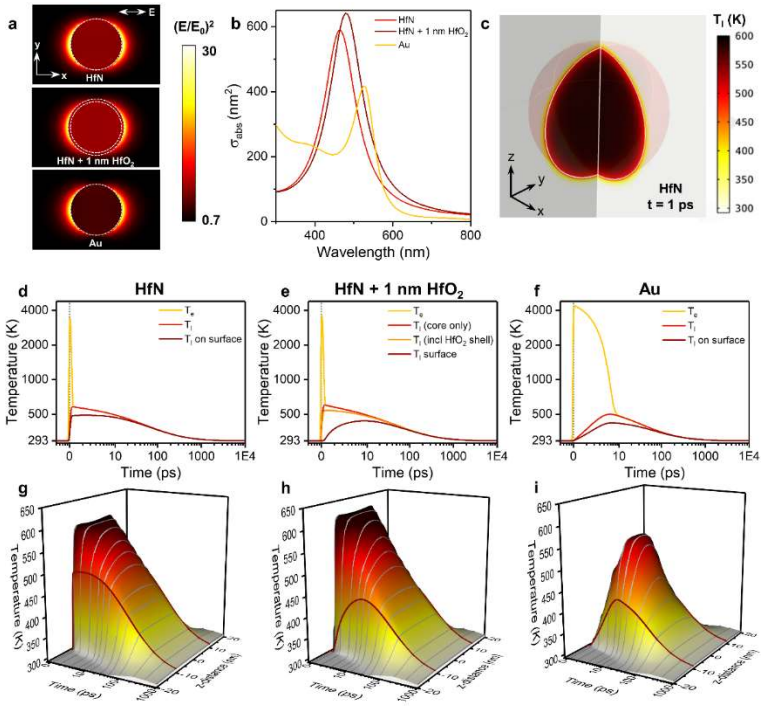

Figure 3. Time-dependent simulation results modelling the evolution and dissipation of heat from 20 nm diameter HfN and Au nanoparticles upon 50 fs photoexcitation (6.4 W/cm^2). a-b) Electric field intensity cross sections (a) and absorption cross section spectra (b) simulated by Lumerical FDTD. Modelling of heat dissipation: a render of the heat distribution 1 ps after a pulse illuminates a HfN particle (c). d-f) Average temperature of the electrons (T_e) and lattice (T_l) in time for a HfN nanoparticle without (d) and with a 1 nm oxide layer (e), and for an Au nanoparticle (f). g-i) Temporal lattice temperature profiles along the z-axis of the spheres. The surface temperature is shown as dark-red lines. For panels d-i, the heat pulse is centered at 0 ps. An animation of the three-dimensional heat dissipation is given in Supporting Video 1.

The results of the simulations for both HfN and Au nanoparticles (Figure 3 and Supporting Video 1) show the evolution of the electron and lattice temperatures in time following photoexcitation. Initially the electron temperature rises, followed by a relaxation and transfer of energy to the lattice resulting in the lattice temperature increasing, which finally equilibrates with the surrounding water (Figure 3c-i). Both HfN and Au nanoparticles show comparable electron temperatures after photoexcitation (centered at 1 ps). However, whereas in Au nanoparticles the hot electrons are fully thermalized after 10 ps, this process occurs much more rapidly in HfN, in about 250 fs. Simultaneously, the HfN lattice heats up almost uniformly to ~600 K with the onset of a large temperature-gradient across the metal-water interface (Figure 3d/g). Meanwhile, the Au nanoparticle reaches a lower temperature due to the lower absorbed power. The inclusion of the thermally isolating HfO_2 thin shell ($\varkappa_{HfO2} \approx 1.1$ W/m.K) changes the surface temperature drastically (Figure 3e/h), but it still remains higher than that of the Au nanoparticle throughout the entire time window. Note, moreover, that in practice the shell will be an oxynitride material (HfO_xN_y, or heavily N-doped HfO_2) and will be expected to have a higher thermal conductivity than pristine HfO_2,[57] that is the presented data can be considered as a lower-limit case for the surface temperature response. When examining the thermal dissipation after the electron-phonon coupling regime (>10 ps), the HfN nanoparticle dissipates the heat while maintaining a fairly uniform internal heat profile, while in the Au nanoparticle there is a larger heat gradient between core and surface on the 10 – 100 ps timescale (Figure 3f/i). This difference can be interpreted as the result of the lower heat capacity of Au than HfN (Figure S7) and high gold/water interfacial thermal conductivity,[58,59] causing the surface to cool down quicker when in contact with H_2O. Eventually, each examined nanoparticle is fully cooled down to ambient temperature after several ns. Crucially, just as for the TA data, the simulated thermal dissipation can only be satisfactorily fitted using a stretched exponential decay (Equation 1, Figure S10), and not with a single or double exponential function. Additionally, the simulated data for Au nanoparticles is in excellent agreement with both literature and our TA results (Figure 2). the calculated e-ph regime is on the order of 10 ps and thermal dissipation occurs over 100's ps,[41] comparably our TA result in $\tau_{e\text{-}ph} = 4.6 \pm 0.1$ ps and $\tau_{ph\text{-}ph} = 65 \pm 4$ ps. Accordingly, the simulations are accurate representations of the Au particle relaxation, and validate the simulations for HfN. Ultimately we conclude that the fs TA signal is exclusively due to thermal effects without electronic contribution.

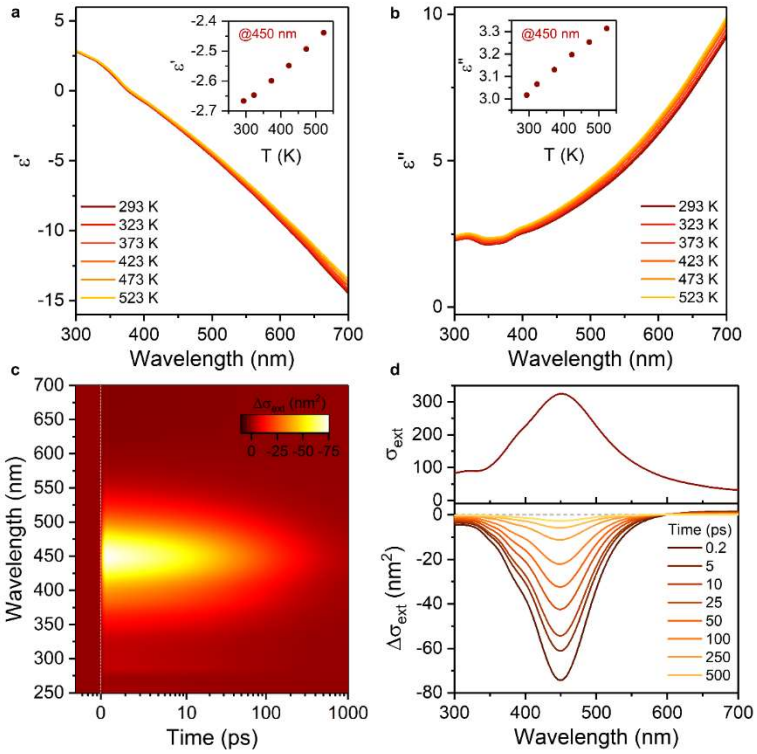

Figure 4. Temperature-dependent ellipsometry and simulated TA data. a-b) Real (a) and imaginary (b) permittivity of a 160 nm thin film HfN at 50 K intervals, up to 523 K. The insets show the near-linear response of each part as a function of temperature at λ = 450 nm. c-d) Simulated TA contour plot and spectra at selected time delays, generated from Mie Theory (Equation 5).

Next, to explain the spectral shape of the TA data we have measured the influence of temperature on the optical constants by temperature-dependent ellipsometry. A high quality thin HfN[34] film was deposited on Si, protected from heat-induced oxidation by a 10 nm film of atomic-layer deposited (ALD) Al_2O_3, and the complex reflection has been measured on an ellipsometer fitted with a heating stage. The Al_2O_3 layer successfully protects the HfN from oxidizing and roughening during heating, with the retrieved spectra being unchanged before and after the cycle (Figure S13). This is not the case for unprotected HfN (Figure S14). The model-extracted optical constants of the HfN thin film from room temperature to 523 K are shown in Figure 4a-b. At elevated temperature, HfN has a less negative real permittivity and a higher imaginary permittivity, with changes being near-linearly

dependent on temperature. At 450 nm, heating the sample to 523 K results in a 10% difference in both parameters. As recently explained in literature for TiN thin films,[60,61] these results can be interpreted by two physical effects upon heating. First, the lattice expands, which reduces the carrier concentration and the screened plasma frequency (where ε' = 0). Secondly, an elevated temperature increases the phonon population, which leads to an increase in phonon scattering and increased attenuation by the bulk material. Finally, we used the temperature-dependent optical constants to estimate the attenuation cross section spectrum (in nm²) from Mie Theory at each temperature during the simulated temperature decay of the HfN nanoparticle by Equation 5:[62]

$$\sigma_D(T_l,\lambda) = \frac{24\pi^2 r^3 {\varepsilon_m}^{\frac{3}{2}}}{\lambda} \times \frac{\varepsilon''(T_l,\lambda)}{(\varepsilon'(T_l,\lambda)+2\varepsilon_m)^2+\varepsilon''(T_l,\lambda)^2} \qquad \text{Equation 5}$$

where r is the particle radius (in nm), and ε_m is the permittivity of the aqueous medium (1.729). By subtracting the absorption cross section spectrum at 293 K, a fully simulated TA data set has been generated (Figure 4c-d). Due to the changes in optical constants, the LSPR band is bleached and broadened when the material is heated, with a change of about 25% when the particle reaches 600 K. The attenuated absorption is centered at the LSPR center wavelength at room temperature. We attribute small differences between experimental and simulated TA diagrams (spectral broadening, central LSPR wavelength,) to the polydispersity of the experimental particles and the inherent differences between sputter-coated and solid-state synthesized HfN. Taken altogether, these data show that an elevated lattice temperature can fully account for the experimentally observed TA behavior of HfN nanoparticles.

The conclusions of this work are in strong contradiction with some recent literature that concluded hot carriers are responsible for the long transient signal observed in HfN thin films.[24–28] However, their analysis does not account for heat generation and dissipation, which is known to be significant in other transition metal nitrides.[32,54,63] It is clear from our analysis that heat has a profound influence on the transient optical response of HfN nanoparticles. Further, they concluded that a phonon-bottleneck is responsible for preventing phonon decay and retaining a hot electron bath,[26] while not accounting for a defect-rich material which, much like our material, would not effectively support one. Conversely, the conclusion of ultrafast heat generation is in line with both observations and theoretical work for similar group-4 metal nitrides (TiN and ZrN).[9,31,32,61] Conclusively, given a real-world

defect-rich material, we are confident that the origin of long-lived TA signals stem from thermal dissipation.

As our findings reveal an ultrashort hot charge carrier lifetime in HfN nanoparticles, with little to no opportunity to harvest thermalized carriers, the question is whether HfN's hot carriers can play a role in plasmonic photochemistry. On the one hand, not yet thermalized "ballistic" hot charge carriers could play an important role in photochemical enhancements observed in literature.[64] However, ballistic hot electrons in HfN have been calculated to have a shorter lifetime than in Au,[29] making it unlikely they can be harvested with respectable efficiency. The same likely applies to ballistic hot holes, although these have not yet been explored.[65] On the other hand, thermalized electrons can be harvested as well, albeit with lower energy than ballistic ones.[4] However, when transforming the simulated electronic temperature from Figure 3d to a thermalized Fermi-Dirac distribution (Figure S12), the available thermalized electron energy in time is strikingly low for HfN, compared to Au: only during the laser pulse do the hot electrons and holes exceed 0.5 eV above and below the Fermi level, respectively. Conclusively, it is unlikely that HfN nanoparticles will prove to be a good hot carrier photocatalyst, but instead may be an excellent thermo-plasmonic material in which hot carrier effects are nearly abolished – as there has been much recent debate on disambiguating the role that hot carriers and local heat generation have in plasmon-driven processes.[14] In that respect, HfN is the most attractive material of the transition metal nitride family, as it combines the second-highest quality visible-range plasmonic character,[66] next to ZrN, with the fastest heating: the electron-phonon coupling of HfN (1.4×10^{18} $W/m^3.K$) is higher than that of TiN or ZrN ($0.8 – 1.0 \times 10^{18}$ and 1.0×10^{18} $W/m^3.K$, respectively)[32]. The ultrafast heating could be exploited in a number of applications, such as pulsed photothermal therapy and catalysis, photo-acoustic imaging, fast thermo-electronics, thermophotovoltaics, and optical nanofabrication with sub-wavelength resolution.

While electron-phonon coupling is not observed in TA, likely since it occurs within the instrumental response time, an interesting phenomenon is observed at early times (Figure 5). HfN nanoparticle suspensions exposed to high energy photons (500 nm) display a narrow photoinduced absorption band around 416 nm which only lasts for ~100 fs. With 630 nm excitation the phenomenon is not seen, unless the sample has previously been irradiated with 500 nm pulses, or the sample is left stationary instead of moved and exposed to high intensity 630 nm pulses. This is accompanied with localized permanent bleaching of the sample, confirming that this is not the missing hot carrier component. The position of the phenomenon with 630 nm excitation red-shifts and is found to be consistently 0.4 ± 0.1 eV above the

pump photon energy. Its presence always follows exposure to either high intensity or high photon energy pulses. This indicates that there is some long-lasting change to the HfN nanoparticles and questions their long-term stability under high-demanding operating conditions, but does not explain what is being observed.

There are several coherent Raman phenomena which could cause a signal in ultrafast TA experiments.[67–69] Given that HfN has a high third order susceptibility ($\chi(3)$) like other group-4 nitrides,[70,71] it may display non-linear optical processes including inverse Raman scattering, or stimulated Raman scattering. In the case of stimulated Raman scattering, a loss in transmission (i.e. higher absorbance) blue-shifted from the pump accompanying a gain in transmission (i.e. decrease in absorbance) red-shifted from the pump can be expected.[69] A short-lived photoinduced absorbance blue-shifted from the pump is clearly visible around 416 nm. Scrutinizing 0.4 ± 0.1 eV below the pump photon energy in Figure 5 does give some indication that there may be a weak short-lived decrease in absorbance ~610 nm. However, as it is followed by a photo-induced bleach of the LSPR developing within the instrumental response time, it is difficult to determine if there is indeed such short-lived stimulated Raman signal, or a slight miscorrection of the experimental chirp.

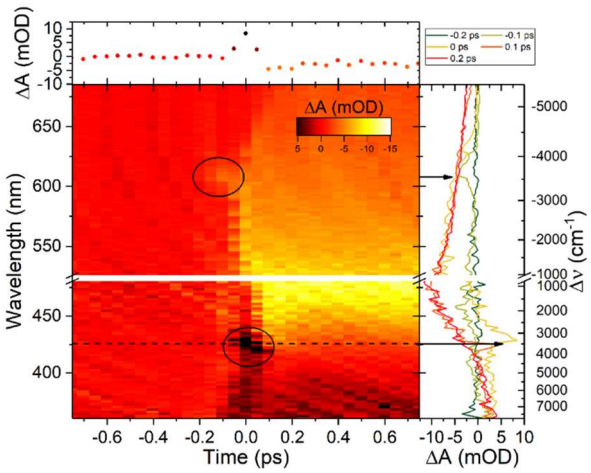

Figure 5. TA contour plot of the early-time phenomenon observed during excitation at 500 nm with time trace at 416 nm, and spectra at time delays of -0.2 ps - 0.2 ps, circles and arrows highlight the regions with ultrafast signals likely caused by stimulated Raman scattering.

If this phenomenon is indeed stimulated Raman scattering, then the 0.4 ± 0.1 eV shift would give an indication of the surface termination. As such, it would be more effective to note that the shift is 3500 ± 800 cm^{-1}, which corresponds roughly to both OH and NH vibrations. Combining this with the observation of a permanent bleach with intense and prolonged 630 nm pulsed irradiation indicates that the HfN is being oxidized and forming hydrated oxide/nitride. This suggests that HfN nanoparticles may not be as chemically stable in high-demanding aqueous conditions as generally advocated and use as a thermo-plasmonic source may require surface passivation if both longevity and intense or energetic light is used. Indeed, recently a method for coating TiN nanoparticles with a shell of silicon oxynitride has been presented, which greatly enhanced the thermal stability of the particles up to 900 °C.[38] In our own temperature-dependent ellipsometry measurements we applied Al_2O_3 as thin protection layer using a conformal ALD process, which altogether prevented further surface oxidation when heated to 523 K. Furthermore, since Al_2O_3 is an excellent thermal conductor, the thermo-plasmonic response would remain largely unaffected.

3 Conclusions

The photophysical and -chemical relaxation pathways in water-dispersed HfN nanoparticles have been studied through fs transient absorption spectroscopy, paired with Lumerical FDTD and COMSOL Multiphysics simulations supported by temperature-dependent ellipsometry. The HfN nanoparticles have been compared to Au nanoparticles, which have well-understood photodynamical regimes, demonstrating the differences, and to validate simulation results. The transient absorption data and simulations are in excellent agreement. We unequivocally demonstrate that HfN nanoparticles convert absorbed photons into heat within <100 fs following photoexcitation; no signature of hot carriers is observed. These results bridge the discrepancy between previous theoretical and experimental work, and demonstrate that in HfN nanoparticles for times beyond the ~100 fs regime after photoexcitation only heat dissipation takes place. This means that while HfN nanoparticles are not good candidates for hot-carrier induced photochemical reactions, they could be ideal for plasmonic photothermal reactions and to help determine the underlying mechanism in plasmonic photochemical reactions. For the application of HfN nanoparticles as a thermo-plasmonic source in aqueous conditions, the formation of a $HfN_xO_yH_z$ surface layer, which likely explains stimulated Raman signals observed here, should be considered and prevented.

4 Methods

4.1 General techniques

Scanning electron microscopy (SEM) was performed on a FEI Verios 460 at 5 kV acceleration voltage and 100 pA beam current. Energy dispersive X-ray spectrometry (EDS) measurements were performed with an Oxford Instruments device with a beam acceleration voltage of 20 kV and current of 0.8 nA, with particles adhered to a TEM grid (Cu-mesh with formvar/carbon). X-ray diffraction (XRD) patterns were measured with a Bruker D2 Phaser with Cu K_α radiation (λ = 1.5406 Å). Atomic layer deposition (ALD) of alumina was performed with a previously published procedure at 250 °C,[72] resulting in a thickness of exactly 10.0 nm. All data and images were further processed using Microsoft Excel, Origin 2017, and ImageJ 2.0 software.

4.2 HfN nanoparticle synthesis

HfN nanoparticles were synthesized according to an adjusted literature method from HfO_2 using Mg_3N_2 at 1000 °C and purified using an acidic work-up.[40] In brief, 300 mg HfO_2 nanoparticles (61-80 nm average particle size, US Research Nanomaterials, Inc.) and 432 mg Mg_3N_2 (325 mesh, Sigma Aldrich) were ground together using pestle and mortar for 5 min. in a glovebox. The mixture was transferred to an alumina crucible, placed in a quartz tube, and transferred to a tube oven. The tube was flushed with 100 sccm Ar for 10 min. and then kept at 50 sccm during subsequent heating. The oven was ramped to 1000 °C at 25 °C/min. and kept for 12 h before allowing the oven to cool down to room temperature. The resulting black powder was added to 60 mL distilled water and transferred to a 200 mL beaker. A clear hiss of escaping gas indicated that there was still active Mg_3N_2 powder in the mixture. Then, 75 mL 1 M HCl was added and the beaker was stirred for 1 h. The dark suspension was centrifuged at 3300 rpm for 15 min., after which the nearly colorless supernatant was decanted and discarded. The pellet was dispersed in 13 mL distilled water by use of vortex and sonication, and centrifuged again at 3300 rpm for 15 min. The deeply purple-colored supernatant was carefully collected (product batch #1), and the pellet was once more dispersed in 13 mL distilled water and centrifuged at 3300 rpm for 15 min. The supernatant was collected (product batch #2) and was added to product batch #1; this combined nanoparticle dispersion was used without further purification. The solution typically remained stable for days to weeks before noticeable precipitation occurred.

4.3 Gold nanoparticle synthesis

Gold nanoparticles were synthesized using the established Turkevich method:[73,74] 50 mL of 38.8 mM sodium citrate (Sigma, 99%) was added to 500 mL of boiling 1 mM $HAuCl_4$ (Sigma, 99.995%) and allowed to boil for 15 minutes before

being cooled. The yellow $HAuCl_4$ became transparent and then progressed to a deep red color. The particles were diluted in MiliQ water to have an attenuation of approximately 0.3 OD/mm and used without further treatment. A UV-Vis spectrum of the Au nanoparticle solution is shown in Figure S4b.

4.4 Reactive sputter coating of HfN

A Flexture reactive sputter coating system (Polyteknik AS, Denmark) was used to deposit HfN from a pure Hf target in a nitrogen/argon atmosphere (35.3 sccm Ar and 0.7 sccm N_2) on Si substrates. The base pressure was 8×10^{-8} mbar. The target was cleaned for at least 2 min. before deposition. The substrate was rotated at 4 rpm during deposition. Radio frequency (RF) magnetron sputtering with 150 W power at a pressure of 2.2×10^{-3} mbar resulted in a typical deposition rate of 8 nm/min.

4.5 Transient absorption spectroscopy

Femtosecond transient absorption experiments were performed using a home-built setup. The initial 800 nm pulses (FWHM 35 ± 1 fs) were produced by a Ti:Sapphire amplifier (Coherent Legend) operating at 5 kHz repetition rate. The output was split into two beams using a 90:10 beam splitter. The pump beam was generated by sending the major part of the 800 nm beam into an optical parametric amplifier (Coherent, Opera), producing pulses with tunable center wavelength and a pulse duration of ca. 50 fs FWHM. The differential absorbance between pump on and off was obtained by chopping the pump beam at 2.5 kHz. The pump was further attenuated using a neutral density filter. The white light continuum probe was produced through supercontinuum generation by guiding the remaining part of the 800 nm beam through a mechanical delay stage, variable neutral density filter wheel and focusing into a CaF_2 crystal (Newlight Photonics, 3 mm thickness, 001-cut, uncoated, the crystal was continuously moved to prevent damage). The remaining 800 nm light in the probe beam was removed using two IR neutral density filters. The polarization of the pump and probe were set to 54.7° (magic angle) to avoid anisotropy effects.[75,76] The pump was focused to a spot of ca. 250 μm diameter, significantly larger than the focused probe spot (ca. 100 μm diameter) and it is thus reasonable to assume that we probe a homogeneously photoexcited sample. Detection of the signal was achieved using a 15 cm spectrograph coupled to a 256-pixel diode array detector. Samples were mounted on a stage which constantly moved both horizontally and vertically to prevent irreversible light-induced changes. The time resolution was determined to be 100 – 150 fs, and the TA signal decay was verified to not be caused by persistent effects. The pump power was kept relatively low (~5 x 10^{14} photons/(cm^2 pulse)) and confirmed to be in the linear regime. The UV-Vis extinction of the samples was

verified to be identical before and after experiments to ensure that no significant permanent bleaching occurred (except in extreme cases when verifying the stimulated Raman scattering signal). Data analysis was performed using Matlab for chirp correction and stretched exponential fitting, and Glotaran[77] for one and two-component exponential fitting.

4.6 Temperature-dependent ellipsometry

Temperature-dependent ellipsometry was performed on a J.A. Woollam variable angle spectrometric ellipsometer (VASE) fitted with a copper heating stage. Reported temperatures correspond to the temperature of the heating stage. Samples were allowed to thermally stabilize at each temperature for 20 min. before ellipsometric measurement at 6 different angles (50-75° with 5° intervals). The optical constants for alumina-covered HfN were retrieved using WVASE32 and CompleteEASE software by isolating the HfN optical constants from the alumina contribution. The alumina contribution was individually measured on alumina covered Si from the same ALD batch process.

4.7 Optical and heat transfer modelling

A detailed account of the modelling is provided in the supporting information. Briefly, Lumerical FDTD was used to determine the optical absorption cross sections of HfN and Au nanoparticles and their three-dimensional absorbed power maps. COMSOL Multiphysics 5.1 was used to solve the heat transfer equations in space and time.

5 References

16. (1) Willets, K. A.; Van Duyne, R. P. Localized Surface Plasmon Resonance Spectroscopy and Sensing. *Annu. Rev. Phys. Chem.* **2007**, *58* (1), 267–297.
17. (2) Mayer, K. M.; Hafner, J. H. Localized Surface Plasmon Resonance Sensors. *Chem. Rev.* **2011**, *111* (6), 3828–3857.
18. (3) Halas, N. J. Spiers Memorial Lecture: Introductory Lecture: Hot-Electron Science and Microscopic Processes in Plasmonics and Catalysis. *Faraday Discuss.* **2019**, *214*, 13–33.
19. (4) Brongersma, M. L.; Halas, N. J.; Nordlander, P. Plasmon-Induced Hot Carrier Science and Technology. *Nat. Nanotechnol.* **2015**, *10* (1), 25–34.
20. (5) Guler, U.; Boltasseva, A.; Shalaev, V. M. Refractory Plasmonics. *Science* **2014**, *344* (6181), 263–264.
21. (6) Naik, G. V; Shalaev, V. M.; Boltasseva, A. Alternative Plasmonic Materials : Beyond Gold and Silver. *Adv. Mater.* **2013**, *25*, 3264–3294.
22. (7) Kim, S. J.; Thomann, I.; Park, J.; Kang, J.-H.; Vasudev, A. P.; Brongersma, M. L. Light Trapping for Solar Fuel Generation with Mie Resonances. *Nano Lett.* **2014**, *14* (3), 1446–1452.

23. (8) Goris, B.; De Backer, A.; Van Aert, S.; Gómez-Graña, S.; Liz-Marzán, L. M.; Van Tendeloo, G.; Bals, S. Three-Dimensional Elemental Mapping at the Atomic Scale in Bimetallic Nanocrystals. *Nano Lett.* **2013**, *13* (9), 4236–4241.
24. (9) Guler, U.; Boltasseva, A.; Shalaev, V. M. Refactory Plasmonics. *Science* **2014**, *344*, 263–264..
25. (10) Defillippi, C.; Shinde, D. V.; Dang, Z.; Manna, L.; Hardacre, C.; Greer, A. J.; D'Agostino, C.; Giordano, C. HfN Nanoparticles: An Unexplored Catalyst for the Electrocatalytic Oxygen Evolution Reaction. *Angew. Chemie Int. Ed.* **2019**, *58* (43), 15464–15470.
26. (11) Yuan, Y.; Wang, J.; Adimi, S.; Shen, H.; Thomas, T.; Ma, R.; Attfield, J. P.; Yang, M. Zirconium Nitride Catalysts Surpass Platinum for Oxygen Reduction. *Nat. Mater.* **2020**, *19* (3), 282–286.
27. (12) Zhang, Y.; He, S.; Guo, W.; Hu, Y.; Huang, J.; Mulcahy, J. R.; Wei, W. D. Surface-Plasmon-Driven Hot Electron Photochemistry. *Chem. Rev.* **2018**, *118*, 2927–2954.
28. (13) Hartland, G. V; Besteiro, L. V.; Johns, P.; Govorov, A. O. What's so Hot about Electrons in Metal Nanoparticles? *ACS Energy Lett.* **2017**, *2* (7), 1641–1653.
29. (14) Baffou, G.; Bordacchini, I.; Baldi, A. Simple Experimental Procedures to Distinguish Photothermal from Hot-Carrier Processes in Plasmonics. *Light Sci. Appl.* **2020**, *9* (108).
30. (15) Mascaretti, L.; Naldoni, A. Hot Electron and Thermal Effects in Plasmonic Photocatalysis Hot Electron and Thermal Effects in Plasmonic Photocatalysis. *J. Appl. Phys.* **2020**, *041101*.
31. (16) Khundkar, L. R.; Zewail, A. H. Ultrafast Molecular Reaction Dynamics in Real-Time: Progress Over a Decade. *Annu. Rev. Phys. Chem.* **1990**, *41* (1), 15–60.
32. (17) Traver, E.; Karaballi, R. A.; Monfared, Y. E.; Daurie, H.; Gagnon, G. A.; Dasog, mita. TiN, ZrN, and HfN Nanoparticles on Nanoporous Aluminum Oxide Membranes for Solar-Driven Water Evaporation and Desalination. *ACS Appl. Nano Mater.* 2020, 3, 3, 2787–2794.
33. (18) Karaballi, R. A.; Esfahani Monfared, Y.; Dasog, M. Photothermal Transduction Efficiencies of Plasmonic Group 4 Metal Nitride Nanocrystals. *Langmuir* **2020**, *36* (18), 5058–5064.
34. (19) Chen, J.; Wang, X.; Tang, F.; Ye, X.; Yang, L.; Zhang, Y. Results in Physics Substrates for Surface-Enhanced Raman Spectroscopy Based on TiN Plasmonic Antennas and Waveguide Platforms. *Results Phys.* **2020**, *16*, 102867.
35. (20) Zhao, F.; Xue, X.; Fu, W.; Liu, Y.; Ling, Y.; Zhang, Z. TiN Nanorods as Effective Substrate for Surface-Enhanced Raman Scattering. *J. Phys. Chem. C* 2019, 123, 48, 29353–29359.
36. (21) Wu, M.; Wei, H.; Wei, Y.; Yao, A.; Bu, J.; Lin, J.; Dong, Z.; Chen, Y.; Cui, Y.; Wu, Z. Vibrational Spectroscopy SERS Properties of TiN Nanotube Arrays Prepared via Reduction Nitridation of TiO2 Nanotube Arrays Derived from Anodic Oxidation Method. *Vib. Spectrosc.* **2018**, *95*, 32–37.
37. (22) Haynes, C. L.; Duyne, R. P. Van. Plasmon-Sampled Surface-Enhanced Raman Excitation Spectroscopy. **2003**, 7426–7433.

38. (23) Le Ru, E. C.; Etchegoin, P. G. Rigorous Justification of the |E|4 Enhancement Factor in Surface Enhanced Raman Spectroscopy. *Chem. Phys. Lett.* **2006**, *423*, 63–66.
39. (24) Xiaoming Wen; Chung, S.; Gupta, N.; Hongze Xia; Yu Feng; Shrestha, S.; Shujuan Huang; Kee, T. W.; Harad, T.; Conibeer, G. Ultrafast Transient Absorption Study of Hot Carrier Dynamics in Hafnium Nitride and Zirconium Nitride. In *2015 IEEE 42nd Photovoltaic Specialist Conference (PVSC)*; IEEE, 2015; pp 1–4.
40. (25) Chung, S.; Wen, X.; Huang, S.; Gupta, N.; Conibeer, G.; Shrestha, S.; Harada, T.; Kee, T. W. Nanosecond Long Excited State Lifetimes Observed in Hafnium Nitride. *Sol. Energy Mater. Sol. Cells* **2017**, *169* (March), 13–18.
41. (26) Chung, S.; Shrestha, S.; Wen, X.; Feng, Y.; Gupta, N.; Hongzy, X.; Ya, P.; Tang, J.; Conibeer, G. Hafnium Nitride for Hot Carrier Solar Cells. *Sol. Energy Mater. Sol. Cells* **2016**, *144*, 781–786.
42. (27) Shrestha, S.; Chung, S.; Liao, Y.; Wang, P.; Cao, W.; Wen, X.; Gupta, N.; Conibeer, G. Potential of HfN , ZrN , and TiH as Hot Carrier Absorber and Al_2O_3/Ge Quantum Well/Al_2O_3 and Al_2O_3/PbS Quantum Dots/Al_2O_3 as Energy Selective Contacts. *Jpn. J. Appl. Phys.* **2017**, *56* (852), 08MA03.
43. (28) Xia, H.; Wen, X.; Feng, Y.; Patterson, R.; Chung, S.; Gupta, N.; Shrestha, S.; Conibeer, G. Hot Carrier Dynamics in HfN and ZrN Measured by Transient Absorption Spectroscopy. *Sol. Energy Mater. Sol. Cells* **2016**, *150*, 51–56.
44. (29) Habib, A.; Florio, F.; Sundararaman, R. Hot Carrier Dynamics in Plasmonic Transition Metal Nitrides. *J. Opt.* **2018**, *20* (6), 064001.
45. (30) Sato, R.; Ishii, S.; Nagao, T.; Naito, M.; Takeda, Y. Broadband Plasmon Resonance Enhanced Third-Order Optical Nonlinearity in Refractory Titanium Nitride Nanostructures. *ACS Photonics* **2018**, *5*, 3452–3458.
46. (31) George, H.; Reed, J.; Ferdinandus, M.; DeVault, C.; Lagutchev, A.; Urbas, A.; Norris, T. B.; Shalaev, V. M.; Boltasseva, A.; Kinsey, N. Nonlinearities and Carrier Dynamics in Refractory Plasmonic TiN Thin Films. *Opt. Mater. Express* **2019**, *9* (10), 3911.
47. (32) Diroll, B. T.; Saha, S.; Shalaev, V. M.; Boltasseva, A.; Schaller, R. D. Broadband Ultrafast Dynamics of Refractory Metals: TiN and ZrN. *Adv. Opt. Mater.* **2020**, *8* (19), 2000652.
48. (33) Dal Forno, S.; Lischner, J. Electron-Phonon Coupling and Hot Electron Thermalization in Titanium Nitride. *Phys. Rev. Mater.* **2019**, *3* (11), 115203.
49. (34) Askes, S. H. C.; Schilder, N. J.; Zoethout, E.; Polman, A.; Garnett, E. C. Tunable Plasmonic HfN Nanoparticles and Arrays. *Nanoscale* **2019**, *11* (42), 20252–20260.
50. (35) Rudy, E. The Crystal Structures of Hf_3N_2 and Hf_4N_3. *Metall. Mater. Trans. B* **1970**, *1* (5), 1249–1252.
51. (36) Dahal, N.; Chikan, V. Synthesis of Hafnium Oxide-Gold Core–Shell Nanoparticles. *Inorg. Chem.* **2012**, *51* (1), 518–522.
52. (37) Monfared, Y. E.; Dasog, M. Computational Investigation of the Plasmonic Properties of TiN, ZrN, and HfN Nanoparticles: The Role of Particle Size, Medium,

and Surface Oxidation.*Can. J. of Chem.*, **Just-IN**. https://doi.org/10.1139/cjc-2020-0335

53. (38) Berrospe Rodriguez, C.; Alvarez Barragan, A.; Nava, G.; Exarhos, S.; Mangolini, L. Stabilizing the Plasmonic Response of Titanium Nitride Nanocrystals with a Silicon Oxynitride Shell: Implications for Refractory Optical Materials. *ACS Appl. Nano Mater.* **2020**, *3* (5), 4504–4511.
54. (39) Alvarez Barragan, A.; Ilawe, N. V.; Zhong, L.; Wong, B. M.; Mangolini, L. A Non-Thermal Plasma Route to Plasmonic TiN Nanoparticles. *J. Phys. Chem. C* **2017**, *121* (4), 2316–2322.
55. (40) Karaballi, R. A.; Humagain, G.; Fleischman, B. R. A.; Dasog, M. Synthesis of Plasmonic Group-4 Nitride Nanocrystals by Solid-State Metathesis. *Angew. Chem - Int. Ed.* **2019**, *58* (10), 3147–3150.
56. (41) Link, S.; El-Sayed, M. A. Spectral Properties and Relaxation Dynamics of Surface Plasmon Electronic Oscillations in Gold and Silver Nanodots and Nanorods. *J. Phys. Chem. B* **1999**, *103* (40), 8410–8426.
57. (42) Hu, M.; Wang, X.; Hartland, G. V; Salgueiriño-Maceira, V.; Liz-Marzán, L. M. Heat Dissipation in Gold–Silica Core-Shell Nanoparticles. *Chem. Phys. Lett.* **2003**, *372* (5–6), 767–772.
58. (43) Hu, M.; Hartland, G. V. Heat Dissipation for Au Particles in Aqueous Solution: Relaxation Time versus Size. *J. Phys. Chem. B* **2002**, *106* (28), 7029–7033.
59. (44) Hashimoto, S.; Werner, D.; Uwada, T. Studies on the Interaction of Pulsed Lasers with Plasmonic Gold Nanoparticles toward Light Manipulation, Heat Management, and Nanofabrication. *J. Photochem. Photobiol. C Photochem. Rev.* **2012**, *13* (1), 28–54.
60. (45) Link, S.; Furube, A.; Mohamed, M. B.; Asahi, T.; Masuhara, H.; El-Sayed, M. A. Hot Electron Relaxation Dynamics of Gold Nanoparticles Embedded in $MgSO_4$ Powder Compared To Solution: The Effect of the Surrounding Medium. *J. Phys. Chem. B* **2002**, *106* (5), 945–955..
61. (46) Hu, M.; Hartland, G. V. Heat Dissipation for Au Particles in Aqueous Solution: Relaxation Time versus Size. *J. Phys. Chem. B* **2002**, *106* (28), 7029–7033.
62. (47) Brown, A. M.; Sundararaman, R.; Narang, P.; Schwartzberg, A. M.; Goddard, W. A.; Atwater, H. A. Experimental and Ab Initio Ultrafast Carrier Dynamics in Plasmonic Nanoparticles. *Phys. Rev. Lett.* **2017**, 118(8):087401
63. (48) Jensen, E. T.; Palmer, R. E.; Allison, W.; Annett, J. F. Temperature-Dependent Plasmon Frequency and Linewidth in a Semimetal. *Phys. Rev. Lett.* **1991**, *66* (4), 492–495.
64. (49) Allen, P. B. Theory of Thermal Relaxation of Electrons in Metals. *Phys. Rev. Lett.* **1987**, *59* (13), 1460–1463.
65. (50) Westrum, E. F.; Sommers, J. A. Heat Capacity of Hanium Mononitride from Temperatured of 5 to 350 K An Estimation Procedure. **2002**, *69*, 103–112.
66. (51) Peirson, H. O. *Handbook of Refractory Carbides and Nitrides: Properties, Characteristics, Processing, and Applications*; William Andrew Publishing/Noyes, 1996.

67. (52) Chen, X.; Struzhkin, V. V; Kung, S.; Mao, H.; Hemley, R. J.; Christensen, A. N. Pressure-Induced Phonon Frequency Shifts in Transition-Metal Nitrides. *Phys. Rev. B* **2004**, *70*, 014501.
68. (53) Chauhan, M.; Gupta, D. C. Structural, Electronic, Mechanical and Thermo-Physical Properties of TMN (TM = Ti , Zr and Hf) under High Pressures : A First-Principle Study. *Int. J. Refract. Met. hard Mater.* **2014**, *42*, 77–90.
69. (54) Spengler, W.; Kaiser, R.; Christensen, A. N.; Müller-Vogt, G. Raman Scattering, Superconductivity, and Phonon Density of States of Stoichiometric and Nonstoichiometric TiN. *Phys. Rev. B* **1978**, *17* (3), 1095–1101.
70. (55) Lin, Z.; Zhigilei, L. V.; Celli, V. Electron-Phonon Coupling and Electron Heat Capacity of Metals under Conditions of Strong Electron-Phonon Nonequilibrium. *Phys. Rev. B* **2008**, *77* (7), 075133.
71. (56) Forno, S. D.; Lischner, J. Electron-Phonon Coupling and Hot Electron Thermalization in Titanium Nitride. *Phys. Rev. Mater.* **2019**, *3*, 115203.
72. (57) Böttger, P. H. M.; Lewin, E.; Patscheider, J.; Shklover, V.; Cahill, D. G.; Ghisleni, R.; Sobiech, M. Thermal Conductivity of Hard Oxynitride Coatings. *Thin Solid Films* **2013**, *549*, 232–238.
73. (58) Alper, J.; Hamad-Schifferli, K. Effect of Ligands on Thermal Dissipation from Gold Nanorods. *Langmuir* **2010**, *26* (6), 3786–3789.
74. (59) Hartland, G. V. Measurements of the Material Properties of Metal Nanoparticles by Time-Resolved Spectroscopy. *Phys. Chem. Chem. Phys.* **2004**, *6* (23), 5263.
75. (60) Briggs, J. A.; Naik, G. V.; Zhao, Y.; Petach, T. A.; Sahasrabuddhe, K.; Goldhaber-Gordon, D.; Melosh, N. A.; Dionne, J. A. Temperature-Dependent Optical Properties of Titanium Nitride. *Appl. Phys. Lett.* **2017**, *110,* 101901 .
76. (61) Reddy, H.; Guler, U.; Kudyshev, Z.; Kildishev, A. V.; Shalaev, V. M.; Boltasseva, A. Temperature-Dependent Optical Properties of Plasmonic Titanium Nitride Thin Films. *ACS Photonics* **2017**, *4* (6), 1413–1420.
77. (62) Mulvaney, P. Surface Plasmon Spectroscopy of Nanosized Metal Particles. *Langmuir* **1996**, *12* (3), 788–800.
78. (63) Saha, B.; Acharya, J.; Sands, T. D.; Waghmare, U. V. Electronic Structure, Phonons, and Thermal Properties of ScN, ZrN, and HfN: A First-Principles Study. *J. Appl. Phys.* **2010**, *107* (3).
79. (64) Zhou, L.; Zhang, C.; McClain, M. J.; Manjavacas, A.; Krauter, C. M.; Tian, S.; Berg, F.; Everitt, H. O.; Carter, E. A.; Nordlander, P.; et al. Aluminum Nanocrystals as a Plasmonic Photocatalyst for Hydrogen Dissociation. *Nano Lett.* **2016**, *16* (2), 1478–1484.
80. (65) Tagliabue, G.; DuChene, J. S.; Abdellah, M.; Habib, A.; Gosztola, D. J.; Hattori, Y.; Cheng, W. H.; Zheng, K.; Canton, S. E.; Sundararaman, R.; et al. Ultrafast Hot-Hole Injection Modifies Hot-Electron Dynamics in Au/p-GaN Heterostructures. *Nat. Mater.* **2020**, *19* (12), 1312–1318.
81. (66) Patsalas, P.; Kalfagiannis, N.; Kassavetis, S.; Abadias, G.; Bellas, D. V.; Lekka, C.; Lidorikis, E. Conductive Nitrides: Growth Principles, Optical and Electronic

Properties, and Their Perspectives in Photonics and Plasmonics. *Mater. Sci. Eng. R Reports* **2018**, *123*, 1–55.

82. (67) Ploetz, E.; Laimgruber, S.; Berner, S.; Zinth, W.; Gilch, P. Femtosecond Stimulated Raman. *Appl. Phys. B* **2007**, *87*, 389–393. https://doi.org/10.1007/s00340-007-2630-x.
83. (68) Umapathy, S.; Lakshmanna, A.; Mallick, B. Ultrafast Raman Loss Spectroscopy. *J. Raman Spectrosc.* **2009**, *40*, 235–237.
84. (69) Harbola, U.; Umapathy, S.; Mukamel, S. Loss and Gain Signals in Broadband Stimulated-Raman Spectra : Theoretical Analysis. *Phys. Rev. A* **2013**, *88*, 011801(R).
85. (70) Kharintsev, S. S.; Kharitonov, A. V.; Saikin, S. K.; Alekseev, A. M.; Kazarian, S. G. Nonlinear Raman Effects Enhanced by Surface Plasmon Excitation in Planar Refractory Nanoantennas. *Nano Lett.* **2017**, *17* (9), 5533–5539.
86. (71) Kinsey, N.; Syed, A. A.; Courtwright, D.; DeVault, C.; Bonner, C. E.; Gavrilenko, V. I.; Shalaev, V. M.; Hagan, D. J.; Van Stryland, E. W.; Boltasseva, A. Effective Third-Order Nonlinearities in Metallic Refractory Titanium Nitride Thin Films. *Opt. Mater. Express* **2015**, *5* (11), 2395.
87. (72) Kontoleta, E.; Tsoukala, A.; Askes, S. H. C.; Zoethout, E.; Oksenberg, E.; Agrawal, H.; Garnett, E. C. Using Hot Electrons and Hot Holes for Simultaneous Cocatalyst Deposition on Plasmonic Nanostructures. *ACS Appl. Mater. Interfaces* **2020**, *12* (32), 35986–35994.
88. (73) Turkevich, J.; Stevenson, P. C.; Hillier, J. A Study of the Nucleation and Growth Processes in the Synthesis of Colloidal Gold. *Discuss. Faraday Soc.* **1951**, *11*, 55.
89. (74) Kimling, J.; Maier, M.; Okenve, B.; Kotaidis, V.; Ballot, H.; Plech, A. Turkevich Method for Gold Nanoparticle Synthesis Revisited. *J. Phys. Chem. B* **2006**, *110*, 15700–15707.
90. (75) Lessing, H. E.; von Jena, A. Separation of Rotational Diffusion and Level Kinetics in Transient Absorption Spectroscopy. *Chem. Phys. Lett.* **1977**, *46* (2), 213–217.
91. (76) Schott, S.; Steinbacher, A.; Buback, J.; Nuernberger, P.; Brixner, T. Generalized Magic Angle for Time-Resolved Spectroscopy with Laser Pulses of Arbitrary Ellipticity. *J. Phys. B At. Mol. Opt. Phys.* **2014**, *47*, 124014.
92. (77) Snellenburg, J. J.; Laptenok, S.; Seger, R.; Mullen, K. M.; van Stokkum, I. H. M. Glotaran: A Java-Based Graphical User Interface for the R Package TIMP. *J. Stat. Softw.* **2012**, *49*, 1–22.
93.

Appendix C: Supporting Information for Chapter 5

1 Transient Absorption Spectroscopy

A home build transient absorption setup (described in main text) was used to observe the ultrafast photodynamics. A 1 mm cuvette containing the colloidal suspensions was continuously moved in the plane of the pump/probe overlap. No less than 10 repetitions were combined to obtain the data sets. The development of the signal was fit with a Gaussian rise-time and appropriate decay using Matlab 2018b; time correction was carried out based on the fit. While this does not model the ultrafast (~100 fs) signal likely due to stimulated Raman scattering (see main text), it allows for fitting with a stretched exponential decay while also fitting the signal development.

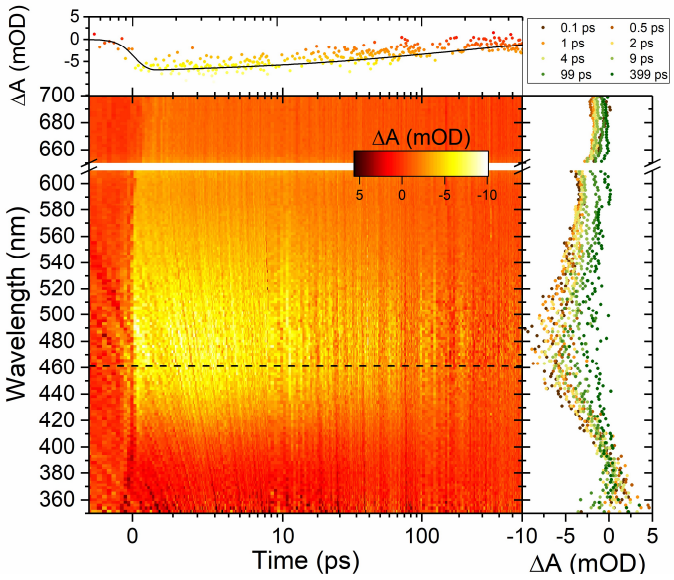

Figure S1. TA contour plot with $\lambda_{exc.}$ = 630 nm for HfN nanoparticles in water. Top: time-trace at 462 nm with a stretched-exponential fit. Right: spectra at selected time delays.

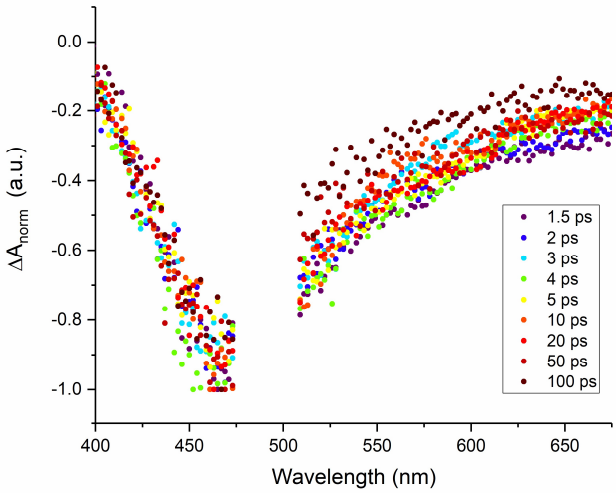

Figure S2. TA spectra at various time delays of HfN nanoparticles in water, normalized so the minimum value is -1. There is little difference between the normalized spectra, which supports the argument that the signal is due to heating for all observable time scales.

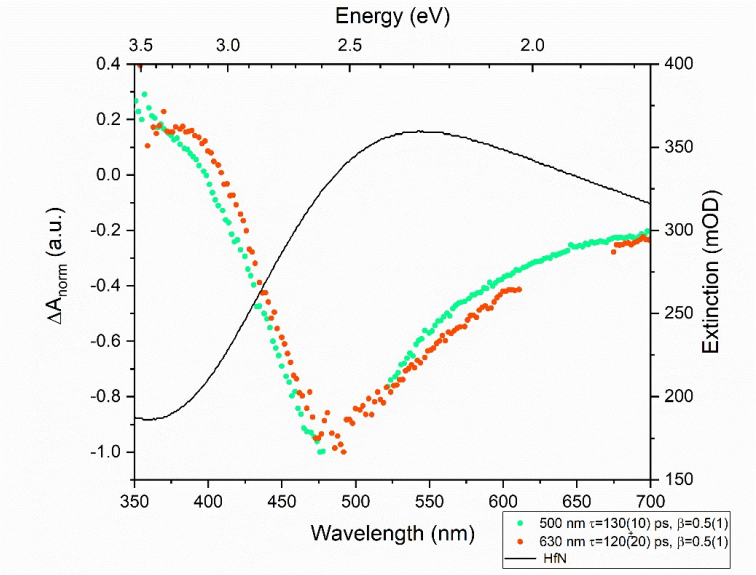

Figure S3. Normalized decay associated spectra (DAS) for HfN nanoparticles in water, fit with a stretched exponential, and the extinction of the sample. The shape of the DAS from both 500 nm and 630 nm excitation show an almost similar shape, indicating that a similar population was excited.

a

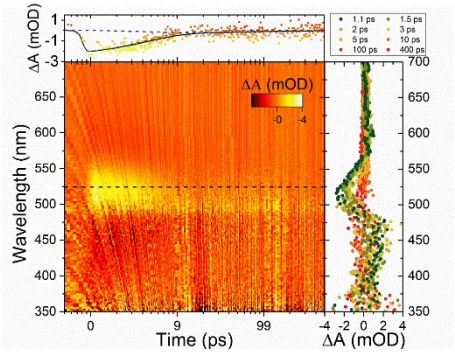

b

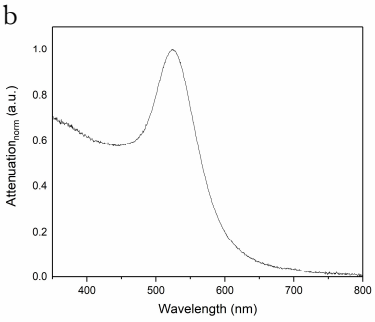

Figure S4. A: TA contour plot with $\lambda_{exc.}$ = 500 nm for Au nanoparticles. Top: time trace at 524 nm with a two-component exponential fit (individual components shown with dashed lines). Right: TA spectra at selected time delays. B: UV-Vis absorbance spectrum of colloidal Au nanoparticles in water.

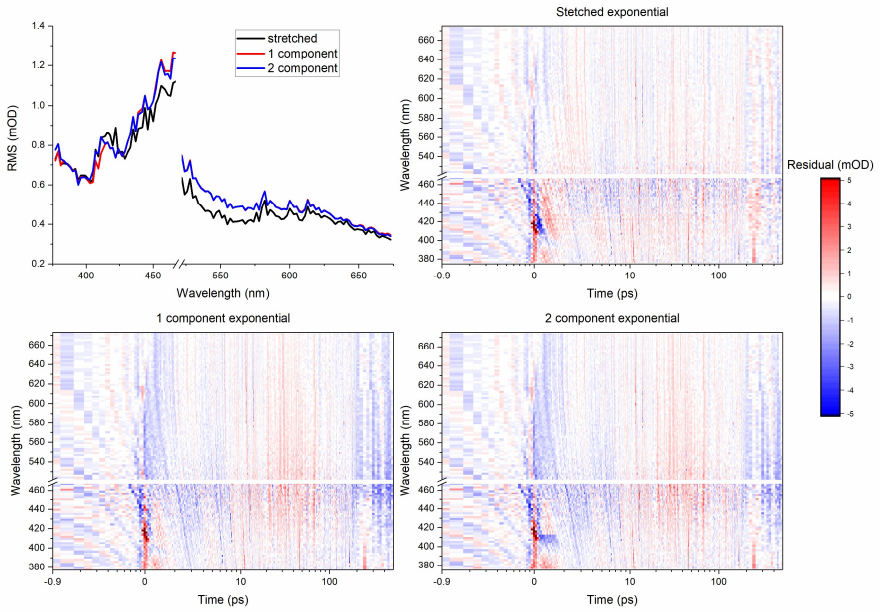

Figure S5. Depiction of the errors from fitting a stretched exponential to TA data obtained at 500 nm excitation, and one or two-component exponentials. Top left: the root mean square of the residuals after each fit for each wavelength. Top right and lower plots: Residual contour plots for each fitting method.

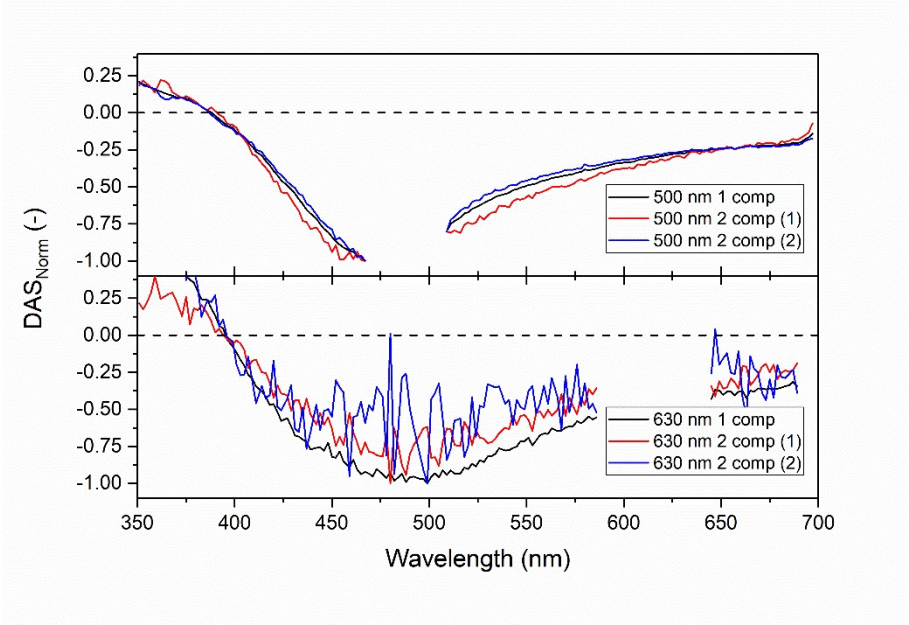

Figure S6. The DAS for one and two-component exponential fits obtained from Glotaran.[1] That both DAS from the two-component fit are so similar is a clear indication of overfitting and suggests that it is the same phenomenon which is inducing the change. However, the one-component fit is a relatively poor fit, while the stretched exponential (with a DAS very similar to the one-component exponential) is in excellent agreement with the data. The use of the stretched exponential fit is known to be appropriate for thermal dissipation.[2] Our calculations show that HfN nanoparticles have a high electron-phonon coupling constant, which cause our simulations to show a very short lifetime for hot-carriers such that for observable time scales the TA signal is expected to be of thermal origin.

2 Methodology of three-dimensional heat transfer simulations

2.1 Description of COMSOL geometry and simulation settings

COMSOL Multiphysics 5.1 was used to simultaneously solve the heat-transfer equations governing the electron and lattice temperatures, as well as the heat transfer to the aqueous surroundings. A spherical geometry was designed in which a spherical HfN or Au nanoparticle (20 nm diameter) was surrounded by a sphere of water (300 nm diameter). A four-fold symmetry was used to minimize computational requirement, with symmetry boundary conditions on the inner sections. The geometry was meshed free tetrahedrals with 15 nm and 0.5 nm maximum and minimum element sizes, respectively, 1.15 maximum element growth rate, 0.1 curvature factor, and 0.85 resolution for narrow regions. The HfN sphere was meshed with 12× scale in all directions. Additionally, to avoid numerical artefacts due to high instantaneous temperature gradients during the fs-laser pulse, 16 boundary layers were applied to the nanoparticle-water interface, and, for oxidized HfN nanoparticles, to the HfN-HfO_2 interface. These settings yielded a tetrahedral mesh consisting of 85260 individual elements (Figure b and c). A time dependent study was employed with a fully coupled MUMPS solver. To accurately capture all dynamics on all timescales, while retaining a complete simulation time range of 100 ns, the time stepping was made progressively precise around the pulse time center, set at a delay of t = 1 ps (Table S1), with intermediate time stepping setting. The total simulation time was approximately 18 min on an Intel Core i7 2.20 GHz processor with 8 GB RAM.

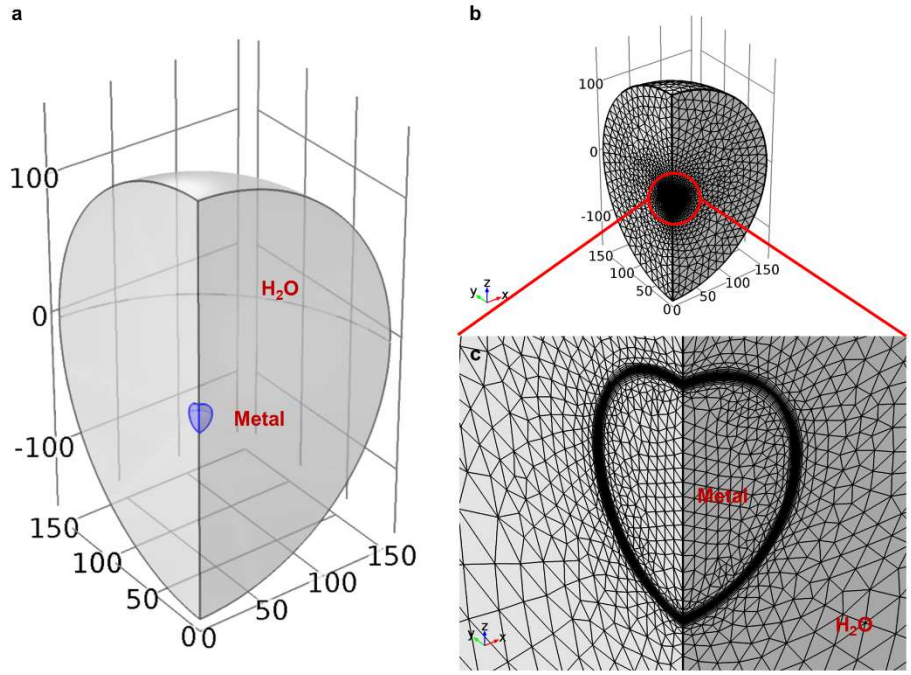

Figure S7. COMSOL simulation geometry (a) and simulation mesh for HfN and Au nanoparticles (b/c). The blue inner sphere in panel a is the 20 nm diameter metal nanosphere, surrounded by a 300 nm diameter H_2O sphere.

Table S1. Time stepping settings of the COMSOL simulation.

Time range (ps)	*Time step (ps)*
0 – 0.8	0.2
0.81– 0.9	0.01
0.9-1.1 (around laser pulse)	0.005
1.11-1.2	0.01
1.22 – 2	0.02
2.1 – 5	0.1
6 – 50	1
52 – 300	2
310 – 990	10
1000 – 8000	100
9000 – 100 000	1000

2.2 Heat transfer and electron-phonon coupling

We use a Dual-Parabolic Two-Step model (DPTS) to fully account for heating and heat transfer contributions in both electron and phonon population.[3] In particular, we choose to explicitly model the heat transfer in the lattice due to the strong coupling of electrons and phonons in this material, which results in strong contribution of both components to the thermal conductivity at all timescales. Moreover, in HfN the lattice contributes much more to the equilibrium thermal conductivity than in typical metals, which is discussed below. Kinsey and coworkers have recently shown the validity of the DPTS model in the case of a transient reflectivity measures of TiN thin films.[4] Within the HfN nanoparticle domain (the blue domain in Figure a) the following coupled partial differential equations apply:

$$C_e(T_e)\frac{\partial T_e}{\partial t} = \nabla[\kappa_e(T_e)\,\nabla T_e] - G(T_e - T_l) + q(x,y,z,t) \qquad \text{Equation 1}$$

$$C_l(T_l)\frac{\partial T_l}{\partial t} = \nabla[\kappa_l(T_l)\,\nabla T_l] + G(T_e - T_l) \qquad \text{Equation 2}$$

where subscripts *e* and *l* distinguish between electronic and lattice terms, *T* is the temperature (in K), *C(T)* is the temperature-dependent volumetric heat capacity (in J/m^3.K), $\varkappa$ is the thermal conductivity (in W/m.K), *G* is the electron-phonon coupling constant (in W/m^3.K), and q(x,y,z,t) is the pulsed laser heating term (in W/m^3). The initial temperature was set to 293.15 K. The electronic temperature was

fully isolated from the water surroundings, that is, no electron energy transfer occurs to water. The lattice temperature is fully coupled with the water temperature, see below. Due to the absence of ligands around the HfN nanoparticles, interfacial heat transfer resistance was neglected at the HfN-H_2O interface. However, we realized that the HfN nanoparticle is oxidized at the surface, thereby introducing a thin HfO_xN_y layer that could introduce a heat transfer resistance ($\varkappa_{HfO2} \approx 1.1$ W/m.K). We therefore included a model in which the HfN core is surrounded by a 1 nm thin HfO_2 shell, see main text.

In practice, the electron temperature was simulated using the "Heat Transfer in Fluids" module, and the lattice temperature was simulated using the "Heat Transfer in Solids" module. Heat transfer through convection or radiation were neglected. To account for the temperature coupling, both modules were linked using the "Local Thermal Non-Equilibrium" module. This module is originally designed for solid-liquid heat transfer in porous media, in which case the heat exchange term (named q_{sf} in COMSOL, instead of G) and heat capacity terms in Equation and Equation are multiplied by the solid weight fraction. Thus, to correctly adapt this built-in model for electron-lattice thermal equilibration, the solid weight fraction was set to 0.5, the material density for HfN (or Au) was multiplied by 2, and the G factor was multiplied by 2.

For the water domain, Equation 3 applied with an outside boundary temperature fixed at 293 K and an initial temperature set to 293 K. Within the model, the water temperature is also defined as "lattice" temperature (subscript l).

$$C_l(T_l)\frac{\partial T_l}{\partial t} = \nabla[\kappa_l(T_e)\,\nabla T_l] \qquad \text{Equation 3}$$

The temperature-dependent electronic heat capacity is calculated using the Debye approximation:

$$C_e(T_e) = \frac{\gamma \rho T_e}{M_W} \qquad \text{Equation 4}$$

where γ is the Sommerfeld constant (1.2×10^{-3} J/mol.K^2),[5] ϱ is the density (13680 kg/m^3), and M_W is the molar weight (M_w = 0.1925 kg/mol). This approximation holds well for noble metals in the low electron temperature regime ($0 < T_e < 0.1T_F$, with T_F being the Fermi temperature, that is $T_F = E_F/k_B \approx 6 \times 10^4$ K)[6], and holds for group 4b transition metal nitrides as well.[7]

The temperature-dependent heat capacity of HfN has been reported by Westrum and Sommers from 5.6 – 346 K,[5] which is in agreement with theoretical works by Saha *et al.*[8] and Gupta *et al.*[9], as well as the tabulated value at 293 K (38 J/mol.K, that is 2.70×10^5 J/m^3.K).[10] These tabulated data were extracted and used for $C_l(T_l)$, and fitted with the 6th-order polynomial in Equation 5 below. Initially, a more appropriate hyperbolic fitting function was used, which is an accurate approximation for group 4b nitrides.[7–9] However, for unknown reasons, the use of the hyperbolic function within COMSOL led to a three-fold increase in simulation time. Furthermore, we assumed a negligible electronic component in this data, due to the much lower heat capacity of electrons compared to phonons. Indeed, this is justified by realizing that the magnitude of $C_e(T_e)$ at any temperature is less than 2% of $C_l(T_l)$, see Figure a and b.

$$C_l(T_l) = -5.33 \times 10^5 + 2.41 \times 10^4 T_l - 67.5 T_l^2 + 0.109 T_l^3 - 9.85 \times 10^{-5} T_l^4 + 4.62 \times 10^{-8} T_l^5 - 8.72 \times 10^{-12} T_l^6 \quad \text{Equation 5}$$

For metals, the total thermal conductivity is given by the linear combination of electronic and lattice contributions, with weights a and b, respectively:

$$\kappa(T) = a\kappa_e(T_e) + b\kappa_l(T_l) \quad \text{Equation 6}$$

The total thermal conductivity of HfN was extracted from Opeka *et al.* and Wuchina *et al.*,[11,12] which is in good agreement with the Handbook of of Refractory Carbides and Nitrides ($\varkappa$(293 K) = 21.7 W/m.K)[10], and fitted with the polynomial in Equation 7, below, plotted in Figure . The thermal conductivity of HfN is considerably lower than that of Au ($\varkappa$(293 K) = 318 W/m.K). We also note that the extracted thermal conductivity of HfN includes the effect of material defects, which lower the thermal conductivity substantially. Bao and co-authors showed that the theoretical value of defect-free HfN is approximately 90 W/m.K at 300 K.[13]

$$\kappa(T) = 14.02 + 0.01697T - 5.33 \times 10^{-6} T^2 \quad \text{Equation 7}$$

For metals such as gold, the overall thermal conductivity stems primarily from the electrons, so that $a \approx 0.99$, while the lattice contributes very little, so that $b \approx 0.01$.[3] However, in the case of HfN, it was recently shown that the phonon contribution is much larger, in the order of 25%.[13] Therefore, for HfN we used $a = 0.25$ and $b = 0.75$:

$$\kappa_e(T_e) = 0.25\kappa(T)$$ Equation 8

$$\kappa_l(T_l) = 0.75\kappa(T)$$ Equation 9

For simulations on Au, the built-in lattice heat capacity and thermal conductivity was used (plotted in Figure), while the electronic heat capacity was calculated using Equation 4, where $\frac{\gamma\rho}{M_W} = 71.4$ J/m^3.K (= 0.729 × 10^{-3} J/mol.K^2).[14]

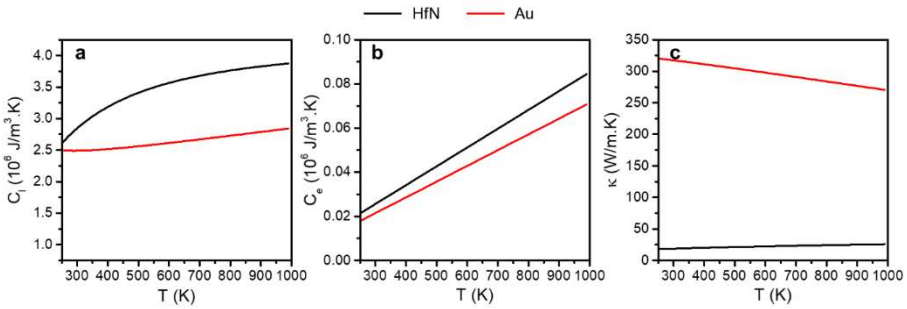

Figure S8. Lattice heat capacity (a), electronic heat capacity (b), and total thermal conductivity (c) of HfN (red curves) and Au (black curves).

The electron-phonon coupling constant *G* was calculated from literature values by using the following approximation, which has been derived by Allen in 1987,[15] and later used for TiN thin film experiments by the group of Kinsey[4] and in theoretical work by Lischner and co-workers[7]:

$$G = \frac{3\gamma\lambda\langle\omega_2\rangle\rho}{\hbar\pi k_B M_W}$$ Equation 10

where γ is the Sommerfeld constant (1.2 × 10^{-3} J/mol.K^2), λ is the Bardeen-Cooper-Schrieffer electron-phonon coupling constant (0.643 for HfN, no units),[16] $\langle\omega_2\rangle$ is the second moment of the phonon spectrum (in J^2), ϱ is the material density (13680 kg/m^3), $\hbar$ is the reduced Planck's constant (6.626 × 10^{-34}/2π J.s), k_B is the Boltzmann constant (1.38 × 10^{-23} J/K) and M_W is the molar weight of HfN (0.1925 kg/mol).

The combined terms $\lambda\langle\omega_2\rangle$ is also known as the Eliashberg function. Although a value for $\langle\omega_2\rangle$ is not readily available for HfN in literature, it is possible to estimate $\langle\omega_2\rangle$ from the Debye temperature θ_D^0 (421 - 484 K,[5,10,16] 491 K theoretical prediction[17]) according to Equation 11:[4,18]

$$\langle\omega_2\rangle = (\theta_D^0 k_B)^2 = 3.4 \times 10^{-41} - 4.5 \times 10^{-41} J^2 \qquad \text{Equation 11}$$

Thus, Equation 10 becomes:

$$G = \frac{3\gamma\lambda\langle\omega_2\rangle\rho}{\hbar\pi k_B M_W} = 1.2 \times 10^{18} - 1.6 \times 10^{18}\ W/m^3K \qquad \text{Equation 12}$$

Such high *G* values in the order of 10^{18} are two to three orders of magnitude higher than measured values reported for Au as compiled by Hohlfeld and coworkers: $1.1 - 4 \times 10^{16}$ W/m^3.K.[19] For simulation purposes we use an averaged value of 1.4×10^{18} W/m^3.K. Here, equation 12 was as also used to calculate *G* for Au, which resulted in a value that falls accurately within the reported range (2.78×10^{16} W/m^3.K, see Table S2). The high *G* values for HfN are is in line with what has been recently reported for the related materials TiN and ZrN in literature.[4,7,20] A high G-value immediately indicates short hot carrier lifetimes. Although the value of *G* varies with electronic temperature,[7] within the temperature range in this work it can be approximated as a constant value.

Table S2. Summary of parameters used to calculate the electron-phonon coupling constant (G) for HfN and Au.

Material	*HfN*	*Au*
γ $(J/mol.K^2)$	1.2×10^{-3} [5]	0.729×10^{-3} [14]
a	0.25 [13]	0.01 [3]
b	0.75 [13]	0.99 [3]
λ	0.643 [16]	0.13 [21]
$\langle\omega_2\rangle$ (J^2)	$3.4 \times 10^{-41} - 4.5 \times 10^{-41}$ (calc.)	4.57×10^{-42} [21]
θ_D^0 (K)	421 – 484 [5,10,16]	170 [14]
ϱ (kg/m^3)	13680	19320
M_W (kg/mol)	0.1925	0.1970
G $(W/m^3.K)$	1.4×10^{18} (calc.)	2.78×10^{16} (calc.)

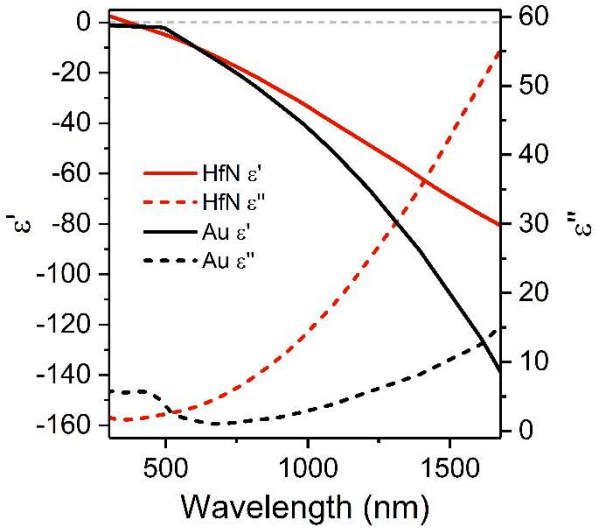

Figure S9. Real (left axis, solid lines) and imaginary permittivity (right axis, dashed lines) of HfN (red)[22] and Au (black).[23]

2.3 Optical heat source

The spatial and temporal heating profile $q(x,y,z,t)$ originating from laser pulse excitation was modelled as follows. First, finite difference time domain (FDTD) simulations were conducted using Lumerical software to solve Maxwell's equations for a 20 nm diameter HfN nanosphere in aqueous surroundings, under λ = 500 nm plane-wave excitation. Optical constants for HfN were used from previous work in which high quality thin film HfN was studied (Figure).[22] For Au, the optical constants from Johnson and Christy were used.[23] The background refractive index was set to 1.333 (H_2O). Four-fold axial symmetry was used. A cross section monitor was used to obtain the absorption and scatter cross sections (σ_{abs} and σ_{scat}), see Figure S7a-c. An electric field monitor was used to visualize the field enhancement around the nanoparticle (see main text). An advanced absorbed power monitor was used to retrieve the three-dimensional absorbed power profile within the nanoparticle, which is proportional to the product of electric field intensity (E^2) and the imaginary part of the permittivity (ε''), see Figure S7d-f. Since the nanoparticle diameter is thinner than the plasmonic skin depth, for each system we observe near-homogeneous absorption throughout the entire nanoparticle volume, although there are subtle absorption gradients. To normalize the absorption profile, all output values were divided by the global average within the nanoparticle domain to yield $\bar{P}_{abs}(x,y,z)$, which was subsequently imported in Comsol as an interpolated function, with linear interpolation and an extrapolated value of 0. A plot of $\bar{P}_{abs}(x,y,z)$ is given in Figure S7d and e.

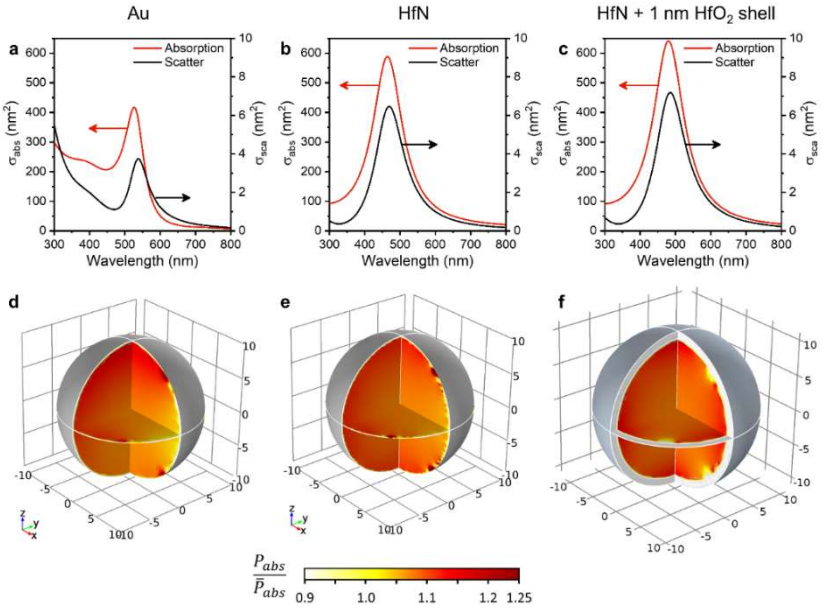

Figure S70. Results of finite difference time domain simulations for Au, HfN, and oxidized HfN nanoparticles. a-c) Absorption (red) and scatter cross section spectra (black) for Au (a), HfN (b) and oxidized HfN (c). d-f) Normalized spatial absorbed power maps for Au (d), HfN (e), and oxidized HfN (f) nanospheres.

The peak heating power for the single nanoparticle (q_{peak} in W) was obtained from the average laser beam power (P_{ave} = 2 mW), laser repetition frequency (f_{rep} = 5 kHz), laser pulse full width half maximum (FWHM = 50 fs), laser beam area (beam radius = 100 μm, i.e. $A = 0.0314 \times 10^{-6}$ m^2), and absorption cross section (for HfN $\sigma_{abs} = 589 \times 10^{-18}$ m^2):

$$q_{peak} = 0.94 \frac{P_{ave}\sigma_{abs}}{f_{rep} \times A \times FWHM} = 139 \times 10^{-3}\ W \qquad \text{Equation 13}$$

Finally, $q(x,y,z,t)$ was obtained by multiplying the product of q_{peak} and $\bar{P}_{abs}(x,y,z)$ by a normalized gaussian temporal pulse (with σ = FWHM/2.3548 = 21.2 fs), which was centered at 1 ps for practical purposes. To account for the four-fold symmetry in the geometry, q_{peak} was divided by 4.

$$q(x,y,z,t) = e^{\frac{(t-1\times10^{-12})^2}{2\sigma^2}} \times \frac{q_{peak}}{4} \times \bar{P}_{abs}(x,y,z) \qquad \text{Equation 14}$$

2.4 Heat transfer modelling data

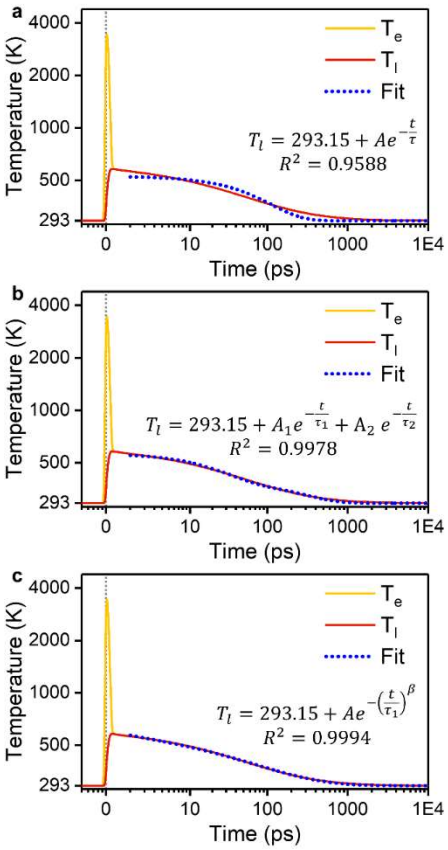

Figure S8. Comparison of different fitting functions for the decay of simulated lattice temperature (red curves) during 50 fs pulsed irradiation of HfN nanoparticles. Fitting was performed in the 1 – 1000 ps domain. a) Single exponential decay, showing a poor fit to the data ($R^2 = 0.9588$). A = 232.7 K and τ = 93.2 ps. b) Double exponential decay, showing a better fit to the data than a single exponential function ($R^2 = 0.9978$). However, the function oscillates around the data, showing that it is not the ideal fit function. A_1 = 168.0 K, τ_1 = 26.4 ps, A_2 = 96.8 K, and τ_2 = 282.6 ps. c) Stretched exponential decay, showing excellent agreement with the data (R^2 = 0.9994). A = 327.7 K, τ = 42.9 ps, β = 0.44. Overall, the stretched exponential function provides the best fit to the data, which is in agreement with the work of Hu and Hartland, who have shown this phenomenon experimentally for Au nanoparticles of various sizes.[2]

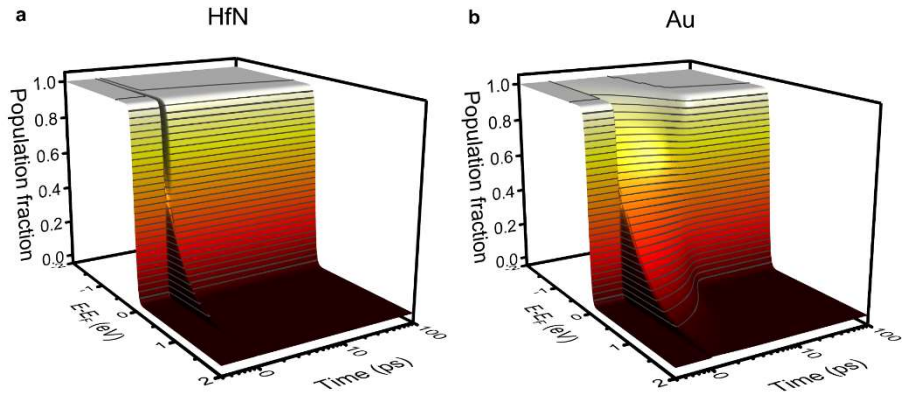

Figure S9. Simulated Fermi-Dirac electron distributions for HfN (a) and Au (b) nanoparticles during 50 fs laser excitation, generated by inserting the simulated electron temperature (T_e) in Equation 15. Note that the equation is not valid in the time interval of electronic excitation and electron-electron scatter (that is, between -0.1 and ~0.1 ps).

$$f(E) = \frac{1}{1 + e^{E - E_F / kT_e}}$$ Equation 15

where k = 8.617 × 10^{-5} eV/K

2.5 Temperature dependent ellipsometry

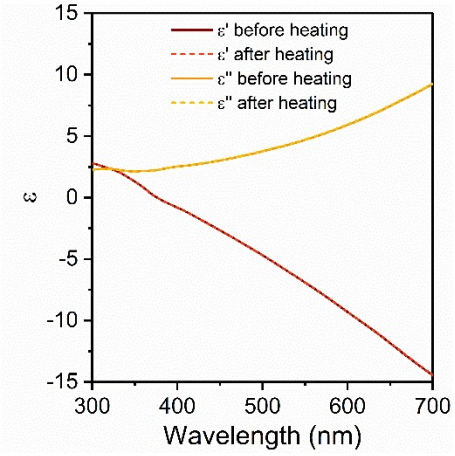

Figure S10. Real and imaginary permittivity of HfN for an alumina-covered HfN sample at room temperature, extracted from temperature-variable ellipsometry, before (solid lines) and after (dashed lines) the heating cycle to 523 K (250° C). The data perfectly overlaps, indicating no material changes during temperature cycling.

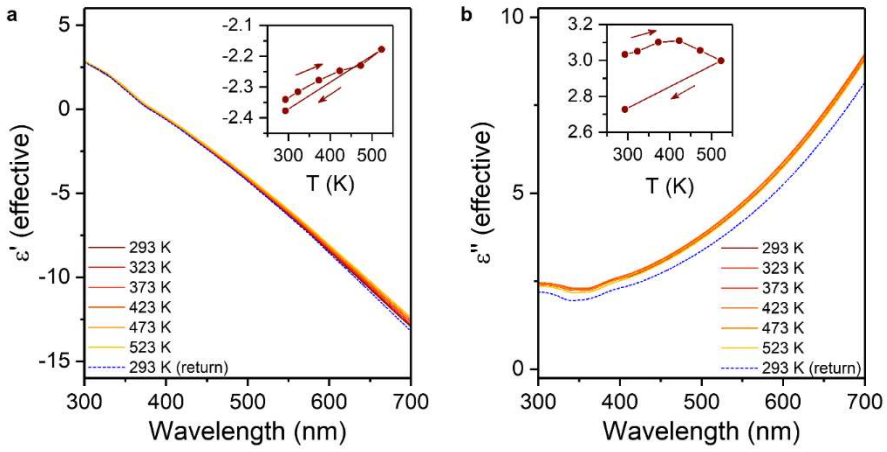

Figure S11. Effective real (a) and imaginary permittivity (b) of HfN (without alumina) during temperature increase from room temperature (red) to 523 K (250 °C; yellow). Insets show data at 450 nm as a function of temperature. The data for the cooled down sample are shown in blue, indicating relatively large changes as a result of temperature cycling. The changes most likely reflect surface roughening and growth of the oxide layer.

3 References

1. Snellenburg, J. J., Laptenok, S., Seger, R., Mullen, K. M. & van Stokkum, I. H. M. Glotaran: A Java-based graphical user interface for the R package TIMP. *J. Stat. Softw.* **49**, 1–22 (2012).

2. Hu, M. & Hartland, G. V. Heat Dissipation for Au Particles in Aqueous Solution: Relaxation Time versus Size. *J. Phys. Chem. B* **106**, 7029–7033 (2002).

3. Zhang, Y., Tzou, D. Y. & Chen, J. K. High-Power and Femtosecond Lasers: Properties, Materials and Applications, Barret, P.H., and Palmerm, M., eds., Nova Science Publishers, Inc., Hauppauge, NY, 2009, Chapter 5, pp. 159-206

4. George, H. *et al.* Nonlinearities and carrier dynamics in refractory plasmonic TiN thin films. *Opt. Mater. Express* **9**, 3911 (2019).

5. Westrum, E. F. & Sommers, J. A. Heat capacity of hafnium mononitride from temperatures of 5 to 350 K. An estimation procedure. *J. Therm. Anal. Calorim.* **69**, 103–112 (2002).

6. Ashcroft, N. W.; Mermin, N. D. *Solid state physics*. (New York : Holt, Rinehart and Winston, 1978).

7. Dal Forno, S. & Lischner, J. Electron-phonon coupling and hot electron thermalization in titanium nitride. *Phys. Rev. Mater.* **3**, 115203 (2019).

8. Saha, B., Acharya, J., Sands, T. D. & Waghmare, U. V. Electronic structure, phonons, and thermal properties of ScN, ZrN, and HfN: A first-principles study. *J. Appl. Phys.* **107**, (2010).

9. Gupta, S. D., Gupta, S. K. & Jha, P. K. High pressure study on the phonon spectra and thermal properties in hafnium nitride and zirconium nitride. *J. Therm. Anal. Calorim.* **107**, 49–53 (2012).

10. Pierson, H. O. Interstitial Nitrides: Properties and General Characteristics. in *Handbook of refractory carbides and nitrides : properties, characteristics, processing, and applications* 181–208 (William Andrew Inc., 1996). doi:10.1016/B978-081551392-6.50007-6

11. Opeka, M. M., Talmy, I. G., Wuchina, E. J., Zaykoski, J. A. & Causey, S. J. Mechanical, Thermal, and Oxidation Properties of Refractory Hafnium and zirconium Compounds. *J. Eur. Ceram. Soc.* **19**, 2405–2414 (1999).

12. Wuchina, E. *et al.* Designing for ultrahigh-temperature applications: The

mechanical and thermal properties of HfB2, HfCx, HfNx and αHf(N). *J. Mater. Sci.* **39**, 5939–5949 (2004).

13. Li, S. *et al.* Anomalous thermal transport in metallic transition-metal nitrides originated from strong electron–phonon interactions. *Mater. Today Phys.* **15**, (2020).

14. Kittel, C. Introduction to Solid State Physics, 8th edition. J.W. *Wiley & Sons, New York,* (2004).

15. Allen, P. B. Theory of thermal relaxation of electrons in metals. *Phys. Rev. Lett.* **59**, 1460–1463 (1987).

16. Chen, X. *et al.* Pressure-induced phonon frequency shifts in transition-metal nitrides. *Phys. Rev. B* **70**, 014501 (2004).

17. Chauhan, M. & Gupta, D. C. Structural, electronic, mechanical and thermo-physical properties of TMN (TM = Ti , Zr and Hf) under high pressures : A first-principle study. *Int. J. Refract. Met. hard Mater.* **42**, 77–90 (2014).

18. Spengler, W., Kaiser, R., Christensen, A. N. & Müller-Vogt, G. Raman scattering, superconductivity, and phonon density of states of stoichiometric and nonstoichiometric TiN. *Phys. Rev. B* **17**, 1095–1101 (1978).

19. Hohlfeld, J. *et al.* Electron and lattice dynamics following optical excitation of metals. *Chem. Phys.* **251**, 237–258 (2000).

20. Diroll, B. T., Saha, S., Shalaev, V. M., Boltasseva, A. & Schaller, R. D. Broadband Ultrafast Dynamics of Refractory Metals: TiN and ZrN. *Adv. Opt. Mater.* **8**, 2000652 (2020).

21. Brorson, S. D. *et al.* Femtosecond room-temperature measurement of the electron-phonon coupling constant γ in metallic superconductors. *Phys. Rev. Lett.* **64**, 2172–2175 (1990).

22. Askes, S. H. C., Schilder, N. J., Zoethout, E., Polman, A. & Garnett, E. C. Tunable plasmonic HfN nanoparticles and arrays. *Nanoscale* **11**, 20252–20260 (2019).

23. Johnson, P. B. & Christy, R. W. Optical Constants of the Noble Metals. *Phys. Rev. B* **6**, 4370–4379 (1972).

This chapter is the final send off from the author to this work, and to any who build on it; as such, I have elected to write this in the first person – to make clear that this chapter is unlike those before, this chapter is rife with opinion. These opinions include where the research could go next, and what questions still linger on the subjects. These opinions also include some pitfalls I encountered, and how to avoid them. The future research I see in this project expand the study of excitation transfer in the gold/cerium-praseodymium oxide and the hafnium nitride, but also to include photocatalysis using these materials. The pitfalls lay in the latter option; while photocatalysis was attempted throughout my time here at The University of Twente, I ran afoul of reactor activity; it is on this that I will elaborate in this chapter. I hope this chapter may be of use and interest to some.

Devin O'Neill

Perspectives, Pitfalls and Reflections

1 Future directions

1.1 Direct continuation of gold/ceria-praseodymium oxide work

The mechanisms, and relative efficiencies of the excitation transfer can be examined in more depth through a series of additional experiments. This would include the observation of the exciton near 350 nm , wavelength dependency of excitation transfer, and determining the quantum yield for the excitation transfer. By doing this, the project would not only strengthen the mechanistic determination, but may also allow for the deconvolution of the relative contribution of each.

First and foremost, observation of the 345 nm TA signal is needed to determine if the $Ce^{4+}{}_{4f}$ band is being populated.[1] Such an observation would provide direct evidence of electrons in the conduction band due to photosensitization by the gold nanoparticles. A modification to the existing TA set-up would be needed: inclusion of an α-BBO crystal before the CaF_2 would convert the 800 nm pulse into 400 nm which would generate supercontinuum white light well into the UV.[2] Since the ceria exciton has been well studied,[3] deviation of the TA signal could be used to indicate if there is chamical interface damping (CID), or plasmon induced resonant energy transfer (PRET), or if there is charge transfer (CT) after the initial excitation. Additionally, the ratio of the 345 nm and 830 nm band may change with [Pr] which would be indicative of a changing mechanism, as only PRET forms both the hole and the electron in the CPO. Should the two bands have different quantum yields then it is an indication that PIRET alone is not responsible for the signal.[8] .

Secondly, paired with observation of the 345 nm TA signal a wavelength dependent study should be conducted. Observations of the quantum yield for wavelengths just above and below the LSPR would indicate what the varyations of the plasmoelectric potential would have on charge transfer[4]. Additionally, the use of higher energy light would allow a comparison with interband electrons,[5] which have improved energetics to overcome Schottky barrier.[6] Both of these, when combined with the above mentioned comparison ofr the 350 nm ceria exciton would allow for a deeper understanding of the relative intesnsities of the mechanisms involved. Ultimately, studies on intensity and wavelength dependence would indicate the efficiency of CT/PIRET. It has been seen in literature that for a silver/ceria system with 500 nm excitation there is considerable population

of the $Ce^{4+}{}_{4f}$ band (an injection efficiency ~15% for 400-520 nm excitation, and ~5% for 600 nm).[1] Given the relative similarity of the Fermi level for silver and gold,[7] it would be expected that the photodynamics for the Au/CeO_2 would be comparable – barring the difference in the LSPR energy. Accordingly, seeing a change in injection efficiency with [Pr] would give solid evidence for considerable CT/PIRET.

Finally, conclusive determination of the mechanism would come from the energy dependent quantum yield. If the quantum yield is invariant with excitation energy, then the process is likely to be dominated by CID (sometimes called plasmon-induced charge transfer transition)[8]. Should it follow a variant of Fowler's model, then it can be determined if it is hot-electrons overcoming a Schottky barrier or a direct metal to semiconductor transition.[8,9]

A difficulty in determining the mechanism may come from complications with the gold interband transition. It is known that interband transitions result in hot carriers with notable activity for both reactions and injections.[10] Fowler's model applied to interband or plasmon induced carriers differ only by a scaling factor,[8] so careful disambiguation of the light to exciton efficiency may be needed to determine interband effects form plasmon effects. It is possible that the samples used in chapter 4 were too thin to support effective PIRET[11], and so CID is dominating. To resolve this, a thin (few nm) dense layer of insulator around the AuNPs could be added to act as a reference where only PIRET is possible.[12]

1.2 Expanding excitation transfer to HfN

While HfN NPs was found to mainly produce heat in chapter 5, it may be possible to make a system which still favours excitation transfer. Since Chapter 4 found that by controlling the praseodymium concentration in cerium-praseodymium oxide (CPO) tuned the mechanism of excitation transfer from gold, it may be that this is also possible for HfN NPs. As such, imbedding HfN NPs in CPO may allow for use of HfN NPs as a plasmonic sensitizer of the semiconductor.

While it is likely that there will be considerable formation of heat, there may be CID, or PIRET under the right conditions. As is discussed in chapter 4, if there is signal detected at either the $Ce^{4+}{}_{4f}$ or the $Ce^{3+}{}_{4f}$ bands and signal at the $Ce^{4+}{}_{4f}$ to $Ce^{4+}{}_{5d6s}$ then there is clear evidence of CID as a means of plasmon relaxation or electron transfer. However, as neither ballistic nor

thermalized electrons have a meaningful lifetime in HfN it is less likely to be electron transfer after LSPR dephasing, and more likely to be CID – confirmation of this can be achieved through both steady state evidence, and spectral hole burning. This is a technique where a specific size distribution of the population is ableated by high intensity narrow band illumination resulting in a change in the spectra corresponding to a small size distribtuin and so allowing the calculation of the dephasing time[13,14]. Similarly, a bleach at the excitation energy, and appropriate signal at all the bands would be indicative of PIRET. It is possible, that while electrons couple very quickly to the lattice in HfN NPs, that the dephasing of the LSPR can be slower than in the CPO, or another semiconductor (as this is the requirement for PIRET)[15].

Further, this project could be expanded into systems of metal oxides/nitrides, using HfN/HfO or other plasmonic metal nitride/metal oxides. TiN/TiO_2 has been shown to be effective as a photocatalyst for dye degradation with 700 nm illumination owing to the sensitization from TiN.[16] While it has been reported that electrons from Landau damping can transfer into TiO_2, further investigation through TA may reveal other mechanisms at work; and tuning the properties of the oxide through doping, loading, or reduction may allow for control over the mechanism and amount of excitation transfer to the oxide.

1.3 Following up with activity measurements

It would be beneficial to link the observation from TA or Raman spectroscopy to catalytic activity. It is one thing to generate excited states in a material, but if the excitation can drive a reaction, or move electrons through a circuit, then the material can realize usefulness.

Given the greater promise of the gold/CPO system, I think it would be very interesting to produce photo-electrodes with gold/CPO on them for study. While it would likely be possible to build it into a photovoltaic assembly, it is likely that there would be greater benefit from changing the hierarchy so that the gold is exposed. This would allow the gold to act as an active surface, and the CPO to act as a barrier which would facilitate either hole extraction from the $Ce^{3+}{}_{4f}$ band, or electrons out of the $Ce^{4+}{}_{4f}$ band. Clearly, this dichotomy would benefit from first performing the study suggested above to determine the wavelength dependent excitation transfer efficiency to these bands. Building on this, it would be possible to move from sacrificial agents onto actual reactions. It may be that gold is ill suited

for reactions which pique interest, and then the gold can be coated with a thin layer of another metal. It has recently been shown that a thin layer of platinum on gold colloids will undergo excellent charge transfer to the surface platinum; however, it does quench the attenuation owing to the plasmon notably.[17]

In contrast to photo-electrochemistry, photo(thermal) catalysis could be performed. Of course, it is not something revelational to say, that a plasmonic nanoparticle sensitized semiconductor could be tested for photo(thermal) catalytic activity; however, once the material has been more thoroughly investigates through TA, and if it shows promise for activity through photoelectrochemical tests, then photo(themal) catalysis is a small step. Ideally, to keep a comparison fair, the environment should be comparable: so, either the TA should be done to include a liquid interface, or the catalysis should be performed using gaseous media and reactant. There are many pitfalls to working with a solid photocatalyst and gaseous reactants, but the one which I will mention in this section (rather than below) is the propagation of light. Since the reactivity of a photocatalyst is dependent on light and since powders tend to attenuate light over a short distance, it is likely that a slurry of some kind would be beneficial - that is, a suspension of particles in water. This would also give the greatest comparison to photo-electrochemical results; although it would differ from the TA performed on dry films in this thesis.

1.4 Potential follow up: design

To summarize the above section: I think it is possible to continue this line of research, and I think there is sufficient questions, and potential for a new PhD candidate to follow up.

A more in depth study of Au/CPO, to determine the wavelength dependent excitation transfer efficiency could be the first chapter. This would be most useful if it included films submerged in an aqueous environment.

A second chapter could compare the Au/CPO to HfN/CPO and HfN/HfO_2. This would also allow for the selection for the most promising material to be used in the final chapters.

A third chapter could build on this by reexamining the excitation transfer efficiency through photo-electrochemical processes. This would allow for the demonstration of utility of photogenerated excited electrons

and holes, and optimize the system for this. The use of co-catalysts could be explored, with consideration of the fourth chapter.

A fourth chapter could follow the use of the material as a photo(thermal) catalyst in the absence of applied electric fields. I would suggest the use of water suspended colloids, as this would best reflect the previous chapters' content.

2 Pitfalls and Reflections

Switching gears from the more optimistic nature of the first section, in this section I will briefly go over some issues that were encountered during my PhD work which others can benefit from. This primarily focuses on reactor activity and the need for good blanks.

2.1 Corrosive materials

At the start of my PhD, I worked with a methane/bromide system, which focused on the use of silver as a solid bromine source. The process would result in the formation of HBr, and in parts I used HBr to study portions of the process. HBr is extremely corrosive and would react with almost any set-up. This resulted in several complications due to the degradation of plastics, fluorocarbons, and metals. If the gas stream passed through tubing, then it would react; evidence of reaction was present with steel, plastics, and even with silicon plastics (likely with organic plasticizers). These reactions resulted in false positives for C_2 species, generated hydrogen, and degraded the connections (blocking Swagelok, fusing plastic parts, etc). These were relatively minor issues, but they resulted in complications which posed complications.

Avoiding these complications involved good blanks and designing experiments to look at one reaction at a time, while acknowledging that the side reactions would occur. That is to say, knowing that the HBr would react with the tubing downstream to form H_2, and that CH_3Br may react as well, then any observed CH_3Br would be biased; additionally, if any C_2 products were observed, they should be carefully examined to ensure they are not the product of plastics, seals, or CH_3Br reacting on the (corroded) steel.

2.2 Active reactors

While active tubing plagued the start of the PhD, one of the greatest frustrations came following up on the silver/ceria work: reactors with active surfaces. To determine the photothermal activity of the particles, they were removed form solution, and placed in a commercial photothermal

spectroscopic cell. Stunning activity was seen, and great excitement stirred. Changing parameters of the particles had essentially no effect, and neither did removing the particles.

The two commercial reactors used in the work were produced by Linkam (CCR-1000) and Harrick (HVC-VUV-5); in both cases, there was significant conversion of CO_2 to CO in the presence of heat and H_2. Indeed, the reactivity of the empty reactors (measured by a calibrated online MS tracing the change in [CO_2]) was a significant portion of the thermodynamic maximum (Figure 1).

Conversations with the staff of Linkam eventually revealed that both the thermocouple and the heating mantle are exposed to the gas mix. The thermocouple is composed of platinum and rhodium, while the heating mantle is composed of nickel chromium;[k] all of which are known to be catalytically active metals. It may be possible to passivate parts of the reactor (we opted to shift the project and moved the responsibility of the reactor to another). We toyed with the idea of coating with alumina, as the sample crucible and frit are alumina, through either atomic layer deposition, or oxidizing an electroplated film.

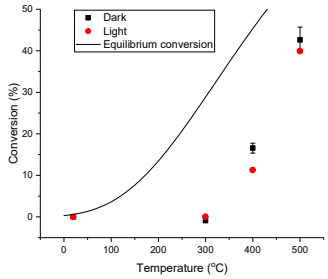

Figure 1: CO_2 conversion in the Harrick cell, flowing 25 mL/min of 1:4 CO_2:H_2 over ceria.

[k] Private correspondences with Linkam technical support engineer J. Hart, on February 24th, 2020

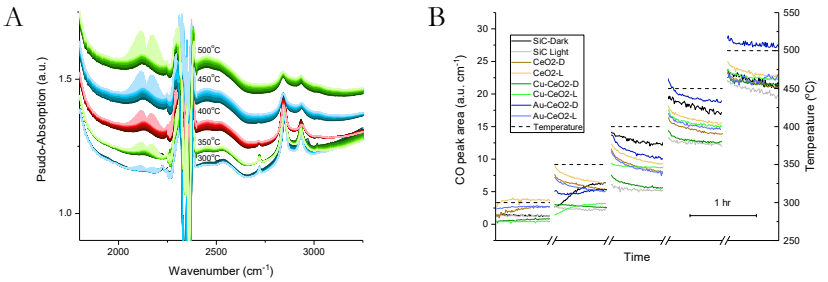

Figure 2:A) diffuse reflectance IR spectra of CO_2 reduction flowing 25 mL/min of 1:4 CO_2:H_2 over ceria. B) the CO signal intensity at each temperature, this was determined by taking the area bounded by an envelope fit around the rotovibrational CO signal.

The Harrick cell, which is meant of diffuse reflectance infrared measurements showed considerable CO formation in IR spectra as well as in the MS signals (Figure 2). The reactor was filled with ceria samples (with and without cocatalysts), and tested in the light and in the dark, additionally, SiC was used as an inert material to function as a blank. While the observed signal has implications for measuring activity, this also has significant implication for the use of the cell for any measurements of reactions: it is easy to mistake reactor activity for catalyst activity. Indeed, as the CO signal from the IR spectra was determined by envelope fitting of the rotovibrational CO spectra, it was also possible to note that there was considerable bound CO for some samples (observable in Figure 2A). It would be easy to misinterpret the observation as being a property of the material if one is not aware that the reactor is the active material.

One issue that can arise from the activity of the reactor is that a material may appear to be active, when it is actually less active in the reverse reaction. During our testing, we observed a sample which appeared to be more active at CO_2 reduction when a co-catalyst was added – the expected result. Upon further scrutiny, it was noted that the conversion for both catalyst with and without co-catalyst was below the conversion for an empty reactor. From this, we could suppose that the catalyst was active in CO oxidation, and the co-catalyst impeded this; but certainly, we could not conclude that the co-catalyst enhanced the reduction of CO_2.

This reinforced the need for blanks in experiments. In my earlier non-academic work (commercial environmental analytical lab) I learned a great deal about blanks and checks, these built on what I had learned in classes; but nothing has made it more clear to me that proper blank and check sample procedure is needed than working with these reactors. One thing I have been more aware of because of this experience, is noting in peer-reviewed papers if there are blanks or check standards; and when asked to help in the review of papers, I scrutinize these. I have been disheartened to see the very same reactors in use in papers, and no blanks having been performed.

2.3 The use of blanks and check standards

In analytical chemistry, blanks and check standards should be everywhere. There are many kinds of blanks and they reveal different things. There are a great many resources on the subject[1] but the simple point I want to foist upon a reader who is looking for information on blanks is the importance of running as many kinds of blanks as is reasonable. Running with a null sample (something inert but will still have a comparable effect on gas flow, or light distribution), without a sample (for comparison to the null sample), and with a null sample which has gone through the same steps as an actual sample (checking for any contaminants) to name a few.[18]

Similar to blanks, there are different kinds of checks that can be used, and again, each tells something different. The simplest check is to simply spike the product stream to verify the calibration on equipment, and the quality of the calibration (the check standard used should be from a different lot if not supplier than the calibration standard). Another is to spike the reagent stream, which can check for reversibility.[18] In my opinion, the former is the one which is most lacking in literature; I have seen many reports which check reversibility by introducing product. If there have been checks on the calibration, then I have not seen them reported.

3 References

(1) Pelli Cresi, J. S.; Spadaro, M. C.; D'Addato, S.; Valeri, S.; Benedetti,

[1] I have personal experience with D.C. Harris's Quantitative Chemistry, and am rather fond of it (and here is reference 18). Much of the information here has learned from that source, and also from working at a lab certified by the Canadian Association for Laboratory Accreditation

S.; Di Bona, A.; Catone, D.; Di Mario, L.; O'Keeffe, P.; Paladini, A.; et al. Highly Efficient Plasmon-Mediated Electron Injection into Cerium Oxide from Embedded Silver Nanoparticles. *Nanoscale* **2019**, *11* (21), 10282–10291.

(2) Johnson, P. J. M.; Prokhorenko, V. I.; Miller, R. J. D. Stable UV to IR Supercontinuum Generation in Calcium Fluoride with Conserved Circular Polarization States. *Opt. Express* **2009**, *17* (24), 21488.

(3) Pelli Cresi, J. S.; Di Mario, L.; Catone, D.; Martelli, F.; Paladini, A.; Turchini, S.; D'Addato, S.; Luches, P.; O'Keeffe, P. Ultrafast Formation of Small Polarons and the Optical Gap in CeO2. *J. Phys. Chem. Lett.* **2020**, *11* (14), 5686–5691.

(4) Sheldon, M.; van de Groep, J.; Brown, A.; Polman, A.; Atwater, H. Plasmoelectric potentials in metal nanostructures. *Science* **2014**, *346* (6211), 828-831.

(5) Mukherjee, S.; Libisch, F.; Large, N.; Neumann, O.; Brown, L. V.; Cheng, J.; Lassiter, J. B.; Carter, E. A.; Nordlander, P.; Halas, N. J. Hot Electrons Do the Impossible: Plasmon-Induced Dissociation of H 2 on Au. *Nano Lett.* **2013**, *13* (1), 240–247.

(6) O'Neill, D. B.; Prezgot, D.; Ianoul, A.; Otto, C.; Mul, G. Silver Nanocubes Coated in Ceria : Core / Shell Size Effects on Light-Induced Charge Transfer. *ACS Appl. Mater. Interfaces* **2020**, 12, 1, 1905–1912.

(7) Ashcroft, N. W.; Mermin, N. D. *Solid State Physics*; New York : Holt, Rinehart and Winston, 1978.

(8) Wu, K.; Chen, J.; McBride, J. R.; Lian, T. Efficient Hot-Electron Transfer by a Plasmon-Induced Interfacial Charge-Transfer Transition. *Science* **2015**, *349* (6248), 632–635.

(9) Aizpurua, J.; Baletto, F.; Baumberg, J.; Christopher, P.; Nijs, B. de; Deshpande, P.; Diaz Fernandez, Y.; Fabris, L.; Freakley, S.; Gawinkowski, S.; et al. Theory of Hot Electrons: General Discussion. *Faraday Discuss.* 2019, **214**, 245-281

(10) Zhou, L.; Zhang, C.; McClain, M. J.; Manjavacas, A.; Krauter, C. M.; Tian, S.; Berg, F.; Everitt, H. O.; Carter, E. A.; Nordlander, P.; et al. Aluminum Nanocrystals as a Plasmonic Photocatalyst for Hydrogen Dissociation. *Nano Lett.* **2016**, *16* (2), 1478–1484.

(11) Li, J.; Cushing, S. K.; Meng, F.; Senty, T. R.; Bristow, A. D.; Wu, N. Plasmon-Induced Resonance Energy Transfer for Solar Energy Conversion. *Nat. Photonics* **2015**, *9* (9), 601–607.

(12) Cushing, S. K.; Li, J.; Bright, J.; Yost, B. T.; Zheng, P.; Bristow, A. D.; Wu, N. Controlling Plasmon-Induced Resonance Energy Transfer and Hot Electron Injection Processes in Metal@TiO2 Core-Shell Nanoparticles. *J. Phys. Chem. C* **2015**, *119* (28), 16239–16244.

(13) Hendrich, C.; Bosbach, J.; Stietz, F.; Hubenthal, F.; Vartanyan, T.; Träger, F. Chemical Interface Damping of Surface Plasmon Excitation in Metal Nanoparticles: A Study by Persistent Spectral Hole Burning. *Appl. Phys. B Lasers Opt.* **2003**, *76* (8), 869–875.

(14) Vartanyan, T.; Bosbach, J.; Stietz, F.; Träger, F. Theory of Spectral Hole Burning for the Study of Ultrafast Electron Dynamics in Metal Nanoparticles. *Appl. Phys. B Lasers Opt.* **2001**, *73* (4), 391–399.

(15) Li, J.; Cushing, S. K.; Meng, F.; Senty, T. R.; Bristow, A. D.; Wu, N. Plasmon-Induced Resonance Energy Transfer for Solar Energy Conversion. *Nat. Photonics* **2015**, *9* (9), 601–607.

(16) Xu, X.; Dutta, A.; Khurgin, J.; Wei, A.; Shalaev, V. M.; Boltasseva, A. TiN@TiO 2 Core–Shell Nanoparticles as Plasmon-Enhanced Photosensitizers: The Role of Hot Electron Injection. *Laser Photon. Rev.* **2020**, *14* (5), 1900376.

(17) Engelbrekt, C.; Crampton, K. T.; Fishman, D. A.; Law, M.; Apkarian, V. A. Efficient Plasmon-Mediated Energy Funneling to the Surface of Au@Pt Core-Shell Nanocrystals. *ACS Nano* **2020**, *14* (4), 5061–5074.

(18) Harris, D. C.; Lucy, C. A. Quality Assurance and Calibration Methods. In *Quantitative Chemical Analysis, 9th edition*; W.H. Freeman & Company: New York, NY, 2016; pp 95–118.

Acknowledgments

So, I have come to this point; when I am writing my thanks to those who were along for the trip; whose help or support has enabled me to reach this point – where to begin… Well, in the words which Julie Andrews immortalized: "Lets start at the very beginning, A very good place to start".

I would like to thank my family, without whom I would not be here. Parents who taught me to question and not accept simple answers encouraged learning. Even if perhaps it was as much exasperation as intent which led my dear mother, after a simplified explanation of the Rayleigh scattering, to answer a young child's follow up question of why (the sky is blue) with the opening of the then 'font of all knowledge': the Encyclopedia Britannica. My Father with whom no broken electronic was safe from further dismantling to banish thoughts of 'magic black boxes', led me to appreciate how things worked, and to not accept the simplest handwaving answer. My dear sister, who is a close friend and confidant, and who greatly inspires me, thank you for all that you have done, for all our conversations – you're a pal and a confidant!

I would like to thank those who made this PhD possible. Guido, your abundance of cheer and exuberant joy at science made even the most dreadful moments of research palatable. Annemarie, your clear cut logical approach to so many things was a great benefit – and your organization was a much welcomed contrast to both my own, and of others. Robert Meijer, without your help, no setup or instrument would work, and so you have my thanks. To both Liddy Harryvan and Dorothy Wold-Deen, without you the group would not function anywhere near as smoothly as it does; for that I am infinitely grateful. I would also like to thank Leon Lefferts for his insightful questions during group and other presentations of mine. The companies which funded my work, I would also like to thank, BASF, SABIC, and SASOL, in partnership with the NWO made it possible to do the PhD; although the members of those companies with whom I met once or twice a year – you all made it a pleasure. Thank you, Esther, Xander, Peter, Toine, and all the others involved. I would also like to acknowledge the other PhDs in the consortium, with whom there was quite the degree of comradery and shared misery: Sabina, Rolf, and Robert, it has been a pleasure sharing my frustrations with yours. I would also like to thank all the external collaborators who made it possible to perform the research in

this thesis: Anatoli Ianoul, Daniel Prezgot, Sven Askes, Erik Garnett, and Cess Otto. I would also like to thank the wonderful members of the MESA+ analysis team, who have made many stunning micrographs with me, and I have had many lovely conversations with; thank you so much Mark and Rico, it was always such a pleasure to work with you. I would be remiss to not note my students, some of whose work contributed directly to my thesis; Ilya, Jasper K, Jasper S, Daan, and Thom, it was a pleasure to work with all of you.

I should be remiss to not thank those two who I coerced into being my paranymphs: Ronald and Piotr. You two have been wonderful friends over these years. From sharing joys or frustrations, to sharing drink and merrymaking it has been a pleasure. Ronald, I don't think it will be the same to work in an office without you; I have become too used to having a constant companion for tea and so much more. Piotr, your infection joy and mirth which like a ray of sunshine is wonderful, and much missed when clouded over.

My dear friends who have made these last four years so much more than just a PhD, but a life here in Enschede, thank you. Nakul, whose glorious luminous personality reflects a stunning light, thank you for all the wonderful memories; I am so grateful to have made such a close friend over these years. Vera, your welcoming and inviting personality made joining the group wonderful, and your efforts to make PCS a community succeeded in so many ways; I am so happy I have had the opportunity to call you friend. Kai and Kasper, you two are such wonderful people, who at times are so silly in a similar way, and made it so much fun to be around you both. Liniker it has been a pleasure working with you, you seem to always have some positivity to share. Mozghan, who has done so much for someone who is still only 25, it has been a wonderful experience knowing you (and Hamid), even if you never join for coffee. Ainoa, you are a pleasure to know, and not just for your wonderful curation of wines, but also for your kindness and joie de vivre. Bastian, while you are not my supervisor, I was nevertheless impressed by your command in meetings (something to aspire to), and your ability of command in revelry (something I will fondly remember). Yibin, your endless positivity, even in trying times is inspirational, I am very glad to have known you. Kaijian, thank you for all your help, without you it would have been much harder to complete my PhD. Sean, thank you both for everything you did in maintaining and managing the TA set-up, but also

for being a right laugh so very often. Sandy, while you were only here for a short while, it was a real treat, and I hope to stay in touch with you for a long time. I would also like to thank my partner, Tina, who has suffered listening to many rants about projects not working and greeted them with loving support.

Samenvatting

Dit proefschrift bestudeert de overdracht en omzetting van energie in plasmonische nanodeeltjes, in de context van koppeling aan halfgeleiders. Aanvankelijk is het gebruik van zilverbromide als katalysator voor de koppeling van methaan onder invloed van broom bestudeerd. Echter, dit bleek niet haalbaar te zijn binnen de beschikbare middelen. De focus op plasmonische nanostructuren begint bij het gebruik van een silver @ ceria (core @ shell) nanocube en Raman-spectroscopie om de mate van ladingsoverdracht op het grensvlak bij verschillende excitatiegolflengten te onderzoeken (in samenwerking met D. Prezgot en A. Ianoul). Dit is gebaseerd op het gebruik van een laagje gouddeeltjes ingebed onder CexPryOz (CPO), wat werd gebruikt om de invloed die de spectrale overlap heeft op het absolute aantal foto-opgewekte dragers die aanwezig zijn in de CPO te bestuderen - een onderzoek naar het relatieve voordeel van energie- en ladingsoverdracht.

Het verdere werk maakt gebruik van HfN, een materiaal naar verwachting langlevende ladingsdragers zou bevatten na het defaseren van de plasmons. Dit werd onderzocht met ultrasnelle spectroscopie met als doel hete dragers te onttrekken; echter, in plaats van hete elektronen werd volledige thermische relaxatie waargenomen. Deze conclusie wordt bevestigd door simulaties, in samenwerking met S. Askes, E. Garnet. Het werk aan HfN overbrugt de verschillen tussen theorie en experimenten die beschreven worden in eerdere literatuur. Het proefschrift sluit af met een hoofdstuk over toekomstig werk dat voort kan komen uit dit onderzoek; en over verschillende problemen waar tijdens het onderzoek tegenaan werd gelopen - namelijk de hoge intrinsieke activiteit van commerciële spectroscopische thermische reactoren.

Hoofdstuk 2 behandelt het gebruik van zilverbromide als een door licht opgewekte halogeenbron voor de activering van methaan. Een dergelijk proces zou de productie van hogere orde koolwaterstoffen uit methaan mogelijk maken, met als bijproduct waterstof. Tegelijkertijd kan de reactor kan worden beveiligd door het uitschakelen van de lichtbron. De fotolyse van zilverbromide werd gebruikt om broomradicalen te produceren die met methaan kunnen reageren om waterstofbromide en methylbromide te produceren. Het doel was om het methylbromide vervolgens over een vast zuur te koppelen, om koolwaterstof soorten van hogere orde te produceren, terwijl het waterstofbromide een reactie aangaat met zilver om zilverbromide te regenereren en waterstof vrij te maken. Helaas toonden de

onderzoeken aan dat het proces niet haalbaar was bij 1 bar, aangezien de benodigde verhouding tussen verlicht oppervlak en volume 58 m2 / L was. Het was bevestigd dat waterstofbromide reageert met zilver om waterstof vrij te maken; echter, er werd ook een sterk zure vloeistof afgezet in de reactor. Hoewel het mogelijk zou kunnen zijn een rendabel katalytisch proces te creëren, werd uiteindelijk de poging daartoe niet voortgezet.

Hoofdstuk 3 onderzoekt plasmonische sensibilisatie van halfgeleiders om de door licht geïnduceerde fotokatalytische efficientie in een core @ shell geometrie te verbeteren. Het voorkomen en het mechanisme van synergetische effecten bij fotokatalyse van zulke geometrieën staan onder debat en worden vermoedelijk ofwel door licht-geïnduceerde ladingsoverdracht (CT), ofwel door thermische effecten veroorzaakt. Deze studie richt zich op de relatie tussen de afmetingen van Ag @ CeO2 nanocubes, de golflengte-afhankelijke efficiëntie en het mechanisme van door licht geïnduceerde directe ladingsoverdracht. Een 4-mercaptobenzoëzuur (4-MBA) verbinding tussen kern en schaal fungeert als een Raman-probe voor CT. Voor alle Ag @ CeO2 nanocubes neemt CT toe met afnemende excitatiegolflengte, met een opmerkelijke toename bij en onder 514 nm. Dit is volledig te verklaren door CT van zilver naar de 4-MBA LUMO, met de toename van excitatiegolflengten die de Ag / 4-MBA LUMO bandgap van 2,28 eV (543 nm) overschrijden. Een tweede waargenomen trend is een toename van de CT opbrengst met de dikte van de ceriumoxide schaal, die wordt toegewezen aan relaxatie van het geëxciteerde elektron verder in de ceriumoxide geleidingsband, waardoor mogelijk defecten gegenereerd worden.

Hoofdstuk 4 onderzoekt de energie- en ladingsoverdracht tussen een gouden plasmonisch nanodeeltje en een dunne film van cerium-praseodymiumoxide. We laten met fs transiënte absorptie spectroscopie zien, dat met goud gesensibiliseerd cerium-praseodymiumoxide een ladings- of energieoverdracht ondergaat via verschillende mechanismen, afhankelijk van het praseodymiumgehalte. Voor monsters zonder praseodymium lijkt het dominante mechanisme BCT te zijn, en er is opmerkelijke warmteontwikkeling op langere tijden. Voor samples met praseodymium varieert het mechanisme: lage belasting (3% Pr n / n en 5% Pr n / n) wordt waarschijnlijk gedomineerd door CID, terwijl 10% Pr n / n significante PIRET vertoont. Steady-state spectroscopie toont aan dat LSPR-demping toeneemt met praseodymiumbelasting. Deze studie stelt vast dat de

sensibilisatie van ceriumoxide voor PIRET door Pr-doping bovendien CID kan bevorderen, wat gunstig kan zijn in fotokatalytische en fotovoltaïsche toepassingen; dit kan gevolgen hebben voor andere halfgeleiders.

Hoofdstuk 5 bouwt verder op de grote interesse in de ontwikkeling van alternatieven voor edelmetalen in plasmonische nanostructuren. Overgangsmetaal nitriden zijn veelbelovend vanwege hun robuuste vuurvaste eigenschappen. De fotofysica van deze nanostructuren, met name de hete-carrier-dynamica en fotothermische respons op ultrasnelle tijdschalen worden nog niet goed begrepen, wat hun implementatie in toepassingen zoals fotothermische katalyse of zonne-thermofotovoltaïsche systemen beperkt. In deze studie worden de lichtgeïnduceerde relaxatieprocessen in in water verspreide HfN-nanodeeltjes verklaard door fs transiënte absorptie, Lumerical FDTD en COMSOL Multiphysics simulaties en temperatuurafhankelijke ellipsometrie. We laten ondubbelzinnig zien dat HfN-nanodeeltjes geabsorbeerde fotonen binnen <100 fs omzetten in warmte; er wordt geen teken van hete-ladings-dragers waargenomen. Interessant genoeg wordt bij hoge fotonenergie of intense bestraling gestimuleerde Raman-verstrooiing waargenomen, wat kenmerkend is voor oxynitride-oppervlakteterminatie. Deze bevindingen suggereren dat overgangsmetaalnitriden voordelen zouden kunnen bieden ten opzichte van edelmetalen op het gebied van plasmonische fotothermische katalyse.

Hoofdstuk 6 gaat in op de vooruitzichten en valkuilen van het werk dat in dit proefschrift wordt uitgevoerd. Eerst wordt een beeld geschetst van het toekomstige werk dat gedaan zou kunnen worden, en uiteindelijk wordt een vervolg PhD voorgesteld die zou voortbouwen op het werk van de hoofdstukken 4 en 5, en het werk zou uitbreiden om de bruikbaarheid van het systeem aan te tonen. De tweede helft van het hoofdstuk schetst enkele van de problemen waar tegenaan werd gelopen bij het gebruik van commerciële fotothermische reactoren. De reactoren hebben blootgestelde componenten die katalytisch actief zijn. Het hoofdstuk wordt afgesloten met een korte discussie over blanco's en controlestandaarden, die moeten worden gebruikt als er in de toekomst een poging wordt gedaan om de reactoren te gebruiken.